

**A Thesis Submitted for the Degree of PhD at the University of Warwick**

**Permanent WRAP URL:**

<http://wrap.warwick.ac.uk/164551>

**Copyright and reuse:**

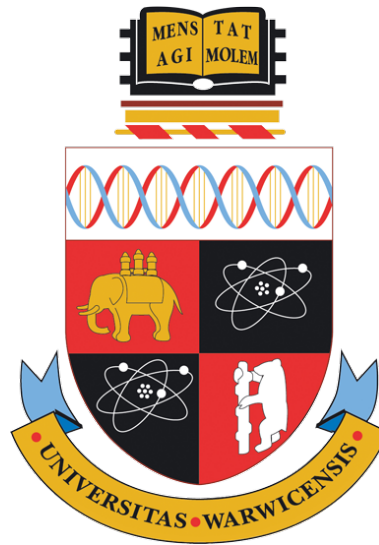
This thesis is made available online and is protected by original copyright.

Please scroll down to view the document itself.

Please refer to the repository record for this item for information to help you to cite it.

Our policy information is available from the repository home page.

For more information, please contact the WRAP Team at: [wrap@warwick.ac.uk](mailto:wrap@warwick.ac.uk)



# Zonal Flows, Geodesic Acoustic Modes and Drift-Waves in magnetically confined plasmas

by

**Sanket Gadgil**

**Thesis**

Submitted to the University of Warwick

for the degree of

**Doctor of Philosophy**

**Department of Physics**

September 2020

# Contents

<b>List of Tables</b>	<b>iii</b>
<b>List of Figures</b>	<b>iv</b>
<b>Acknowledgments</b>	<b>x</b>
<b>Declarations</b>	<b>xi</b>
<b>Abstract</b>	<b>xii</b>
<b>Chapter 1 Introduction</b>	<b>1</b>
1.1 Present Power Generation . . . . .	2
1.2 Nuclear Power . . . . .	2
1.3 Plasma Physics - Basic Parameters . . . . .	6
1.4 Plasma Physics - Drifts and invariants . . . . .	8
1.5 Plasma Physics - Kinetic description . . . . .	9
1.6 Plasma Physics - Fluid Descriptions . . . . .	10
1.7 Fusion Power . . . . .	14
1.8 Magnetic Confinement Fusion (MCF) . . . . .	16
1.9 Spherical Tokamak . . . . .	19
1.10 Transport . . . . .	20
1.11 Thesis outline . . . . .	26
<b>Chapter 2 Drift-Wave instability in the presence of Zonal Flows</b>	<b>27</b>
2.1 Introduction . . . . .	27
2.2 Methodology . . . . .	30
2.2.1 Model Equations . . . . .	30
2.2.2 Global Dispersion Relation . . . . .	32

2.2.3	Numerical Analysis . . . . .	36
2.3	Discussion . . . . .	39
2.3.1	Further analysis at $V_0 = 1.0$ . . . . .	44
2.4	Conclusion . . . . .	45
<b>Chapter 3</b>	<b>Linear GAM Properties</b>	<b>47</b>
3.1	Introduction . . . . .	47
3.2	Geodesic Acoustic Mode . . . . .	47
3.3	CENTORI . . . . .	51
3.4	CENTORI results . . . . .	54
3.4.1	Continuous wavelet transform (CWT) . . . . .	55
3.4.2	Fluctuating Electron Density ( $n_{e1}$ ) . . . . .	57
3.4.3	Total Scalar Potential ( $\phi$ ) . . . . .	62
3.4.4	Fluctuating Scalar Potential ( $\phi_1$ ) . . . . .	65
3.4.5	Outboard Mid-Plane Fluctuating Electron Density ( $n_{e1}$ ) . . . . .	68
3.4.6	Outboard Mid-Plane Scalar Potential ( $\phi$ ) . . . . .	70
3.5	Summary . . . . .	70
<b>Chapter 4</b>	<b>Non-Linear GAM Properties</b>	<b>72</b>
4.1	Introduction . . . . .	72
4.2	Methodology . . . . .	73
4.3	Results . . . . .	74
4.3.1	Outboard Mid-Plane Fluctuating Electron Density ( $n_{e1}$ ) . . . . .	75
4.3.2	Fluctuating Electron Density ( $n_{e1}$ ), $\theta = 90^\circ$ . . . . .	79
4.3.3	Outboard Mid-Plane Total Scalar Potential ( $\phi$ ) . . . . .	81
4.4	Summary . . . . .	82
<b>Chapter 5</b>	<b>Conclusion</b>	<b>83</b>
<b>Appendix A</b>	<b>GAM derivation</b>	<b>85</b>



# List of Tables

1.1	Comparison of specifications of MAST and JET.[1][2]	20
-----	---	----

# List of Figures

1.1	A few examples of cross-section profiles for different species pairings considered for fusion.[3]	15
1.2	A schematic of a tokamak.[4]	17
1.3	Labelling of a typical tokamak geometry.[5]	18
2.1	Example of integration contour used in the averaging technique, labels for the terms in Eq. (2.18) are also included.	34
2.2	2.2a The growth rate(imaginary component of $\omega$ ) versus the perturbation mode number. The parameters are: $\alpha = 0.5$ , $\kappa = 1.0$ and $k_{ZF} = 0.4\pi$ and $V_0 = 0.1$ . 2.2b A scan across $\alpha - \kappa$ space with the z-axis showing the maximum growth rate. The red dot shows the $\alpha = 0.5$ and $\kappa = 1.0$ location.	37
2.3	Plots showing the time-evolution of scalar potential. The time-steps are in units of $\omega_{ci}^{-1}$ . The initial perturbation's $k_y$ is set to $0.3\pi$ , or a mode number $m_s = 6$ .	38
2.4	An energy plot of the simulation run shown in Fig. 2.3. The A-D labelled points show the energies at various stages and the transition from zonal flow to drift-wave dominance is clear. The energies are normalised to the same constant, which is chosen for convenience.	39
2.5	Figures showing the frequencies and growth rates of the drift-waves against their mode number, $m_s$ at different values of $V_0$ with identical conditions to Fig. 2.4. The curves correspond to predictions from the linear stability theory, the solution to Eq. (2.27) and the measure values from the simulation. The y-axis units are $\omega^* = \omega/k_y V_0$ , these apply to the linear result as well to allow comparison between results.	40

2.6	The main plot shows the energy of the system with constants set to $\alpha = 0.5$ , $\kappa = 1.0$ , $V_0 = 1.0$ , $k_{ZF} = 0.4\pi$ and with a drift-wave perturbation mode number $m_s = 2$ . Panel A shows the initial transition and inversion of dominant states, Panel B shows full dominance of the drift-wave mode and suppression of the zonal flow, with Panel C showing the return to zonal flow dominance. . . . .	41
2.7	An energy plot showing the results from a simulation run similar to Fig. 2.6, but with $V_0 = 0.01$ to illustrate a lack of zonal flow suppression as a result of energy exchange. . . . .	42
2.8	A similar figure to Fig. 2.6 but with $\alpha = 0.2$ . This shows faster dynamics in all respects including drift-wave growth and subsequent zonal flow dominance later in the simulation. . . . .	43
2.9	Figure showing the zonal flow decay rates with $\alpha = 0.5$ consistent with all simulation data from Figures 2.6 and earlier. . . . .	44
2.10	Figures showing the frequencies and growth rates of the drift-waves against their mode number, $m_s$ . . . . .	45
3.1	Knorr's model [6] . . . . .	50
3.2	A breakdown of the coordinate systems used by CENTORI[7] . . . . .	52
3.3	(a) Plot of the structure of the 'bump' wavelet from the MATLAB documentation.[8] (b) The frequency-time domain structure of the 'bump' wavelet. [8] . . . . .	56
3.4	(a): CWT of the fluctuating electron density, $n_{e1}$ , showing frequency as a function of normalised $\psi$ averaged over 3.75-5ms of the run at a fixed poloidal position of $\theta = 90^\circ$ . The red line signifies the expected profile of the GAM frequency if it were present across the entire radial extent. (b): CWT showing frequency as a function of time in a fixed radial location, $\psi = 0.92$ , and a fixed poloidal location, $\theta = 90^\circ$ , between 17kHz and 47kHz. The red line represents the expected profile of the GAM frequency at this particular location across the time-span calculated based on Eq. (3.31). . . . .	57
3.5	(a): Filtered time trace showing the fluctuating electron density, $n_{e1}$ , for frequencies between 17kHz - 47kHz at radial location of 0.92 and a poloidal angle of $90^\circ$ . (b): Power spectrum of the fluctuating electron density, $n_{e1}$ , across the 3.75-5ms time-span in a fixed radial position, 0.92, and poloidal angle, $90^\circ$ . . . . .	59

3.6	(a): Fourier transform of fluctuating electron density, $n_{e1}$ , showing frequency vs. poloidal mode number at a fixed radial location, 0.92. (b): Fourier transform of fluctuating electron density, $n_{e1}$ , showing frequency vs. radial mode number at a fixed poloidal angle, $90^\circ$ . . . . .	60
3.7	(a): Time-space plot of fluctuating electron density, $n_{e1}$ , vs. poloidal angle. The poloidal angles are such that $0^\circ$ is the out-board mid-plane and $90^\circ$ is the point in the tokamak with the highest Z-axis value per Figure 3.2. The radial location is 0.92 (b): Time-space plot of fluctuating electron density, $n_{e1}$ , vs. normalised $\psi$ at a poloidal angle $90^\circ$ . . . . .	61
3.8	CWT of total scalar potential, $\phi$ , data showing frequency versus time in a fixed radial location, 0.92, and a fixed poloidal location, $90^\circ$ , between 17kHz and 47kHz. The red line represents the expected profile of the GAM frequency at this particular location across the time-span. . . . .	62
3.9	(a): Filtered time trace showing the total scalar potential, $\phi$ , for frequencies between 17kHz - 47kHz at radial location of 0.92 and a poloidal angle of $90^\circ$ . (b): Power spectrum of the total scalar potential, $\phi$ , across the 3.75-5ms time-span in a fixed radial position, 0.92, and poloidal angle, $90^\circ$ . . . . .	63
3.10	(a): Fourier transform of total scalar potential, $\phi$ , showing frequency vs. poloidal mode number at a fixed radial location, 0.92. (b): Fourier transform of total scalar potential, $\phi$ , showing frequency vs. radial mode number at a fixed poloidal angle, $90^\circ$ . . . . .	64
3.11	(a): Time-space plot of total scalar potential, $e\phi/\langle T_e \rangle$ , vs. poloidal angle. The poloidal angles are such that $0^\circ$ is the out-board mid-plane and $90^\circ$ is the point in the tokamak with the highest Z-axis value per Figure 3.2. The radial location is 0.92. (b): Time-space plot of total scalar potential, $e\phi/\langle T_e \rangle$ , vs. normalised $\psi$ at a poloidal angle $90^\circ$ . . . . .	64
3.12	CWT showing frequency versus time in a fixed radial location, 0.92. and a fixed poloidal location, $90^\circ$ , between 17kHz and 47kHz. The red line represents the expected profile of the GAM frequency at this particular location across the time-span. . . . .	65
3.13	(a): Filtered time trace showing the fluctuating scalar potential, $\phi_1$ , for frequencies between 17kHz - 47kHz at a radial location, 0.92 and a poloidal angle of $90^\circ$ . (b): Power spectrum of fluctuating scalar potential, $\phi_1$ , across the 3.75-5ms time-span in a fixed radial position, 0.92, and poloidal angle, $90^\circ$ . . . . .	66

3.14	(a): Fourier transform of fluctuating scalar potential, $\phi_1$ , showing frequency vs. poloidal mode number at a fixed radial location, 0.92. (b): Fourier transform of fluctuating scalar potential, $\phi_1$ , showing frequency vs. radial mode number at a fixed poloidal angle, $90^\circ$ . . . . .	66
3.15	(a): Time-space plot of fluctuating scalar potential, $\phi_1$ , vs. poloidal angle. The poloidal angles are such that $0^\circ$ is the out-board mid-plane and $90^\circ$ is the point in the tokamak with the highest Z-axis value per Figure 3.2. The radial location is 0.92. (b): Time-space plot of fluctuating scalar potential, $\phi_1$ , vs. normalised $\psi$ at a poloidal angle $90^\circ$ . . . . .	67
3.16	(a): CWT of the fluctuating electron density, $n_{e1}$ , showing normalised $\psi$ versus frequency averaged over 3.75-5ms of the run at a fixed poloidal position of $\theta = 0^\circ$ . The red line signifies the expected profile of the GAM frequency if it were present across the entire radial extent. (b): CWT showing frequency versus time in a fixed radial location, 0.92, and a fixed poloidal location, $0^\circ$ , between 17kHz and 47kHz. The red line represents the expected profile of the GAM frequency at this particular location across the time-span. . . . .	68
3.17	(a): Filtered time trace showing the fluctuating electron density, $n_{e1}$ , for frequencies between 17kHz - 47kHz at radial location of 0.92 and a poloidal angle of $0^\circ$ . (b): Power spectrum of the fluctuating electron density, $n_{e1}$ , across the 3.75-5ms time-span in a fixed radial position, 0.92, and poloidal angle, $0^\circ$ . . . . .	69
3.18	(a): Fourier transform of fluctuating electron density, $n_{e1}$ , showing frequency vs. radial mode number at a fixed poloidal angle, $0^\circ$ . (b): Time-space plot of fluctuating electron density, $n_{e1}$ , vs. normalised $\psi$ at a poloidal angle $0^\circ$ . . . . .	69
3.19	(a): Filtered time trace showing the fluctuating scalar potential, $\phi_1$ , for frequencies between 17kHz - 47kHz at radial location of 0.92 and a poloidal angle of $0^\circ$ . (b): Time-space plot of fluctuating scalar potential, $\phi_1$ , vs. normalised $\psi$ at a poloidal angle $0^\circ$ . . . . .	70

4.1	(a) Power spectrum of the fluctuating electron density, $n_{e1}$ . The power spectrum is averaged over the time-span of 3.75-5ms at a radial location of 0.92 and poloidal angle of $0^\circ$ . The red circles are aligned with the two main frequencies of interest, 23kHz and 30kHz. The cyan circles are aligned with the interaction frequencies of 46kHz, 53kHz and 60kHz. (b) Shows an unfiltered time trace of the fluctuating electron density, $n_{e1}$ , at a radial location of 0.92 and a poloidal angle of $0^\circ$ . . . . .	75
4.2	Bicoherence of the fluctuating electron density, $n_{e1}$ , at a radial location of 0.92 and poloidal angle of $0^\circ$ . There is a time shift of $0.047ms \sim T_{GAM}$ , where $T_{GAM}$ is the approximate time period of the 23kHz mode. This plot is unfiltered therefore the bicoherence values range from 0-1. . . . .	76
4.3	Bicoherence of the fluctuating electron density, $n_{e1}$ , at a radial location of 0.92 and poloidal angle of $0^\circ$ . There is a time shift of $0.047ms \sim T_{GAM}$ , where $T_{GAM}$ is the approximate time period of the 23kHz mode. This plot is filtered to exclude values below 0.5. . . . .	77
4.4	Bicoherence of the fluctuating electron density, $n_{e1}$ , at a radial location of 0.92 and poloidal angle of $0^\circ$ . There is a time shift of $0.047ms \sim T_{GAM}$ , where $T_{GAM}$ is the approximate time period of the 23kHz mode. This plot is filtered to exclude values below 0.75. . . . .	78
4.5	Power spectrum of the fluctuating electron density, $n_{e1}$ . The power spectrum is averaged over the time-span of 3.75-5ms at a radial location of 0.92 and poloidal angle of $90^\circ$ . The red circles are aligned with the two main frequencies of interest, 23kHz and 30kHz. The cyan circles are aligned with the interaction frequencies of 46kHz, 53kHz and 60kHz. . . .	78
4.6	Bicoherence of the fluctuating electron density, $n_{e1}$ , at a radial location of 0.92 and poloidal angle of $90^\circ$ . There is a time shift of $0.047ms \sim T_{GAM}$ , where $T_{GAM}$ is the approximate time period of the 23kHz mode. This plot is unfiltered therefore the bicoherence values range from 0-1. . . . .	80
4.7	Bicoherence of the fluctuating electron density, $n_{e1}$ , at a radial location of 0.92 and poloidal angle of $90^\circ$ . There is a time shift of $0.047ms \sim T_{GAM}$ , where $T_{GAM}$ is the approximate time period of the 23kHz mode. This plot is filtered to exclude values below 0.75. . . . .	80
4.8	Power spectrum of the total scalar potential, $\phi$ . The power spectrum is averaged over the time-span of 3.75-5ms at a radial location of 0.92 and poloidal angle of $0^\circ$ . . . . .	81

4.9	Bicoherence of the total scalar potential, $\phi$ , at a radial location of 0.92 and poloidal angle of $0^\circ$ . There is a time shift of $0.047ms \sim T_{GAM}$ , where $T_{GAM}$ is the approximate time period of the 23kHz mode. This plot is filtered to exclude values below 0.75. . . . .	82
A.1	Knorr's model[6] . . . . .	90

# Acknowledgments

I would like to thank my supervisor, Dr. Bogdan Hnat, for his continued support, advice, availability and patience.

I would also like to thank: Professor George Rowlands and Assistant Professor Makoto Sasaki, for informative discussions and for collaborating on the work presented in this thesis.

I am also thankful to my office-mates: Jack, Lauren, Alun, Selina-Jane, Duncan, Liz and Bernard. All of you made it a joy to work in the office.

Finally, I would like to thank the EPSRC (Engineering and Physical Sciences Research Council) whose funding made this PhD possible.



# Declarations

I declare that work presented in this thesis is my own original work except where indicated otherwise and has not been submitted in any capacity for a degree at another academic institution. Work for this thesis was undertaken under the supervision of Dr. Bogdan Hnat. Parts of this thesis have been previously published by the author:

## **Chapter 2:**

- [9] S. Gadgil, B. Hnat, and G. Rowlands. Investigation of drift-wave instability in the presence of zonal flows using spatial averaging. *Physics of Plasmas*, 26(1):012105, 2019. doi: 10.1063/1.5049087

Research was published during the development of this thesis, but does not form part of the thesis:

- [10] B Hnat, S Gadgil, A Kirk, F Militello, and N Walkden. Experimental constraint on the radial mode number of the geodesic acoustic mode from multi-point langmuir probe measurements in mast ohmic plasma. *Plasma Physics and Controlled Fusion*, 60(8):085016, 2018. doi: 10.1088/1361-6587/aacd58

Additionally work in Chapter 3 and Chapter 4 was completed in collaboration with Assistant Professor Makoto Sasaki.

# Abstract

A key component in understanding the L-H transition is the behaviour and interactions of Zonal Flows(ZF), Geodesic Acoustic Modes(GAM) and Drift-Waves. To that end, this thesis explores the behaviour of GAMs and the interactions between ZF and drift-waves. For investigating the ZFs and drift-wave interaction, a new spatial averaging technique is developed and applied to the linearization of the modified Hasegawa-Wakatani model. A global dispersion relation for drift-waves in the presence of zonal flows is obtained [9]. Subsequently both the linear and non-linear behaviour of GAMs is investigated by analysing data from a fluid simulation of the MAST(Mega Ampere Spherical Tokamak) tokamak. Evidence of linear physics is obtained by investigating the spatial and temporal modal structures of GAMs using continuous wavelet transforms and fast fourier transforms. Non-linear physics is investigated using bicoherence analysis and it is shown that non-linear coupling exists between GAM and low frequency modes. Additionally self-interaction of GAMs is also observed and a poloidal dependence of this behaviour was recovered.

# Chapter 1

## Introduction

One of the more prominent debates in the public consciousness in the 21st century concerns anthropogenic climate change. The need to cut greenhouse gas emissions is now evident, however, the path to achieving this goal has introduced a debate with a larger scope. How do humans produce the energy needed for civilization in the future? How much energy do we need to produce and particularly in what form will that energy be needed? A potential answer to these questions is to use renewable energy sources. There are many disparate solutions, wind power is particularly relevant in the U.K. where offshore wind farms are now becoming a significant source of electricity and a means to reduce greenhouse gas emissions[11]. The economies of scale have started to reduce the cost of wind farms, however, without reliable electricity storage technology they still rely on gas turbines to make up for any energy shortfall. A similar lack of consistent output hampers uptake of solar power. The other two possible renewable sources available to the U.K., tidal and wave power, are mired in environmental concerns that are separate to emissions, such as marine life conservation. At the moment without significant electricity storage advances in both technology and economics, pure renewables seem a difficult proposition. Regardless, due to momentum both from the public and governments around the world, renewables seem likely to be a large part of the energy mix in the future. However to maintain (and possibly expand) current global energy usage, a solution that provides a steady baseload of power would be highly desirable. To that end, nuclear power is a low-emissions option.

## 1.1 Present Power Generation

The main method of electricity production in the 20th century was based around burning fossil fuels to release stored chemical energy and convert said energy to electricity via generating steam and turning a turbine. The final conversion of this chemical energy to electricity is fairly inefficient, the higher heating value efficiency of coal fired power plants is  $\sim 40\%$ , and the stored chemical energy per volume is quite low in and of itself. There are a few reasons why it has succeeded as a primary means of energy production. One is that the fuel itself is relatively abundant(at least for now) and easy to transport, handle and ultimately use. With this and the sheer advantage afforded by nearly a century(perhaps 2) of research and development focused around this method meant that it could not only be used for electricity generation but also, among many other things, for transportation and heating. However, in the absence of any other sources of abundant chemical energy that would also have low-emissions, it's clear a new way to generate energy must be found. One possibility is to exploit the energy available in the environment, either from wind, solar, hydro-electric, tidal, geothermal, etc. In truth however wind, solar and hydro are effectively all solar powered either directly or indirectly. Tidal is dependent on the gravitational interplay between the Earth, Moon and Sun and is relatively stable and predictable. Geothermal partially sources its energy from the gravitational compression inherent in the structure of the Earth and from the decay of various nuclei trapped in the interior of the planet. All of these are sustainable in the long term and cause far less of an environmental impact than burning fossil fuels. However, their ties to the environment are the source of their disadvantages as well, chiefly that they are not very flexible, convenient or universal. By comparison the energy-density of fossil fuels means that far less land is taken up by their use and the universality is lent by the fact that, so long as one has a solid(relatively dry) platform and oxygen then one can deploy the technology almost anywhere. The major disadvantages of fossil-fuels being the lack of sustainability and emissions of greenhouse gases and other pollutants.

## 1.2 Nuclear Power

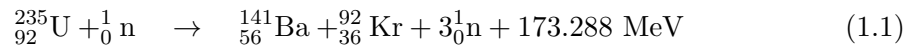
Fundamentally nuclear power is somewhat similar to chemical power in the sense that they are both used by releasing stored energy in a given volume of material(fuel). The key differences lie in how the energy is stored and how it is liberated. In chemical power the energy is stored as binding energy of the bonds between atoms in a molecule. To liberate this energy a chemical reaction between two molecules that is exothermic is needed,

producing more energy than is needed to instigate it, in other words, with products that have a higher binding energy than the reactants,

$$\text{Energy gained} = \text{binding energy of products} - \text{binding energy of reactants}.$$

The method of energy liberation in nuclear power is only slightly different from a purely qualitative description. Nuclear power also requires an exothermic reaction but depending on the type of nuclear power one may not need two reactants and nuclear transmutation itself may be an exothermic process. Given the difference in strength between the electromagnetic force and strong nuclear force, it is unsurprising that the binding energy in the bonds between nuclei is almost  $10^3$  higher than a given chemical bond in a molecule. Therefore per unit mass, nuclear fuel has much more stored energy.

In nuclear fusion two or more reactants can combine(“fuse”) to create products which have more binding energy than before. The spare energy, equal to the subsequent mass deficit, is usually contained in the kinetic energy of the products or directly in photons that may be produced. In nuclear fission the reactant can split and creates products that have more binding energy than before. A common isotope of Uranium,  $^{235}\text{U}$ , is used as fuel in nuclear reactors. Natural uranium needs to be enriched to increase the concentration of  $^{235}\text{U}$  present. The level of this enrichment is tailored to suit the need. For light water reactors this enrichment is rarely more than 3-5%[12]. The enrichment is necessary because  $^{235}\text{U}$  is a fissile isotope of Uranium. An isotope of an element is fissionable if it can undergo nuclear fission(either spontaneously or with external action). Additionally an isotope of an element is fissile if it is fissionable and can sustain a chain reaction. A chain reaction is defined as an externally induced nuclear fission reaction which produces neutrons in sufficient quantity and energy as part of the products to initiate more than 1 nuclear fission reaction in another nucleus in the fissile material. This chain reaction is at the heart of applications utilizing nuclear fission. An example of a reaction that occurs inside a fission reactor is:



The extra 173.288 MeV corresponds to the excess energy released in the reaction, this presents as the kinetic energy of the reaction products. The non-neutronic products can undergo further fission reactions via spontaneous decay and produce yet more energy in the form of excess kinetic energy of the decay products. The increase in kinetic energy is equivalent to an increase in heat in the system and this heat can be extracted for electricity generation. In order to ensure fission reactions continue the free neutrons must be slowed down by a moderator, examples include graphite and ordinary water. Having

slower neutrons increases the cross-section of the fission reaction and allows the chain reaction to continue in the presence of low-enriched uranium. The number of slowed neutrons in the system now exceed the initial number before the reaction. As a result of this if the arrangement of the  $^{235}\text{U}$  atoms is optimal then the slowed(thermal) neutrons can proceed to induce multiple fission reactions. In reality the average number of free neutrons produced in a  $^{235}\text{U}$  fission reaction is 2.4[13]. Managing the resulting chain reaction via control of available free neutrons is crucial, either via neutron absorbing materials, which make up components known as control rods or simply managing the geometry of the system to allow them to escape without reacting. The heat that is generated can be directly extracted from the system via a coolant and used to generate steam which then drives turbines and produces electricity.

Nuclear fusion by contrast would not be reliant on management of a runaway process in order to generate power. In fusion there are different challenges, chief among which is overcoming the Coulomb barrier, and the only way to do this is to increase the speed at which the particles collide. While fission generally deals in solid fuel, the speeds at which particles move in solids are too slow to initiate fusion. A way to increase the average speed of the particles in a material is to increase the temperature. There are several temperature thresholds which signify transition points going from: solid→liquid→gas→plasma. Plasma is the single most common form of matter in the universe since it makes up almost all of the visible matter in the universe. In a gas, atoms or molecules are free to move in 3D space and are mostly neutral so collisions between them are more or less inconsequential, mostly serving to bring the gas to an equilibrium temperature. However when sufficient heat is added the atoms in a gas can disassociate into ions and electrons. Two ions in the plasma will be positively charged and will repel but if brought close enough to each other can fuse into another element. To overcome the Coulomb barrier it is not enough to simply heat fuel material to a plasma but heat it sufficiently to allow some fraction of the ions to fuse. As it turns out the temperatures needed to achieve this reaction are so high that no material can withstand prolonged exposure to the heated plasma, therefore a method is needed to prevent the plasma from touching the walls of the reactor. Luckily the individual components of a plasma are charged and therefore sensitive to electromagnetic fields. And so in a reactor, shaped magnetic fields are necessary to contain the plasma. The last piece of the puzzle is to heat the plasma further such that the fraction of ions that are fusing can produce enough heat to allow the plasma to maintain its own temperature. If this were achieved one could ideally run the reactor indefinitely so long as more fuel was provided and the waste products(helium nuclei known as alpha particles) were removed. Unfortunately

the reactor cannot run at a 100% efficiency and once all losses have been taken into account, the energy-gain necessary,  $Q = \frac{\text{ENERGY PRODUCED}}{\text{ENERGY CONSUMED}}$  turns out to be  $> 5$ , beyond this energy gain the plasma is said to have ignited and the fusion reactions are self-sustaining. It is also crucial to note that the thermal energy produced that keeps the plasma hot is only a portion of the total produced energy. The rest of the energy, mostly in the form of neutrons which do not interact with the magnetic field, is captured externally and would eventually be used to heat water and drive turbines to produce electricity. This not only goes to the national grid but also powers the systems that the reactor is dependent on. These features allow fusion to retain all of the advantages of nuclear fission whilst eliminating certain disadvantages. These include the lack of long-lived radioactive waste, the walls of a fusion reactor are likely to be bombarded by neutrons and made radioactive via transmutation(a process referred to as “activation”), however the material has a short half-life,  $\sim 10$  years rather than 10000s years for waste from fission reactions. Another is the fact that since fusion constantly requires external input, either in the form of heat, fuelling and helium ash removal. Turn off the fuelling and the reactor will stop within  $\sim 1$ s and so dangerous reactor conditions, such as meltdowns, are impossible. And another often overlooked advantage being that the majority of the fuel needed for a fusion reactor to function is abundantly available in any water source on Earth [14]. This eliminates any geopolitical frictions and/or conflicts that may arise from the resource scarcity that is usually associated with almost all other fuel-based methods of power generation. In specific comparison to nuclear fission, the potential for proliferation of material that may be used in an offensive capacity is significantly reduced(or possibly eliminated) when dealing with nuclear fusion.

Nuclear fusion reactors would also be portable in the sense that they could feasibly be located anywhere on or off the planet, assuming sufficient volume was available to occupy, this would likely not exceed the volume used by conventional fission reactors. Flexibility is an aspect that fusion reactors are lacking in when compared to fossil fuels. However given that battery technology has allowed, at least in small scales, for the possibility of shifting away from fossil fuels in almost every sector of transportation(save aviation) the electricity generated from fusion reactors could facilitate the obsolescence of fossil fuels as a means of powering transportation.

This discussion hopefully highlights the usefulness of nuclear fusion as an energy source. The feasibility of nuclear fusion to contribute to combating climate change is a discussion that has been gaining more traction as fusion reactors become a more viable proposition. As an example the idea of fusion reactors being used in geographic locations with low renewable resources(wind, solar, etc.) to offset CO<sub>2</sub> emissions has been investigated

and found to be viable[15]. Given the advantages it is an avenue worth pursuing if not for addressing climate change then for the energy demand that is likely to be needed afterwards. After all, the Earth’s population is projected to hit 9 billion shortly after 2050[16]. With such an increase in energy demand a reliable high-density baseload is going to be undeniably necessary. Conventional nuclear fission reactors could make up the shortfall and provide low-emission electricity but the resources for these reactors are finite and will also run out(estimates suggest  $\sim 1000$  years) not to mention the inherent instability and lack of public and political will surrounding this particular method of energy generation.

To understand the difficulties associated with nuclear fusion one has to understand the physics of the medium in which fusion will happen – plasma.

### 1.3 Plasma Physics - Basic Parameters

A plasma is a partially or fully ionised gas. In this state the electrons and ions are unbound, but since both components are electrically charged, they are subject to electromagnetic fields, both external and self-generated. The electromagnetic force is so strong that no significant violation of quasi-neutrality,  $n_e = Zn_i$ , is allowed. Minor deviations are allowed and the characteristic length-scale over which these deviations occur is known as the Debye-length. The force between minor separation of charges can be given per unit area as:  $F = qE = (nde)E = (nde)^2/\epsilon_0$ , where  $d$  is the thicknesses of the sheets of charges adjacent to each other. Equating the potential of such a charge configuration,  $Fd$  with the one dimensional internal energy,  $dnk_BT$  and solving for  $d$  gives:

$$d \equiv \lambda_D = \left( \frac{\epsilon_0 k_B T}{ne^2} \right)^{\frac{1}{2}} \quad (1.2)$$

This length signifies the limit of any given particle’s influence on the rest of the plasma. Any deviation from neutrality at a scale larger than the Debye length will cause the plasma to react to preserve quasi-neutrality. However any deviation below this scale can persist and causes particles to respond via Coulomb forces. A qualitative description of a characteristic test parameter for plasmas known as the “plasma parameter” can be defined in terms of Debye length, chiefly if the Debye length of a given system of particles is smaller than the average separation between the particles then the system is not a plasma.

The plasma frequency is another characteristic parameter of a plasma. The frequency can be extracted by considering that the induced electric field generates simple harmonic



motion, since it is a attractive inverse-square law force. It can be derived by looking at the motion of a single charged particle under the influence of this electric field in one dimension:

$$\frac{\partial^2 x}{\partial t^2} = -\frac{q}{m}E = -\frac{nq^2}{m\epsilon_0}x = -\omega_p^2 x \quad (1.3)$$

$$\omega_p = \left(\frac{nq^2}{m\epsilon_0}\right)^{\frac{1}{2}} \quad (1.4)$$

In magnetised plasmas another characteristic length scale emerges due to the dynamics of the charges in the magnetic field. The equation of motion for a charged particle in a magnetic field pointing in the z-direction and no background electric field is:

$$\frac{d\vec{v}}{dt} = \frac{q}{m}(\vec{v} \times \vec{B}) \quad (1.5)$$

$$= (\omega_c v_y, -\omega_c v_x, 0)_T \quad (1.6)$$

$$\text{where: } \omega_c = \frac{qB}{m} \quad (1.7)$$

Taking the second derivative of the  $x$  and  $y$  components gives:

$$\frac{d^2 v_x}{dt^2} = \omega_c \frac{dv_y}{dt} = -\omega_c^2 v_x \quad (1.8)$$

$$\frac{d^2 v_y}{dt^2} = \omega_c \frac{dv_x}{dt} = -\omega_c^2 v_y \quad (1.9)$$

Solving for  $v_x$ ,  $v_y$  and then for  $x$ ,  $y$  gives:

$$x = -r_L \cos \omega_c t \quad (1.10)$$

$$y = r_L \sin \omega_c t \quad (1.11)$$

$$\text{where: } r_L = \frac{v_{\perp}}{\omega_c}, \quad v_{\perp} = \sqrt{v_x^2 + v_y^2} \quad (1.12)$$

Finally given the fact that the charged particles in a plasma can contribute to background electromagnetic fields, Maxwell's equations need to be incorporated into any description

of plasma:

$$\vec{\nabla} \times \vec{B} = \mu_0 j + \epsilon_0 \mu_0 \frac{\partial \vec{E}}{\partial t} \quad \text{where } j \text{ is current density} \quad (1.13)$$

$$\vec{\nabla} \times \vec{E} = -\frac{\partial \vec{B}}{\partial t} \quad (1.14)$$

$$\vec{\nabla} \cdot \vec{B} = 0 \quad (1.15)$$

$$\vec{\nabla} \cdot \vec{E} = \frac{\rho}{\epsilon_0} \quad \text{where } \rho \text{ is charge density} \quad (1.16)$$

## 1.4 Plasma Physics - Drifts and invariants

The motion of a charged particle can be affected by external forces and the motion can be expressed as the motion of the guiding centre of the charged particle trajectory (ie. the centre of gyration of the particle), this is since these drifts generally happen on a much larger scale than the Larmor radius. For example, a parallel electric field (in the direction of the magnetic field) would accelerate the particle along the direction of the magnetic field. Similarly a parallel gradient in the magnetic field would accelerate the particles towards regions of lower magnetic field strength (against the gradient). For all other drifts (except for slowly time-varying varying electric field) a generalisation of the drift velocity definition can be made:

$$v_d = \frac{\vec{F} \times \vec{B}}{qB^2} \quad (1.17)$$

then simply substitute in the various forces:

$$\vec{F} = q\vec{E} \quad \text{for } \vec{E} \times \vec{B} \text{ drift} \quad (1.18)$$

$$\vec{F} = -\frac{1}{2}mv_{\perp}^2 \frac{\vec{\nabla} B}{B} \quad \text{for } \vec{\nabla} B \text{ drift} \quad (1.19)$$

$$\vec{F} = \frac{mv_{\parallel}^2}{R} \hat{R} \quad \text{for curvature drift} \quad (1.20)$$

For a slowly time-varying electric field the  $\vec{E} \times \vec{B}$  drift velocity can be used:

$$v_d = \frac{\vec{E}(t) \times \vec{B}}{B^2} \quad \rightarrow \quad \frac{dv_d}{dt} = \frac{d}{dt} \left( \frac{\vec{E}(t) \times \vec{B}}{B^2} \right) \quad \rightarrow \quad \vec{F}_p = -m \frac{d}{dt} \left( \frac{\vec{E}(t) \times \vec{B}}{B^2} \right) \quad (1.21)$$

$$\text{Substituting } \vec{F}_p \text{ into Eq. (1.17): } v_p = -\frac{m}{qB^2} \frac{((d\vec{E}/dt) \times \vec{B}) \times \vec{B}}{B^2} = \frac{m}{qB^2} \frac{d\vec{E}}{dt} \quad (1.22)$$

Since ions and electrons drift in the opposite direction due to polarization drift a polarization current can be set up.

An adiabatic invariant of motion in this case is the magnetic moment:

$$\mu = \frac{\frac{1}{2}mv_{\perp}^2}{B} \quad \rightarrow \quad \frac{d\mu}{dt} = 0 \quad (1.23)$$

## 1.5 Plasma Physics - Kinetic description

For the sake of tractability the plasma can be described as a statistical system as opposed to individual particles. Kinetic theory is such a description, one can use a single particle distribution function in position  $\vec{q}$ , canonical momentum  $\vec{P}$  and time  $t$  and introduce terms to provide effects of multi-particle interactions (collisions for example). This distribution function  $f$  describes the probability of a particle at time  $t$  being at position  $\vec{q}$  and having a canonical momentum  $\vec{p}$ . And given the principle of conservation of particles in a given system it follows:

$$\frac{df}{dt} = \frac{\partial f}{\partial t} + \dot{\vec{q}} \cdot \vec{\nabla}_q f + \dot{\vec{p}} \cdot \vec{\nabla}_p f = 0 \quad (1.24)$$

Reassigning  $\vec{q}$  and  $\vec{p}$  for  $\vec{x}$  and  $m\vec{v}$  gives the Vlasov equation (note that  $q$ , the non-vector notation, represents charge *not* position):

$$\frac{\partial f}{\partial t} + \vec{v} \cdot \vec{\nabla}_x f + \frac{q}{m} (\vec{E} + \vec{v} \times \vec{B}) \cdot \vec{\nabla}_v f = 0 \quad (1.25)$$

$$\text{where } \dot{\vec{p}} = m\dot{\vec{v}} = q(\vec{E} + \vec{v} \times \vec{B}) \quad (1.26)$$

This neglects collisions but this can be rectified by introducing a term on the RHS to give the Fokker-Planck equation:

$$\frac{\partial f}{\partial t} + \vec{v} \cdot \vec{\nabla}_x f + \frac{q}{m} (\vec{E} + \vec{v} \times \vec{B}) \cdot \vec{\nabla}_v f = \left( \frac{\partial f}{\partial t} \right)_c \quad (1.27)$$

The fields present in this equation are the average fields, whereas the effects of the instantaneous fields are folded into the collision term as the contribution of many small incident angle binary coulomb collisions. This term conserves particle number, momentum and energy but does act as a source of entropy. From this term resistivity in the plasma is realised as well as transfer of energy between particles(allowing thermal equilibration). Various averages and assumptions can be applied to the Fokker-Planck equation to obtain a simplified(if restricted) equation that is more relevant to particular phenomena. For example, the gyro-kinetic equation takes into account the effects of electromagnetic fields that vary on a scale smaller than the Larmor radius by averaging their contributions over the gyration of the particles(sometimes known as the Larmor orbit). Another property of the kinetic description is that taking moments of the Fokker-Planck equation recovers the fluid equations governing large scale physics of plasmas.

## 1.6 Plasma Physics - Fluid Descriptions

A fluid description of the plasma is useful in that it further reduces the number of variables needed for description of the plasma. The Fokker-Planck equation evolves one quantity which is a function of 7 variables,  $f(\vec{x}, \vec{v}, t)$ . Taking moments of the Fokker-Planck equation yields three fluid properties that describe the plasma and they are recovered as such:

$$n = \int f(\vec{x}, \vec{v}', t) d\vec{v}' \quad (1.28)$$

$$\vec{v} = \frac{1}{n} \int \vec{v}' f(\vec{x}, \vec{v}', t) d\vec{v}' \quad (1.29)$$

$$\vec{P} = m \int (\vec{v}' - \vec{v})(\vec{v}' - \vec{v}) f(\vec{x}, \vec{v}', t) d\vec{v}' \quad (1.30)$$

These properties are now dependent on only 4 variables,  $n(\vec{x}, t)$ ,  $\vec{v}(\vec{x}, t)$  and  $\vec{P}(\vec{x}, t)$ . The properties are number density(can be turned into mass density, charge density by adding pre-factors), fluid velocity(can be turned into current density by adding pre-factors) and pressure, which is presents as a tensor but can be given as a scalar when the distribution function is isotropic. It is then defined as:

$$p = \frac{1}{3} m \int (\vec{v}' - \vec{v})^2 f(\vec{x}, \vec{v}, t) \quad (1.31)$$

The density, velocity and pressure definitions are known as the 0<sup>th</sup>, 1<sup>st</sup> and 2<sup>nd</sup> moments of the distribution function respectively. Taking the 0<sup>th</sup> moment of the Fokker-Planck equation gives:

$$\frac{\partial n}{\partial t} + \int \vec{v}' \cdot (\vec{\nabla}_{\vec{x}} f) d\vec{v}' + \frac{1}{m} \int \vec{F} \cdot (\vec{\nabla}_{\vec{v}'} f) d\vec{v}' = \int \left( \frac{\partial f}{\partial t} \right)_c d\vec{v}' \quad (1.32)$$

$$\frac{\partial n}{\partial t} + \vec{\nabla}_{\vec{x}} \cdot \int \vec{v}' f d\vec{v}' + \frac{1}{m} \int f \vec{F} \cdot d\vec{S} = 0 \quad (1.33)$$

$$\frac{\partial n}{\partial t} + \vec{\nabla}_{\vec{x}} \cdot (n\vec{v}) = 0 \quad (1.34)$$

The collision term on the RHS goes to zero assuming that particle number doesn't change due to collisions and the contribution from the Lorentz force  $\vec{F}$  goes to zero by using integration by parts and the divergence theorem to show that in the limit  $\vec{v} \rightarrow \infty$ , the distribution function  $f \rightarrow 0$  faster than  $|\vec{S}| \propto v^2 \rightarrow \infty$ . The final equation is the familiar continuity equation. A similar procedure can be used to obtain the momentum equation by taking the 1<sup>st</sup> moment of the Fokker-Planck equation and multiplying by mass  $m$ :

$$m \frac{\partial}{\partial t} (n\vec{v}) + m \int \vec{v}' \vec{v}' \cdot (\vec{\nabla}_{\vec{x}} f) d\vec{v}' + \int \vec{v}' \vec{F} \cdot (\vec{\nabla}_{\vec{v}'} f) d\vec{v}' = m \int \vec{v}' \left( \frac{\partial f}{\partial t} \right)_c d\vec{v}' \quad (1.35)$$

$$m \frac{\partial}{\partial t} (n\vec{v}) + m \vec{\nabla}_{\vec{x}} \cdot \int \vec{v}' \vec{v}' f d\vec{v}' + \int \vec{v}' f \vec{F} \cdot d\vec{S} - \int \vec{v}' f (\vec{\nabla}_{\vec{v}'} \cdot \vec{F}) d\vec{v}' - \int f \vec{F} (\vec{\nabla}_{\vec{v}'} \cdot \vec{v}') d\vec{v}' = \vec{R} \quad (1.36)$$

$$m \frac{\partial}{\partial t} (n\vec{v}) + m \vec{\nabla}_{\vec{x}} \cdot \int ((\vec{v}' - \vec{v}) + \vec{v}) ((\vec{v}' - \vec{v}) + \vec{v}) f d\vec{v}' - n\vec{F} = \vec{R} \quad (1.37)$$

$$m \frac{\partial}{\partial t} (n\vec{v}) + \vec{\nabla}_{\vec{x}} \cdot \vec{P} + m \vec{\nabla}_{\vec{x}} \cdot (n\vec{v}\vec{v}) - n\vec{F} = \vec{R} \quad (1.38)$$

To note the mixed term from the expansion of  $((\vec{v}' - \vec{v}) + \vec{v})((\vec{v}' - \vec{v}) + \vec{v})$  disappears when averaged over  $\vec{v}'$  since  $O(\vec{v}' - \vec{v})$  represents thermal fluctuations which average to 0. Expanding all terms in the momentum equation by using the product rule gives:

$$mn \frac{\partial \vec{v}}{\partial t} + m\vec{v} \frac{\partial n}{\partial t} + mn(\vec{v} \cdot \vec{\nabla}_{\vec{x}}) \vec{v} + m\vec{v} (\vec{\nabla}_{\vec{x}} \cdot (n\vec{v})) + \vec{\nabla}_{\vec{x}} \cdot \vec{P} - n\vec{F} = \vec{R} \quad (1.39)$$

$$mn \left( \frac{\partial \vec{v}}{\partial t} + (\vec{v} \cdot \vec{\nabla}_{\vec{x}}) \vec{v} \right) = -\vec{\nabla}_{\vec{x}} \cdot \vec{P} + n\vec{F} + \vec{R} \quad (1.40)$$

As can be seen, each  $n^{\text{th}}$  moment of the Fokker-Planck equation requires a  $(n+1)^{\text{th}}$  moment. This necessitates some simplification to close the set. An approximation that can close this set is that of adiabatic behaviour. This leads to the MHD model which

can be evaluated by changing notation slightly by converting  $mn \rightarrow \rho$ ,  $qn \rightarrow \rho_c$ ,  $qn\vec{v} \rightarrow \vec{j}$  and treating  $\vec{\vec{P}}$  as a scalar  $p = \frac{1}{3}Tr(\vec{\vec{P}})$ :

$$\frac{\partial \rho}{\partial t} = -\vec{\nabla}_{\vec{x}} \cdot (\rho \vec{v}) \quad (1.41)$$

$$\rho \left( \frac{\partial \vec{v}}{\partial t} + (\vec{v} \cdot \vec{\nabla}_{\vec{x}}) \vec{v} \right) = -\vec{\nabla}_{\vec{x}} p + (\rho_c \vec{E} + \vec{j} \times \vec{B}) + \vec{R} \quad (1.42)$$

$$\frac{d}{dt}(p\rho^{-\gamma}) = 0 \rightarrow \text{using continuity equation} \rightarrow \frac{dp}{dt} = -\gamma p(\vec{\nabla}_{\vec{x}} \cdot \vec{v}) \quad (1.43)$$

$$\vec{j} = \frac{\vec{\nabla}_{\vec{x}} \times \vec{B}}{\mu_0} \quad (1.44)$$

$$\frac{\partial \vec{B}}{\partial t} = -\vec{\nabla}_{\vec{x}} \times \vec{E} \quad (1.45)$$

$$\vec{E} + \vec{v} \times \vec{B} = \eta \vec{j} = \vec{R}/qn \quad \text{where } \eta \text{ is resistivity} \quad (1.46)$$

Resistivity is defined via Ohm's Law and a new scalar is introduced,  $\eta$ . Neglecting resistivity and any other effects of particle interaction leads to Ideal MHD. The assumptions that lead to the MHD model are relatively mild, however more radical assumptions can also be made to close the set of equations, such as zero electron mass or in the case of the Braginskii two-fluid description[17], subsonic flows in the plasma.

The need for a closure of the set of equations is still necessary in this case since the Braginskii description does not treat pressure as a scalar. The result is a need for an assumptive definition of the pressure tensor( $\vec{\vec{P}}$ ) and the vector heat flux( $\vec{q}$ ). The actual calculation of these variables is more involved and beyond the scope of this thesis but in brief it involves accounting for the collisional term in the Fokker-Planck equation. Even through further assumptions yield an expression, this includes empirical pre-factors for some terms. The approach for deriving the new set of equations involves splitting the different variables into those for individual species. Furthermore another assumption is that the plasma distribution can be defined as a perturbed Maxwellian,  $f = f_0 + f_1$ , where  $f_0$  is a Maxwellian distribution:

$$f_0 = \frac{n_\alpha}{(2\pi T_\alpha/m_\alpha)^{1.5}} \exp\left(-\frac{m_\alpha}{2T_\alpha}(\vec{v}' - \vec{v})^2\right) \quad (1.47)$$

The Fokker-Planck equation can then be expanded to yield a new set of equations. The continuity equation is largely unchanged but is now expressed separately for each species:

$$\frac{\partial n_\alpha}{\partial t} = -\vec{\nabla}_{\vec{x}} \cdot (n_\alpha \vec{v}_\alpha) \quad (1.48)$$

The momentum equation is changed to split the pressure tensor into a scalar pressure  $p$  and the “strain” tensor:

$$\vec{\Pi}_{ij} = m \int \left( (\vec{v}' - \vec{v})_i (\vec{v}' - \vec{v})_j - \frac{(\vec{v}' - \vec{v})^2}{3} \vec{I}_{ij} \right) f(\vec{x}, \vec{v}, t) d\vec{v}' \quad (1.49)$$

, which is related to the pressure tensor as:  $\vec{P}_{\alpha ij} = p_\alpha \vec{I}_{ij} + \vec{\Pi}_{\alpha ij}$ .

$$n_\alpha m_\alpha \frac{d\vec{v}_\alpha}{dt} = -\vec{\nabla}_{\vec{x}} p_\alpha - \frac{\partial}{\partial x_j} \vec{\Pi}_{\alpha ij} + n_\alpha \vec{F}_\alpha + \vec{R}_\alpha \quad (1.50)$$

The new energy conservation equation, which replaces the ideal gas law interpretation, is:

$$\text{where: } T_\alpha = \frac{1}{n_\alpha} \int \frac{m_\alpha}{3} (\vec{v}' - \vec{v}_\alpha)^2 f_\alpha d\vec{v}' \quad (1.51)$$

$$\frac{3}{2} n_\alpha \frac{d}{dt} (T_\alpha) = -p_\alpha \vec{\nabla} \cdot \vec{v}_\alpha - \vec{\Pi}_\alpha : \vec{\nabla} \vec{v}_\alpha - \vec{\nabla} \cdot \vec{q}_\alpha + Q_\alpha \quad (1.52)$$

The quantity  $\vec{q}_\alpha$  is the heat flux associated with a given species of particles, the quantity  $Q_\alpha$  indicates heat exchange between the species  $\alpha$  and other species. Further extensions of MHD can be found in Tokamaks, J. Wesson[18]

## 1.7 Fusion Power

Examining the energetics of a fusion reactor more closely, the total energy inside a plasma can be defined as  $W = 3nTV$ , where  $k_B$  is set to 1,  $n$  is the average plasma number density,  $T$  is the average plasma temperature and  $V$  is the plasma volume. The rate of energy loss in the system can be described as  $P_{\text{loss}} = W/\tau$ , where the confinement time  $\tau = W/P_{\text{heating}}$ . One can then split the heating power of the plasma into externally supplied heat and internal heating due to charged particles produced in the fusion reactions,  $P_{\text{heating}} = P_{\text{ext}} + P_{\text{ch}}$ . The heating power from the charged particles is defined as  $P_{\text{ch}} = \frac{1}{4}n^2\langle\sigma v\rangle\epsilon_{\text{ch}}V$ , here  $\sigma$  is the cross-section associated with the two particle species being used as fuel(as seen in Fig. 1.1) and  $\epsilon_{\text{ch}}$  is the energy released in said given fusion reaction. Now examining required external heating power:

$$P_{\text{heating}} = \left( \frac{3nT}{\tau} - \frac{1}{4}n^2\langle\sigma v\rangle\epsilon_{\text{ch}} \right) < 0 \quad (1.53)$$

The inequality indicates the necessary condition for self-sustenance of the plasma energy solely through charged particles produced by fusion, rearranging gives:

$$n\tau > \frac{12T}{\epsilon_{\text{ch}}\langle\sigma v\rangle} \quad (1.54)$$

This condition known as the Lawson criterion however still has a temperature dependence on the L.H.S., given that  $\langle\sigma v\rangle \propto T^2$  one can multiply both sides by  $T$  to make the L.H.S.  $nT\tau$  which is known as the triple product. In order to obtain an ignition condition one simply has to pick a relevant fusion reaction. In a reactor the main objective is to increase the temperature of the plasma sufficiently to allow the particle velocities to overcome Coulomb repulsion, to that end it is desirable to pick two fusion reactants that have low mass and low charge. Fortunately elements(and their isotopes) that satisfy these 2 requirements also yield products which have a much higher binding energy than the reactants. This would indicate that hydrogen nuclei(protons) might be the most suitable however as it turns out the balance between needing low mass for high temperatures and high mass, low charge for overcoming Coulomb repulsion dictates that isotopes(versions of hydrogen with extra neutrons) of hydrogen are preferable. There are two main isotopes that are worth considering in the context of fusion, deuterium(1 extra neutron) and tritium(2 extra neutrons). The primary fusion reaction that would take place with these two isotopes as fuel would be:



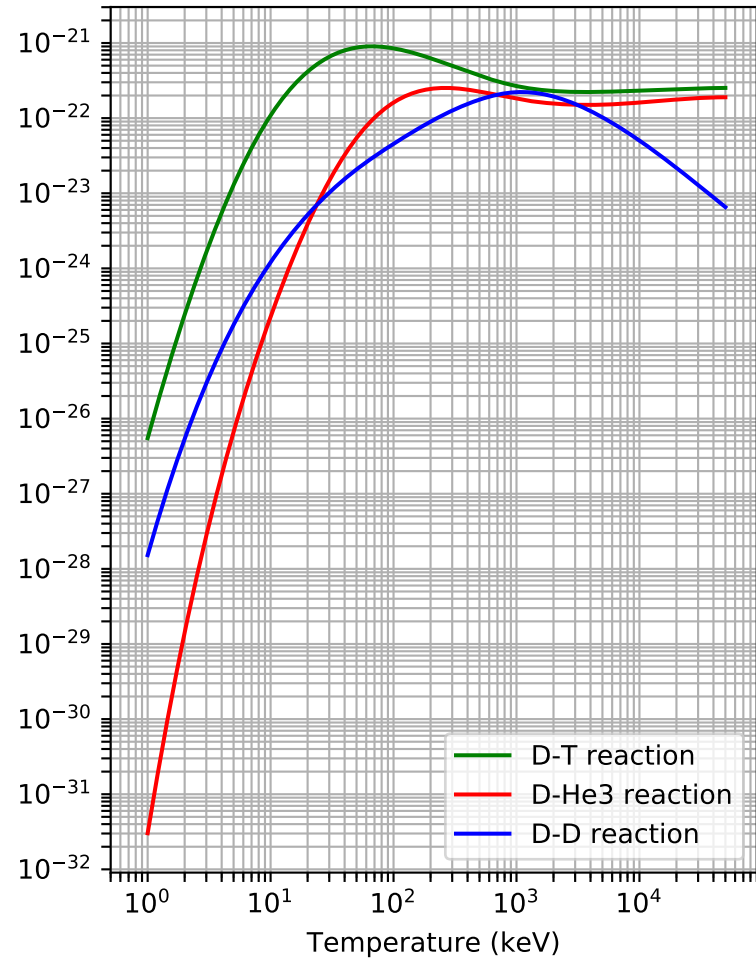


Figure 1.1: A few examples of cross-section profiles for different species pairings considered for fusion.[3]



This reaction produces 17.6 MeV[3] of excess(kinetic) energy,  ${}^4_2He$  takes 3.5 MeV of energy and the  ${}^1_0n$  takes 14.1 MeV of energy. In a plasma only the  ${}^4_2He$  particle is going to provide heating to the plasma as it is the only product that is charged. The neutrons stream out and their energy must be captured in another fashion. The  $\epsilon_{ch}$  now becomes  $\epsilon_{\alpha} = 3.5\text{MeV}$  which is the heating power from the alpha particles. The condition relating to the triple product now becomes:

$$nT\tau > 3 \times 10^{21} \text{m}^{-3} \text{keV s} \quad (1.56)$$

One can pick any combination of  $n$ ,  $T$  and  $\tau$  that is desired and check for feasibility of self-sustenance. An example could be ,  $n = 10^{20} \text{m}^{-3}$ ,  $T = 10 \text{keV}$  and  $\tau = 3 \text{s}$ . Increasing density and temperature and reducing confinement time can also satisfy this limit although by definition a much shorter confinement time would lead a reactor design away from steady-state and into pulsed state as is the case for ICF concepts(inertial confinement fusion). This ignition condition however simply sets the condition for theoretical break-even, the number can be lowered by (re-circulating the energy from the neutrons into either heating or operating the machine) or can be increased by requiring meaningful electrical output to the grid. Regardless, for feasibly operating in the range of the temperatures and densities mentioned above, one cannot simply contain the plasma using conventional materials. There are no materials that can withstand the temperatures and therefore another method of confinement must be sought.

## 1.8 Magnetic Confinement Fusion (MCF)

One solution is to confine the plasma using magnetic fields. Plasma particles gyrate around magnetic field lines and can therefore be effectively guided away from the walls of the reactor. Tokamaks are devices that make use of such magnetic fields and are, at the moment, the most promising avenue for achieving a ignition-capable fusion reactor. In a tokamak a doughnut-shaped vacuum vessel is where the plasma resides during operation. The shape and structure of certain major components can be seen in Fig 1.2. The geometrical labelling of a typical tokamak is given in Fig. 1.3, where  $R_0$  and  $a$  are major and minor radius respectively. The toroidal fields coils generate a magnetic field that forms field lines along the toroidal direction of the tokamak. The particles can freely move along these field lines but cannot easily cross them. The primary transformer

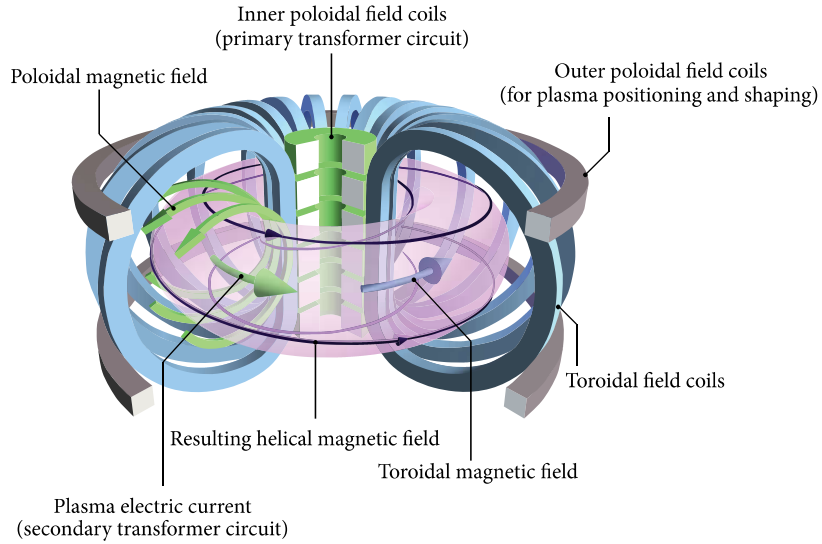


Figure 1.2: A schematic of a tokamak.[4]

circuit at the centre of the machine induces a current in the plasma which follows the same direction as the toroidal field lines. Though the plasma is quasi-neutral, the ions are heavier than the electrons and are thus travel at slower speeds, this mismatch of charge movement produces a plasma current. This current in turn generates its own poloidal field and this combines with the toroidal field to twist the field lines into helical trajectories. As a result the particles can travel both inwards, in major radius, towards the central column and outwards, towards the edge of the device. The toroidal field gets weaker as you travel outwards, in major radius, and so it is advantageous to shape the toroidal field coils so that they produce field lines that keep the particles close to the central column for longer. Therefore even though for a circular cross-section tokamak the toroidal field coils would be circular, for most tokamaks they are shaped like the letter “D” as shown in Fig. 1.2. The extra poloidal field coils outside the toroidal field coils are mostly just used for shaping the plasma further. The heating of the plasma is dependent on the temperature regime that is required. For the initial ionisation of the gas injected into the vacuum vessel, Ohmic heating from resistance to the plasma current induced

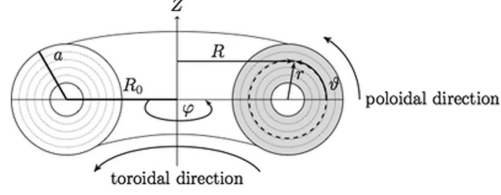


Figure 1.3: Labelling of a typical tokamak geometry.[5]

by the primary transformer circuit is used. As the temperature of the plasma increases the resistance of the plasma drops and Ohmic heating is now no longer viable. For further heating there are multiple options which can be used in combination or isolation. These are NBI(Neutral-Beam-Injection), ICRH(Ion-Cyclotron-Resonance-Heating) and ECRH(Electron-Cyclotron-Resonance-Heating). NBI is where the fuel(deuterium-tritium or just deuterium) is ionised outside the vacuum vessel and accelerated using electric fields and then neutralised as it is injected into the plasma. It is always travelling at a faster speed than the average thermal speed of the plasma and as it is re-ionised and the plasma thermalises, the average temperature in the system increases. The other two methods use a similar modification of the distribution function of the plasma to change the temperature but instead of introducing new particles, they instead modify the speed of existing ions and electrons and then allow the plasma to thermalise to a new equilibrium. The mechanism for these indirect heating schemes is known as Landau-damping which is a form of collision-less dissipation of plasma waves(induced by external EM waves) by individual plasma particles(that have a speed that is near or at the transverse speed of the induced plasma wave). Electron cyclotron current drive is also used in some situations not to heat the plasma but to increase the plasma current. This can improve certain limits on tokamak operation and/or reduces the burden on the primary transformer circuit.

With good confinement and in the absence of any instabilities the particles might cause, the alpha particles do indeed deposit their energy into the plasma but exhausting them is a challenging problem. As of right now the method involves exhausting some of the bulk plasma(which will contain some of the “ash”) at the edge and then re-injecting fresh fuel to facilitate a slow flush of the helium “ash” out of the system. This issue of impurity build-up is especially relevant in the design of future reactors that are likely to operate in the so-called H-mode(high-confinement mode). As opposed to the more accessible

L-mode, the H-mode is more difficult to induce and depending on the dimensions of the tokamak can improve confinement time by a factor of 2 or more. This is done by establishing internal transport barriers which inhibit radial transport of energy. Whilst this is desirable, it also stops impurities escaping the core plasma. The part of the plasma that is most affected by this exhausting mechanism resides in an area of the vacuum vessel known as the scrape-off layer(SOL). The plasma in this area has field lines which do not close but are instead shaped to terminate in a region of the tokamak known as the divertor. The divertor experiences high heat-flux comparable to a re-entering space craft( $\sim 10\text{MWm}^{-2}$  [19]) and the design of a capable divertor is one of the main issues that needs to be addressed for a commercial reactor.

In terms of operational constraints of a conventional tokamak, there are various limits. The triple product mentioned earlier requires a set combination of density( $n$ ), temperature( $T$ ) and confinement time( $\tau$ ). The confinement time is largely dependent on the geometry and magnetic configuration of any given device and is usually empirically derived using scaling relations or extrapolations of relevant data. The beta limit is largely dictated by the magnetic field strength(in the toroidal direction). There is another constraint known as the Greenwald limit[20] which limits the maximum density inside the device and is dependent on the plasma current magnitude. If the geometry of the magnetic fields(and consequently the vacuum vessel) is changed so that the ratio between major and minor radius(known as the aspect ratio) decreases then the scaling laws can be strongly modified. The confinement time scaling for a small aspect ratio tokamak has a high dependence on toroidal field,  $B_T$  [21][22], meaning good confinement can be achieved with moderate fields. These so called spherical tokamaks(due to their more compact toroidal shape) are of interest for future reactor designs, this is demonstrated by the commissioning of a design study in the UK for STEP(Spherical Tokamak for Energy Production)[23].

## 1.9 Spherical Tokamak

This change in aspect ratio introduces both advantages and disadvantages. One of the advantages it introduces is that since the particles have to travel a greater length (and therefore spend more time) on the high field side they are generally better confined. This is since the local magnetic field pressure is high enough that more plasma pressure can be incorporated without the  $\beta$ (the ratio between the plasma pressure and the magnetic field pressure) exceeding any limits. This leads to higher average  $\beta$  across the device and therefore better performance overall. This can be further augmented by employing a high

safety factor( $q$ ) which increase the number of poloidal rotations a field line undergoes before a full toroidal rotation is completed. A disadvantage in terms of engineering which could also be seen as an advantage is the compactness of the reactor design. The more compact it is the fewer materials are needed and the smaller the reactor's footprint. But the compactness means that there is less room for toroidal field coils and/or a central solenoid for the primary transformer circuit. And even if a central solenoid and toroidal field coils can be designed to fit the restricted space, the protection for these components from the plasma(in the case of disruptions and/or instabilities) or from neutron radiation is also a challenge. For reference Table 1.1 shows a comparison of specifications between MAST(Mega-Ampere-Spherical-Tokamak) and JET(Joint European Torus) both of which are located at CCFE(Culham Centre for Fusion Research):

	JET	MAST
Major Radius( $R$ )	2.96m	0.85m
Minor Radius( $r$ )	1.25m	0.65m
Aspect Ratio( $A$ )	2.368	1.3
Toroidal Magnetic Field( $B_T$ )	3.45T	0.5T
Plasma Current( $I_p$ )	4.8MA	1MA

Table 1.1: Comparison of specifications of MAST and JET.[1][2]

## 1.10 Transport

Given the nature of confinement in tokamaks, gradients in density and temperature are introduced. These gradients in turn drive fluxes of particles and heat outwards(in minor radius). The purpose of transport theory is to calculate these fluxes. Treating the plasma as an ordinary fluid allows one to recover classical diffusive processes. The key difference in the case of plasma is that the time and length scales are relative to plasma properties. The particle and heat fluxes,  $\vec{\Gamma}$  and  $\vec{q}$  respectively, can be expressed as:

$$\vec{\Gamma} = -D\vec{\nabla}_{\perp}n_{\alpha} \quad (1.57)$$

$$\vec{q} = -n\chi\vec{\nabla}_{\perp}T_{\alpha} \quad (1.58)$$

where  $\alpha = e, i$  depending on whether the species of interest is electrons or ion. The scaling on the diffusion coefficient  $D$  follows as:

$$D \sim \nu(\delta x)^2 \quad (1.59)$$

The collision frequency,  $\nu$  varies for different collision types, but is generally much less than the cyclotron frequency for the relevant particle species in a magnetized plasma:

$$\nu_{ei} \ll \Omega_e \quad (1.60)$$

$$\nu_{ii} \ll \Omega_i \quad (1.61)$$

For clarity, the convention in this case is that  $\nu_{\alpha\beta}$  signifies the frequency of collisions between species causing  $\alpha$  to be scattered by  $\beta$ . It is appropriate to think of the frequency of collisions as being the frequency with which the particle trajectory changes significantly as a result of an average aggregate of multiple small-angle deflections due to Coulomb interactions. It is also useful to consider collision times, these scale as  $\tau_{\alpha\beta} \sim \nu_{\alpha\beta}^{-1}$ .

Looking now at particle diffusion across the magnetic field in the framework of a random-walk process, it is assumed that all internal plasma parameters that may lead to a diffusion of the guiding centre motion have length-scales of variation that are longer than the Larmor radius. Now considering a gradient in plasma density  $n$  in the x-direction, a flux of particles across the magnetic field (in the z-direction) due to electron-ion collisions can be estimated:  $\Gamma_x \sim -D_\perp(\partial n/\partial x)$ , where  $D_\perp \sim (\nu_{ei}\rho^2/2)$ .

Analysis of heat diffusion across the magnetic field involves considering a temperature gradient in the x-direction but uniform plasma density. The flux of heat is dominated by ion-ion collision and can be estimated as  $q = -n_i\chi(\partial T)/(\partial x)$  where  $\chi_i \sim (\rho_i^2\nu_{ii})$ . Heat conduction in the direction parallel to the magnetic field happens much faster (by a factor  $(\Omega\tau)^2$ ) but is not heavily involved in heat loss from the tokamak.

Considering particle and heat losses separately in a realistic spherical tokamak like MAST will yield quantities which will give an indication of expected confinement performance under the assumptions of classical diffusion. Taking the fluxes defined above to be through the surface area of a torus,  $4\pi^2rR$ , with a minor radius  $r$  and major radius  $R$ . A rough estimate for particle confinement time is then  $\tau_\Gamma = 4\pi^2rR/D_\perp \sim 120s$  for MAST-like tokamak. This is not consistent with the observed confinement time in MAST. Re-examining this confinement time by now and looking at the heat diffusion through the tokamak gives a different value:  $\tau_q = 4\pi^2rR/\chi_i \sim 1s$  this is also too large a value. Modifying this heat transport coefficient by considering the effect of particles trapped in the weak-field region of the tokamak in so-called "banana orbits" yields a value for  $\chi_i$  that is enhanced by a factor of  $\sqrt{2\epsilon}(B/B_p)^2$ . Here  $\epsilon = r/R$  is the inverse aspect ratio and  $B_p$  is the poloidal magnetic field. For a MAST-like tokamak this amounts to an enhancement by a factor of  $\sim 25$  which would decrease the new confinement time down to  $\tau_q \sim 0.04s \equiv 40ms$  which is much closer to the observed confinement time

in MAST. Further modifications to the particle diffusion coefficient must be made to account for anomalous radial transport arising from electrostatic fluctuations which lead to outward propagating turbulent eddies. The definition of this Bohm diffusion coefficient is part-empirically defined as:  $D_e^{\text{Bohm}} = T/(16eB)$ , for MAST-like conditions ( $B = 0.5T$  and  $T_e = 1keV$ ) this gives a value of  $D_e^{\text{Bohm}} \sim 125m^2/s$  which leads to a thousand-fold decrease of the classical particle diffusion confinement time:  $\tau_\Gamma \sim 0.1s \sim 100ms$  which is now in much better agreement with both  $\tau_q$  and the experimentally observed confinement time ranging from  $\tau_{\text{exp}} = 10 - 50ms$ .

The electrostatic fluctuations that cause this anomalous diffusion can be examined using the Hasegawa-Wakatani equations. The formal description of this model is that it is derived from the two-fluid Braginskii[17] equations with a non-adiabatic electron response due to electron-ion collisions along the direction of magnetic field. The resulting two coupled equations give the non-linear time-evolution of the vorticity(defined as  $\nabla_\perp^2 \phi$ ) and plasma density( $n$  which is the same for both electrons and ions due to quasi-neutrality.) This simplified model gives insight into drift-wave-turbulence and zonal flows and is useful for painting a qualitative picture of a localized region plasma(which is still large enough for fluid model assumptions to apply). The model assumes cold ions ( $T_i = 0$ ) and uniform electron temperature across the scale of the region being considered( $T_e \neq 0$ ,  $\vec{\nabla} \cdot T_e = 0$ ). Parallel ion velocity is also neglected here and quasi-neutrality is assumed. The normalization scales will be discussed further on. To start with, consider the perpendicular ion momentum equation(ion momentum equation projected in the direction perpendicular to the magnetic field):

$$m_i n \left( \frac{\partial}{\partial t} + \vec{v}_i \cdot \vec{\nabla}_\perp \right) \vec{v}_i = n q_i \left( -\vec{\nabla}_\perp \phi + \vec{v} \times \vec{B} \right) \quad (1.62)$$

Setting the L.H.S. to 0 and taking the curl with  $\vec{B}$  and rearranging gives:

$$\vec{v}_E = \frac{-\vec{\nabla} \phi \times \vec{B}}{B^2} \quad (1.63)$$

This is the lowest order velocity and crucially is identical for both ions and electrons since  $\vec{E} \times \vec{B}$  drift is independent of charge or mass. Note that collisions are ignored in this case. Substituting this velocity back into the perpendicular ion momentum equation gives:

$$\frac{d}{dt} (\vec{v}_E) = \frac{q_i}{m_i} \left( -\vec{\nabla}_\perp \phi + \vec{v} \times \vec{B} \right) \quad (1.64)$$



Taking the curl with  $\vec{B}$  and rearranging obtains the ion polarization drift,  $\vec{v}_{ip}$ :

$$\frac{d}{dt} (\vec{v}_E \times \vec{B}) = \frac{q_i}{m_i} (-\vec{\nabla}_\perp \phi \times \vec{B} - B^2 \vec{v}) \quad (1.65)$$

$$\vec{v}_{\perp,i} = \vec{v}_E + \frac{m_i}{q_i B^2} \frac{d}{dt} (\vec{\nabla}_\perp \phi) = \vec{v}_E + \vec{v}_{ip} \quad (1.66)$$

Now examining the perpendicular electron momentum equation:

$$m_e n \left( \frac{\partial}{\partial t} + \vec{v}_e \cdot \vec{\nabla}_\perp \right) \vec{v} = n q_e (-\vec{\nabla} \phi + \vec{v} \times \vec{B}) - T_e \vec{\nabla}_\perp n \quad (1.67)$$

Again setting the L.H.S. to 0 and taking the curl with  $\vec{B}$  and rearranging gives:

$$\vec{v}_{\perp,e} = \vec{v}_E - \frac{T_e}{n q_e} \frac{\vec{\nabla}_\perp n \times \vec{B}}{B^2} = \vec{v}_E + \vec{v}_{ed} \quad (1.68)$$

Here,  $v_{ed}$  is the electron diamagnetic drift. The calculation of this is simply to emphasize that the diamagnetic drift includes a  $\vec{\nabla}_\perp n$  in its definition which will be useful later. Moving on to the parallel electron momentum equation, examined with the same procedure as before (with collision included via a current term):

$$0 = -n q_e \vec{\nabla}_\parallel \phi - T_e \vec{\nabla}_\parallel n - q_e n \eta \vec{J}_\parallel \quad (1.69)$$

$$\vec{J}_\parallel = -\frac{T_e}{q_e \eta} \left[ \frac{\vec{\nabla}_\parallel n}{n} + \frac{q_e \vec{\nabla}_\parallel \phi}{T_e} \right] \quad (1.70)$$

To begin construction of the Hasegawa-Wakatani equations it is useful now to turn to the electron and ion continuity equations as defined by Braginskii, after simplification the electron continuity equation becomes:

$$\frac{\partial n}{\partial t} + (\vec{v}_E \cdot \vec{\nabla}_\perp) n + \frac{1}{q_e} \vec{\nabla}_\parallel \cdot \vec{J}_\parallel = 0 \quad (1.71)$$

For ions the continuity equation becomes:

$$\frac{\partial n}{\partial t} + (\vec{v}_E \cdot \vec{\nabla}_\perp) n + n (\vec{\nabla}_\perp \cdot \vec{v}_{ip}) = 0 \quad (1.72)$$

Due to quasi-neutrality one can now equate both equations and obtain an expression for the time-evolution of the vorticity( $\nabla_{\perp}^2 \phi$ ):

$$n(\vec{\nabla}_{\perp} \cdot \vec{v}_{ip}) = \frac{1}{q_e} \vec{\nabla}_{\parallel} \cdot \vec{J}_{\parallel} \quad (1.73)$$

$$\frac{d}{dt}(\nabla_{\perp}^2 \phi) = \frac{-q_i B^2}{q_e m_i n} \vec{\nabla}_{\parallel} \cdot \vec{J}_{\parallel} = \frac{B^2}{m_i n} \vec{\nabla}_{\parallel} \cdot \vec{J}_{\parallel} = -\frac{B^2 T_e \vec{\nabla}_{\parallel}}{m_i n q_e \eta} \cdot \left[ \frac{\vec{\nabla}_{\parallel} n}{n} + \frac{q_e \vec{\nabla}_{\parallel} \phi}{T_e} \right] \quad (1.74)$$

Now it is useful to define some normalization parameters:

$$\frac{e\phi}{T_e} \rightarrow \phi, \quad \frac{e\phi_1}{T_e} \rightarrow \phi_1, \quad \frac{n}{n_0} \rightarrow n, \quad \frac{n_1}{n_0} \rightarrow n_1, \quad n = n_0 + n_1, \quad \phi = \phi_0 + \phi_1 \quad (1.75)$$

$$\omega_{ci} t \rightarrow t, \quad \frac{x}{\rho_s} \rightarrow x, \quad \frac{y}{\rho_s} \rightarrow y, \quad \rho_s = \frac{1}{\omega_{ci}} \sqrt{\frac{T_e}{m_i}}, \quad \rho_s^2 = \frac{m_i T_e}{e^2 B^2}, \quad \omega_{ci} = \frac{eB}{m_i} \quad (1.76)$$

Re-configuring Eq. (1.71) and redefining  $(\vec{v}_E \cdot \vec{\nabla}_{\perp})f = (1/B_0)\{\phi, f\}$  (where  $\{\phi, f\} = (\partial\phi/\partial x)(\partial f/\partial y) - (\partial f/\partial x)(\partial\phi/\partial y)$ ) and defining  $\nabla_{\parallel}^2 = -k_z^2$  gives:

$$\omega_{ci} n_0 \frac{\partial n_1/n_0}{\partial t} + \frac{n_0 T_e}{e B_0 \rho_s^2} \left\{ \frac{e\phi}{T_e}, \frac{n_0 + n_1}{n_0} \right\} = -\frac{T_e k_z^2}{e^2 \eta} \left[ \frac{n_1}{n_0} - \frac{e\phi_1}{T_e} \right] \quad (1.77)$$

$$\text{Noting that: } \frac{T_e}{\rho_s^2 e B_0} = \omega_{ci}, \text{ and normalizing} \quad (1.78)$$

$$\frac{\partial n_1}{\partial t} = \alpha(\phi_1 - n_1) - \kappa \frac{\partial \phi}{\partial y} - \{\phi, n_1\} \quad (1.79)$$

$$\alpha = \frac{T_e k_z^2}{n_0 e^2 \eta \omega_{ci}}, \quad \kappa = -\frac{1}{n_0} \frac{\partial n_0}{\partial x} \quad (1.80)$$

The equation (1.79) is the first of the Hasegawa-Wakatani equations[24], the second concerns the time-evolution of the vorticity, applying the normalization to Eq. (1.74) yields:

$$\frac{\omega_{ci} T_e}{\rho_s^2 e} \frac{\partial \nabla_{\perp}^2 \phi}{\partial t} + \frac{T_e^2}{e^2 \rho_s^4} \{\phi, \nabla_{\perp}^2 \phi\} = -\frac{B^2 T_e k_z^2}{m_i n e \eta} \left[ \frac{n_1}{n_0} - \frac{e\phi_1}{T_e} \right] \quad (1.81)$$

$$\frac{\partial \nabla_{\perp}^2 \phi}{\partial t} = \alpha(\phi_1 - n_1) - \{\phi, \nabla_{\perp}^2 \phi\} \quad (1.82)$$

This is now the second Hasegawa-Wakatani equation. Now noting that  $\phi_0 = 0$  and suppressing the  $\sim$  on  $n_1$  as well as adding dissipative terms leads to:

$$\frac{\partial \nabla_{\perp}^2 \phi}{\partial t} = \alpha(\phi - n) - \{\phi, \nabla_{\perp}^2 \phi\} - D \nabla^4 (\nabla_{\perp}^2 \phi) \quad (1.83)$$

$$\frac{\partial n}{\partial t} = \alpha(\phi - n) - \kappa \frac{\partial \phi}{\partial y} - \{\phi, n\} - D \nabla^4 n \quad (1.84)$$

For the purposes of utilizing these equations for tokamak physics it is useful to subtract the poloidally averaged value of the perturbations in the  $\alpha$  term since the poloidal flows do not contribute to resistance in the direction of the magnetic field, and so now:

$$\alpha(\phi - n) \rightarrow \alpha(\phi_1 - n_1) \text{ where } \phi_1 = \phi - \langle \phi \rangle_y \text{ and } n_1 = n - \langle n \rangle_y$$

A straightforward linearization of the equations is possible and yields a dispersion relation that is dependent on the parallel resistivity; the inverse scale length of the density gradient and the inverse scale length of the perturbations themselves (the wavenumber) in the poloidal direction:

$$\phi_1 = \phi = |\phi| \exp(i(k_x x + k_y y - \omega t)) \quad (1.85)$$

$$n_1 = n = |n| \exp(i(k_x x + k_y y - \omega t)) \quad (1.86)$$

$$\frac{\partial \zeta}{\partial t} = \alpha(\phi_1 - n_1) - \{\phi, \zeta\} \quad (1.87)$$

$$\text{where } \zeta = \nabla_{\perp}^2 \phi = -(k_x^2 + k_y^2)\phi = -k^2 \phi \quad (1.88)$$

$$i\omega k^2 \phi = \alpha(\phi - n) - (-k_x k_y (-k_y^2 \phi^2)) \quad (1.89)$$

$$\frac{\partial n}{\partial t} = \alpha(\phi_1 - n_1) - \kappa \frac{\partial \phi}{\partial y} - \{\phi, n\} \quad (1.90)$$

$$-i\omega n = \alpha(\phi - n) - \kappa i k_y \phi - (-k_x k_y \phi n) \quad (1.91)$$

$$n = \left( \frac{\alpha - \kappa i k_y}{\alpha - i\omega} \right) \phi \quad \text{assuming } k_x^2 \ll k_y^2 \text{ then } k^2 = k_y^2 \quad (1.92)$$

$$i k_y^2 \omega \phi = \alpha \phi - \frac{\alpha(\alpha - \kappa i k_y)}{\alpha - i\omega} \phi \quad (1.93)$$

$$\omega = \frac{-i\alpha(k_y^2 + 1) \pm \sqrt{-\alpha^2(k_y^2 + 1) + 4i\alpha\kappa k_y^3}}{2k_y^2} \quad (1.94)$$

This solution is a useful starting point but it is not quite complete. Crucially it ignores the contribution that may or may not exist as a result of poloidal zonal flows ( $k_y = 0$ ,  $k_x \neq 0$ ). Zonal flows are important features in both realistic tokamaks as well as simplistic models such as the Hasegawa-Wakatani equations. Considering not just the effects of

these zonal flows on turbulence but also the effects of the toroidal geometry itself on the zonal flows(generation of Geodesic Acoustic Modes) is central to this thesis.

### **1.11 Thesis outline**

To this end the structure of the main body of the thesis consists of 3 chapters. Each chapter focuses on a slightly different aspect of the Zonal Flow-GAM(Geodesic Acoustic Mode)-Drift-Wave interaction. The first chapter is concerned with accounting for any contribution from the zonal flows on the drift waves as described in the Hasegawa-Wakatani model. The approach taken is similar to linearization but employs a technique to spatially average over the zonal flows in the system and subsequently analyse their impact on the drift-wave dispersion relation. The second chapter examines GAMs generated in the CENTORI simulation and validates their structure in the simulation as well as looking for distinct features that may be parallel to observations from experiments. The work in this chapter focuses mostly on linear GAM features. The third chapter is effectively an extension/expansion of the second chapter in so far as it investigates the non-linear and self interacting nature of GAMs in CENTORI.

## Chapter 2

# Drift-Wave instability in the presence of Zonal Flows

### 2.1 Introduction

Transport and its impact on radial transport is of fundamental importance for the confinement properties of tokamaks. In particular radial turbulent transport (in minor radius) is important to understand. In this case heat and particles are being lost from the containment system to the open-field Scrape-Off layer (SOL) which subsequently channels the plasma to the divertor. The loss of particles in general is concerning but can be compensated by appropriate fuelling. By contrast the loss of fast particles (high-temperature plasma) is more pressing. The heat carried away from the core of the tokamak by these particles is more difficult to efficiently replace without increasing the required energy output of the fusion process. Furthermore an increased heat flux on the divertor has its own challenges such as thermal management and impact on the materials in the divertor region. Therefore understanding this radial turbulent transport and subsequently controlling it would yield tangible improvements in plasma quality and heat content inside the tokamak. This turbulent transport is driven by micro-scale turbulence, as remarked in section 1.10). These are driven by density and temperature gradients perpendicular to the magnetic field. Drift-waves are generated by the density gradients and propagate perpendicularly to both the magnetic field and the direction of the density gradient. For example if the magnetic field vector was aligned with the z-axis and the density gradient was in the -x-axis (the density increases inwards towards the core) then the drift-wave would propagate in the positive y-direction. Due to quasi-neutrality, the density gradient is in both ion and electron density, however the response to the gradient

is pre-dominantly via electrons, and any coupling to electro-static potential is achieved through a non-adiabatic electron response. The mode then becomes unstable at a scale on the order of the hybrid gyro-radius  $\rho_s = \sqrt{m_i T_e}/eB$ . When the drift-waves grow to large amplitudes, their nonlinear self-interaction leads to drift-wave turbulence [25].

The micro-scale turbulent eddies can self-organise into zonal flows (ZF)[26][27]. In a tokamak these manifest as modes with long poloidal wavelengths (short way around the tokamak) a small finite radial wavelengths. Toroidal dynamics are relatively slow in comparison and therefore are not usually considered in the analysis of these phenomena (both for zonal flows and drift-waves). Zonal Flows are potentially very powerful in the ways that they can impact the onset/development of turbulence which drives radial particle and heat transport. Firstly, zonal flows can nonlinearly change the stability threshold for unstable modes arising from ITG (Ion Temperature Gradient) and resistive instabilities [28][29]. Secondly, turbulent eddies that are travelling radially outwards can be stretched and impeded as the zonal flows have a finite radial wavelength, this leads to a reduction of the turbulence level via dissipation of this modes before they can exit to the SOL[30]. Due to these effects, control of zonal flows provides a useful method for managing the turbulent transport in a tokamak. Specifically such an effect is currently observed and utilised in the L-H transition from a low confinement mode (L-mode) to a high confinement mode (H-mode), which is associated with a steeper density and pressure profile at the plasma edge. This transition is based on zonal flows suppressing turbulence[31].

The primary pathway for growth of zonal flows is non-linear, via momentum transfer of self-interacting turbulent structures which leads to shearing of small scale turbulence and the transfer of its energy to large scale sheared flows. One non-linear pathway is for a 4-wave interaction of drift-waves which can drive zonal flows via modulational instability [32][33][34]. Another method is via the Kelvin-Helmholtz instability of coherent radial structures known as radial streamers which via the instability decay to perpendicularly oriented zonal flows [35]. By contrast the decay of zonal flows can be caused by both linear and nonlinear processes. One linear method of decay is if zonal flows couple to compressible poloidal modes known as Geodesic Acoustic Modes (explored in more detail in Chapters 3 and 4). A field aligned component of these GAMs is Landau damped and due to the coupling, the zonal flows can also lose energy via this avenue. A nonlinear method of decay can be the tertiary Kelvin-Helmholtz instability of small scale fluctuations in ITG and resistive drift-wave turbulence [28][35].

This chapter will mainly focus on exploring another method of linear decay of zonal flows, chiefly via a Landau-damping-like interaction with drift-waves. This has been

explored in part previously using this motivation[28]. There is a subtle difference in the context in which this interaction is investigated in this chapter, mainly drift-wave instability in the presence of zonal flows rather than zonal flow stability. In the previous work by Numata et al.[28] they start with the Hasegawa-Wakatani model and linearise around an equilibrium that includes a zonal flows. They then check the growth rates for the zonal flows and the growth rates for the drift-waves. Furthermore the values for certain physical parameters (mainly the parallel electron resistivity) in the linearised Hasegawa-Wakatani model are taken at far extremes ( $\sim 0$ ). These are not justified in the region of interest for ZF-Drift-wave interactions, since they would imply low collisionality, which is more commonly found in the core at high temperatures. There is some exploration of realistic values, however these are limited to empirical results from a simulation without corroborating analytical predictions. The work presented in this chapter aims to obtain more general analytic predictions for the behaviour of the drift-wave instability in the presence of zonal flows and does so by building on and complementing the work presented in Numata et al.[28].

The method of investigating the drift-wave instability presented in this chapter yields a dispersion relation that is independent of any given shear profile and is dependent only on the zonal flow amplitude and the spatial scale in the radial direction (similar to a radial wavelength). The dispersion relation obtained is global since it is not dependent on the radial coordinate and the poloidal and toroidal coordinates are not involved in either the drift-wave description or the profile of the zonal flow. During the process of linearisation, Landau-like terms appear which present a resonant condition where the phase speed of drift-wave packet matches the advection speed of the zonal flow. This presents potential singularities which must be dealt with and the final expression is not easily analytically solvable and so is solved numerically. The results from this process are then compared to simulations of the same Modified Hasegawa-Wakatani model used in Numata et al.[28]. The main focus of comparison is in the near-resonant cases where drift-wave phase speed and zonal flow advection speed are close in value and investigate the departure of the frequencies and growth rates from the standard case (derived in the Thesis Introduction).

## 2.2 Methodology

### 2.2.1 Model Equations

The model used for the following analysis is the Modified Hasegawa-Wakatani model. The details of this model can be found in the Transport section of the Thesis Introduction. To briefly reiterate, the Hasegawa-Wakatani equations are derived from the standard two-fluid Bragiński equations (again details can be found in the Thesis Introduction) with a non-adiabatic electron response. The model is well suited to examining drift-wave turbulence and zonal flows in a localized region of the tokamak. The model equations are as follows:

$$\frac{\partial \zeta}{\partial t} = \alpha(\varphi_1 - n_1) - \{\varphi, \zeta\} \quad (2.1)$$

$$\frac{\partial n}{\partial t} = \alpha(\varphi_1 - n_1) - \kappa \frac{\partial \varphi}{\partial y} - \{\varphi, n\}. \quad (2.2)$$

Here  $\zeta = \partial^2 \varphi / \partial x^2 + \partial^2 \varphi / \partial y^2$  is the vorticity and  $n$  is the density of the plasma. The directions of  $x$  and  $y$  correspond to the radial and poloidal direction in a localized region at the edge of the tokamak plasma. The constant  $\kappa$  is defined as the value of the gradient of the background density,  $\partial \ln n_0 / \partial t$ . This term partially couples the two equations however it mostly acts as a driving term for temporal density variations. This energy can be dissipated via diffusion terms but due to their small contributions over the spatial and time scales of interest, they are neglected here but are included in the simulation for numerical stability. The coupling of interest here is  $\alpha(\varphi_1 - n_1)$  which fully couples the two equations. The constant,  $\alpha$  includes the parallel resistive dynamics due to ion-electron collisions and is defined as  $\alpha = T_e k_z^2 / (n_0 e^2 \eta \omega_c i)$ , where  $\eta$  is the electron resistivity. The Poisson brackets are defined as:

$$\{\varphi, f\} = (\partial \varphi / \partial x)(\partial f / \partial y) - (\partial f / \partial x)(\partial \varphi / \partial y). \quad (2.3)$$

For linearisation, a radially varying background electrostatic potential ( $\varphi_0(x)$ ) is included, this will act as the zonal flow profile. With  $\varphi = \varphi_0 + \varphi_1 = \varphi_0(x) + \hat{\varphi} \exp(i(k_y y - \omega t))$  and  $n = n_1 = \hat{n} \exp(i(k_y y - \omega t))$ . In this context,  $\phi_0$  is associated with the background flow and  $\phi_1$  &  $n_1$  are the representations of drift-wave perturbations in the form of plane waves in the poloidal direction. Furthermore  $V = \partial \varphi_0 / \partial x$  is the velocity profile of the background flow. Firstly, the new definition of  $\zeta$  such that it's conducive to linearising



Eq. (2.1):

$$\begin{aligned}\zeta &= \frac{dV}{dx} + \frac{\partial^2 \varphi_1}{\partial x^2} - k_y^2 \varphi_1 = \zeta_0 + \zeta_1 \\ \zeta_0 &= \frac{dV}{dx} \quad \zeta_1 = \frac{d^2 \varphi_1}{dx^2} - k_y^2 \varphi_1\end{aligned}$$

Substituting this description into Eq. (2.1) and rearranging leads to:

$$-i\omega\zeta_1 + ik_y V \zeta_1 - ik_y \frac{d^2 V}{dx^2} \varphi_1 = \alpha(\varphi_1 - n_1) \quad (2.4)$$

This can be substituted into Eq. (2.2) as well as the definition for  $n_1$ . Re-labelling  $\hat{\varphi} \exp(i(k_y y - \omega t))$  as  $\varphi_1$ , leads to:

$$-i\omega n_1 + ik_y V n_1 = \alpha(\varphi_1 - n_1) - ik_y \kappa \varphi_1 \quad (2.5)$$

rearranging Eq. (2.5) yields:

$$n_1 = \frac{i\alpha + k_y \kappa}{\omega - k_y V + i\alpha} \varphi_1, \quad (2.6)$$

this can now be substituted into Eq. (2.4) to eliminate  $n_1$  and produce:

$$\left[ \frac{d^2}{dx^2} - k_y^2 + \frac{k_y}{\omega - k_y V} \frac{\partial^2 V}{\partial x^2} - \frac{i\alpha}{\omega - k_y V + i\alpha} \left( 1 - \frac{\kappa k_y}{\omega - k_y V} \right) \right] \varphi_1 = 0 \quad (2.7)$$

Up to this point the derivation is fairly similar to the derivation in Numata et al. [28] (near the end of section IV. Stability of Zonal Flow). From here a different approach is taken to derive a global dispersion relation.

Firstly a definition of the zonal flow velocity profile is needed, the particular profile chosen is,  $V(x) = V_0 \sin(k_{ZF} x)$ . A unique property of this profile is that:

$$\frac{d^2 V(x)}{dx^2} = -V_0 k_{ZF}^2 \sin(k_{ZF} x) = -k_{ZF}^2 V(x)$$

Additionally, with an appropriately chosen  $k_{ZF}$ , multiple zonal flows can be fit into a slab of arbitrary width  $L$  (provided the length-scale satisfies the applicability of the MHW

model). Substituting this profile into Eq. (2.7) gives:

$$\left[ \frac{d^2}{dx^2} - k_y^2 + \frac{-k_y V_0 k_{ZF}^2 \sin(k_{ZF} x)}{\omega - k_y V_0 \sin(k_{ZF} x)} - \frac{i\alpha}{\omega - k_y V_0 \sin(k_{ZF} x) + i\alpha} \left( 1 - \frac{\kappa k_y}{\omega - k_y V_0 \sin(k_{ZF} x)} \right) \right] \varphi_1 = 0 \quad (2.8)$$

From here there are multiple avenues to explore, Numata et al. for example explores the extremal limits of  $\alpha$ . Setting  $\alpha = 0$  reduces Eq. (2.8) to a form similar to Rayleigh's equation for a neutral fluid. This exposes an important feature in this dispersion relation as a result of Rayleigh's inflection point theorem. This requires that for the growth rate of the drift-wave perturbation to be finite that  $d^2 V/dx^2(x_i) = 0$  at  $x = x_i$  —for this profile,  $-k_{ZF}^2 V(x_i) = 0$ . Equivalently setting  $\alpha = \infty$  gives a requirement of  $-k_{ZF}^2 V(x_i) + \kappa = 0$ . The corresponding method of obtaining a dispersion relation for these limits is to multiply Eq. (2.8) by the complex conjugate of the potential,  $\varphi_1^*$  and integrating over the whole volume. This is unsuitable for our case since if  $\alpha$  is finite, then it introduces new resonance conditions that cannot be handled by this approach.

### 2.2.2 Global Dispersion Relation

Instead of the approach in Numata et al. a different route is explored, looking at the implications of intermediate values of  $\alpha$  where Eq. (2.8) cannot be simplified and many resonances exist. Given the periodicity of the velocity profile in the radial direction and the  $k_x = 0$  definition of the chosen drift-wave perturbation, a limited spatial average in the radial direction should be sufficient to capture the effects of the velocity profile. The extent of the region chosen is between  $x - l$  and  $x + l$ , where  $l = n\pi/k_{ZF}$  where  $n \in \mathbb{Z}$  and  $n \gg 1$ . Therefore the total extent is always more than  $2\pi/k_{ZF}$  which consists of a full radial period of the velocity profile (where it ranges from  $-V_0$  and  $V_0$ ). The general expression describing the spatial average of an arbitrary function is :

$$\langle f \rangle = \frac{1}{2l} \int_{x-l}^{x+l} f(v(\xi)) d\xi = \frac{1}{2l} \int_{x-l}^{x+l} \left[ \int_{-\infty}^{\infty} f(\chi) \delta(\chi - v(\xi)) d\chi \right] d\xi \quad (2.9)$$

Here  $\xi$  is the dummy variable for the real-space coordinate and  $\chi$  is the dummy variable for the velocity-space coordinate. The averaged function,  $f$  is any function/expression that is dependent on the velocity profile  $v(\xi) = \chi$ . Changing the order of integration and

defining a new function  $F_0(\chi)$  gives:

$$\langle f \rangle = \int_{-\infty}^{\infty} f(\chi) \left[ \frac{1}{2l} \int_{x-l}^{x+l} \delta(\chi - v(\xi)) d\xi \right] d\chi \quad (2.10)$$

$$F_0(\chi) = \frac{1}{2l} \int_{x-l}^{x+l} \delta(\chi - v(\xi)) d\xi = \frac{1}{2l} \sum_{|\xi-x|<l} \left| \frac{d\chi}{d\xi} \right|_{\chi=v(\xi)}^{-1} \quad (2.11)$$

$$\langle f \rangle = \int_{-\infty}^{\infty} f(\chi) F_0(\chi) d\chi \quad (2.12)$$

Converting Eq. (2.11) to be an integral over velocity( $\chi$ )-space:

$$F_0(\chi) = \frac{1}{2l} \int_{-\infty}^{\infty} \delta(\chi - v(\xi)) \left| \frac{d\chi}{d\xi} \right|^{-1} d\xi \quad (2.13)$$

Normally the evaluation of Eq. (2.11) in real-space leads to a sum of the inverted derivatives of  $\chi$  at the different locations in real-space where the  $\delta$ -function is satisfied. However given that the chosen velocity profile varies between  $-V_0$  and  $V_0$ , switching to velocity-space gives only one possible location where the resonant conditions being considered are satisfied and therefore giving a tractable result. In addition to the limited variability and periodicity of the chosen velocity profile there is also the unique property that its spatial derivative can be defined as a function of itself. If for now the constant  $V_0$  is neglected in this example (since it can always be transferred outside integrals) and  $v(\xi) = \sin(k_{ZF}\xi)$  then:

$$\left| \frac{d\chi}{d\xi} \right|^{-1} = \frac{1}{k_{ZF}} \frac{1}{\cos(k_{ZF}\xi)} = \frac{1}{k_{ZF}} \frac{1}{\sqrt{1 - \sin^2(k_{ZF}\xi)}} = \frac{1}{k_{ZF}} \frac{1}{\sqrt{1 - \chi^2}} \quad (2.14)$$

Now evaluating Eq. (2.13) results in (note the reference to  $\chi$  on the RHS is allowed due to the  $\delta$ -function fixing the definition  $\chi = v(\xi)$ ):

$$F_0(\chi) = \frac{1}{2lk_{ZF}} \frac{1}{\sqrt{1 - \chi^2}} \quad (2.15)$$

This expression is immensely useful for simplifying (relatively) the procedure for applying the spatial averaging to Eq. (2.8). To illustrate the general procedure, an example of the averaging technique applied to a term in Eq. (2.8) is presented.

$$T = \left\langle \frac{-k_{ZF}^2 k_y V_0 \sin(k_{ZF}x)}{\omega - k_y V_0 \sin(k_{ZF}x)} \right\rangle = \frac{-k_{ZF}^2}{2l} \int_{x-l}^{x+l} \frac{\sin(k_{ZF}\xi)}{\omega^* - \sin(k_{ZF}\xi)} d\xi, \quad (2.16)$$

where  $\omega^* = \omega/(k_y V_0)$ . Changing to velocity-space gives:

$$T = -k_{ZF}^2 \int_{\chi(x-l)}^{\chi(x+l)} \frac{\chi F_0(\chi)}{\omega^* - \chi} d\chi = k_{ZF}^2 \int_{\chi(x-l)}^{\chi(x+l)} \frac{g(\chi)}{\chi - \omega^*} d\chi \quad (2.17)$$

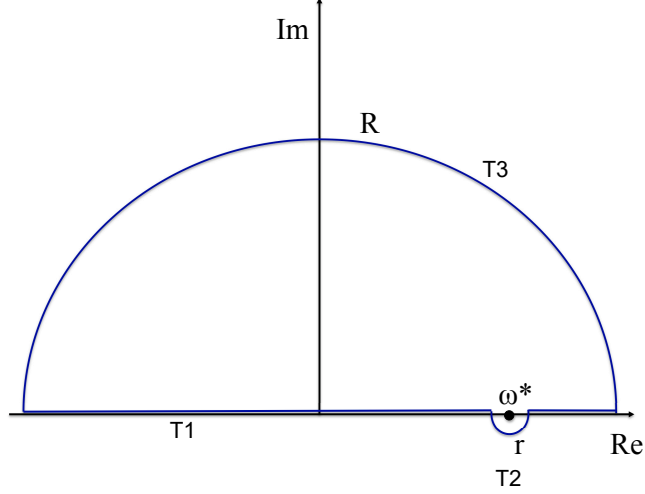


Figure 2.1: Example of integration contour used in the averaging technique, labels for the terms in Eq. (2.18) are also included.

The denominator in the integral requires careful treatment as different limits give distinct results. Therefore the term is split into three parts:

$$T = T_1 + T_2 + T_3 = k_{ZF}^2 \int_{\chi(x-l)}^{\chi(x+l)} \frac{g(\chi)}{\chi - \omega^*} d\chi + k_{ZF}^2 \int_r \frac{g(\chi)}{\chi - \omega^*} d\chi + k_{ZF}^2 \int_R \frac{g(\chi)}{\chi - \omega^*} d\chi \quad (2.18)$$

In this case,  $T_1$  deals with the non-resonant case where  $\omega^*$  is far from  $\chi$ ,  $T_2$  looks at the resonant case and  $T_3$  completes the contour illustrated in Fig. 2.1. Starting with the evaluation of  $T_1$ , changing to real-space and rearranging:

$$T_1 = \frac{-k_{ZF}^2}{2l\omega^*} \int_{x-l}^{x+l} \frac{\chi}{1 - \chi/\omega^*} d\xi \quad (2.19)$$

$$T_1 = \frac{-k_{ZF}^2}{2l\omega^*} \int_{x-l}^{x+l} \chi \left( 1 + \left( \frac{\chi}{\omega^*} \right) + \left( \frac{\chi}{\omega^*} \right)^2 + \dots \right) d\xi \quad (2.20)$$

Note that with  $(\chi/\omega^*)$  taken as a small parameter a Maclaurin expansion is used.

Absorbing the extra  $\chi$  in the integral into the expansion and keeping only terms the first term that will yield a non-zero result gives:

$$T_1 = \frac{-k_{ZF}^2}{2l\omega^*} \int_{x-l}^{x+l} \left( \frac{\chi^2}{\omega^*} \right) d\xi = \frac{-k_{ZF}^2}{2l\omega^{*2}} \int_{x-l}^{x+l} \chi^2 d\xi \quad (2.21)$$

$$T_1 = \frac{-k_{ZF}^2}{2l\omega^{*2}} \int_{x-l}^{x+l} \sin^2(k_{ZF}\xi) d\xi = \frac{-k_{ZF}^2}{2l\omega^{*2}} \left[ \frac{\xi}{2} - \frac{\sin(2k_{ZF}\xi)}{4k_{ZF}} \right]_{x-l}^{x+l} \quad (2.22)$$

$$T_1 = \frac{-k_{ZF}^2}{2\omega^{*2}} \quad (2.23)$$

Evaluating the remaining pieces of the contour integrals  $T_2, T_3$  gives:

$$T_2 = k_{ZF}^2 \int_r \frac{g(\chi)}{\chi - \omega^*} d\chi = i\pi k_{ZF}^2 g(\omega^*) = i\pi k_{ZF}^2 \omega^* F_0(\omega^*) \quad (2.24)$$

$$T_3 = k_{ZF}^2 \int_R \frac{g(\chi)}{\chi - \omega^*} d\chi = \frac{i\pi k_{ZF}}{2l} \quad (2.25)$$

Even when the resonant condition isn't met there are still poles at  $\chi = -1$  and  $\chi = 1$  and the possibility of needing to use branch cuts was considered but the residue at these poles evaluates to 0 so any contribution is not included. Combining all of the parts:

$$T = T_1 + T_2 + T_3 = \frac{-k_{ZF}^2}{2\omega^{*2}} + \frac{i\pi k_{ZF}}{2l} + i\pi k_{ZF}^2 \omega^* F_0(\omega^*) \quad (2.26)$$

This averaging technique is applied to every term in Eq. (2.8) and the resulting dispersion relation is:

$$\begin{aligned} & \left[ -k_x^2 - k_y^2 + i \frac{k_{ZF}\pi}{2l} - \frac{k_{ZF}^2}{2\omega^{*2}} + k_{ZF}^2 \omega^* \pi i F_0(\omega^*) \right. \\ & - \frac{\gamma}{\omega^* + \gamma} - \frac{\gamma}{2(\omega^* + \gamma)^3} + \pi i \gamma F_0(\omega^* + \gamma) \\ & + \frac{\gamma^*}{\omega^*} + \frac{\gamma^*}{2\omega^{*3}} - \pi i \gamma^* F_0(\omega^*) \\ & \left. - \frac{\gamma^*}{\omega^* + \gamma} - \frac{\gamma^*}{2(\omega^* + \gamma)^3} + \pi i \gamma^* F_0(\omega^* + \gamma) \right] \varphi_1 = 0. \end{aligned} \quad (2.27)$$

There are a few convenient labels introduced,  $\gamma = i\alpha/k_y V_0$  and  $\gamma^* = \kappa/V_0$ . Now the x-dependence is gone but a contribution from the ZF velocity profile and its characteristic inverse length-scale,  $k_{ZF}$ , is retained. Second order terms in  $V_0$  are included as they can contribute at sensible values of  $\alpha, \kappa$  and with  $V_0 \gg 0$ . The averaging window,  $l$ , is also present in the result and terms associated with it may have their contribution reduced if  $l$  is increased to large values. But given that  $F_0$  spans the entire range of values of velocity inside the  $\{(x-l), (x+l)\}$  interval, the averaging in the velocity-space

and real-space should be consistent with each other and should be independent of  $l$ . Note also that in averaging Eq. (2.8), the second derivative with respect to  $x$  has been replaced with  $-k_x^2$ . This radial wavenumber,  $k_x$ , is assumed to be small with  $k_x \ll k_y$  and  $k_x \ll k_{ZF}$ . The motivation for this choice comes from the linear drift-wave solution to the Hasegawa-Wakatani equations which yield a stable propagating drift-wave at  $k_x = 0$  and finite  $k_y$  if zonal flow contributions are excluded. A similar justification is used when looking at vertically stratified ocean waves with a rigid cap condition [36], where provided the length scale of the  $x$  direction is much greater than the length scale associated with the zonal-flow-drift-wave interaction dynamics then  $-k_x^2$  is the result of evaluating the  $d^2/dx^2$  term in Eq. (2.8) with  $k_x \ll 1$ .

There are some limitations to consider for this method. Mostly these concern the velocity profile of the background flow. A velocity profile that is either not periodic or has no clear value for the characteristic length scale for variation,  $l$ , will not be well suited for this method. Similarly any velocity profile whose formulation's derivative cannot be expressed as a function of the formulation itself, is again not well suited.

The complex contour derived terms should dominate for resonant conditions, where the drift-wave phase speed matches the given condition. Solving Eq. (2.27) is a non-trivial task and cannot easily be done via straight-forward analysis. A more fruitful approach is to solve the equation numerical via any number of root-finding algorithms that are widely available. Here, it is solved using the `fsolve(...)` function in MATLAB. Before using said function it is useful to rearrange Eq. (2.27) to eliminate any possible divergences. Fig. 2.2a the result of solving Eq. (2.27), in particular the growth rates with respect to the mode number of the perturbations,  $m_s$ . This mode number is defined as:  $m_s = k_y L / 2\pi$  where  $L$  is the slab length. Fig. 2.2b shows an exploration of the  $\alpha - \kappa$  space for the maximum growth-rate. It is evident that  $\kappa$  is a dominant drive of drift-wave instability, which is consistent with the additional energy that is introduced by the term containing  $\kappa$  in the MHW model.

### 2.2.3 Numerical Analysis

To verify the newly obtained dispersion relation, data from a numerical simulation is used. The simulation solves the MHW model in 2D slab geometry with doubly-periodic boundary conditions. The slab lengths are normalized to the hybrid Larmor radius,  $L_x = L_y = L = 40\rho_s$  and the time-steps are  $\Delta t = 0.01\omega_{ci}^{-1}$ , with  $\omega_{ci} = eB/m_i$ . Arakawa's method [37] is used to solve the Poisson brackets and a third-order Karniadakis implementation [38] is used for the time evolution. The dissipative terms, such as  $D\nabla^4 n$ , are

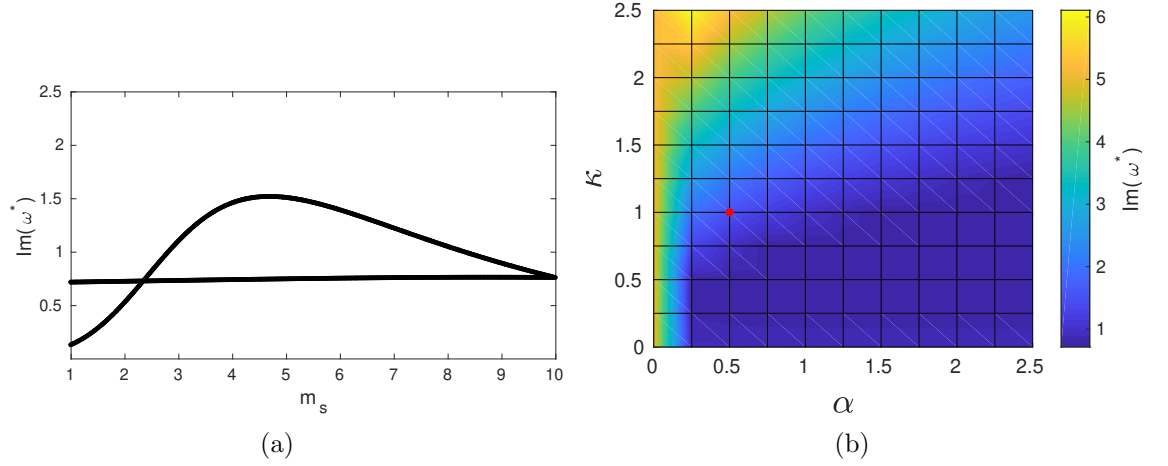


Figure 2.2: 2.2a The growth rate(imaginary component of  $\omega$ ) versus the perturbation mode number. The parameters are:  $\alpha = 0.5$ ,  $\kappa = 1.0$  and  $k_{ZF} = 0.4\pi$  and  $V_0 = 0.1$ . 2.2b A scan across  $\alpha - \kappa$  space with the z-axis showing the maximum growth rate. The red dot shows the  $\alpha = 0.5$  and  $\kappa = 1.0$  location.

added back in to aid numerical stability, and are defined as  $D = 10^{-4}$ .

The initial conditions are chosen to specifically look for drift-wave and zonal flow interactions, to that end the plasma number density is set as  $n(x, y, 0) = 0.01 \cos(k_x x + k_y y)$ , and  $k_x = 0.01 k_y$ . The simulation tracks the electrostatic potential but solves the MHW model which describes the time-evolution of the vorticity  $\nabla^2 \varphi$ . Therefore an initial condition for the vorticity needs to be defined, but derived from the initial condition for  $\varphi$ :

$$\zeta(x, y, 0) = k_{ZF} V_0 \cos(k_{ZF} x) - (k_x^2 + k_y^2)(0.01 V_0) \cos(k_x x + k_y y) \quad (2.28)$$

The  $V_0$  constant comes from the inclusion of a background flow in the initial condition of  $\varphi$ . The  $(0.01 V_0)$  term comes from the perturbed potential  $\varphi_1$  having an amplitude 0.01 times smaller than the amplitude of  $\varphi_0$ . In addition to the number density,  $n$  and the electrostatic potential,  $\varphi$ , various energies are tracked:

$$E_{ZF} = \frac{1}{2} \int (\nabla \langle \varphi \rangle)^2 dV \quad (2.29)$$

$$E_T = \frac{1}{2} \int (\nabla(\varphi - \langle \varphi \rangle))^2 dV \quad (2.30)$$

$$E_{Kin} = E_{ZF} + E_T \quad (2.31)$$

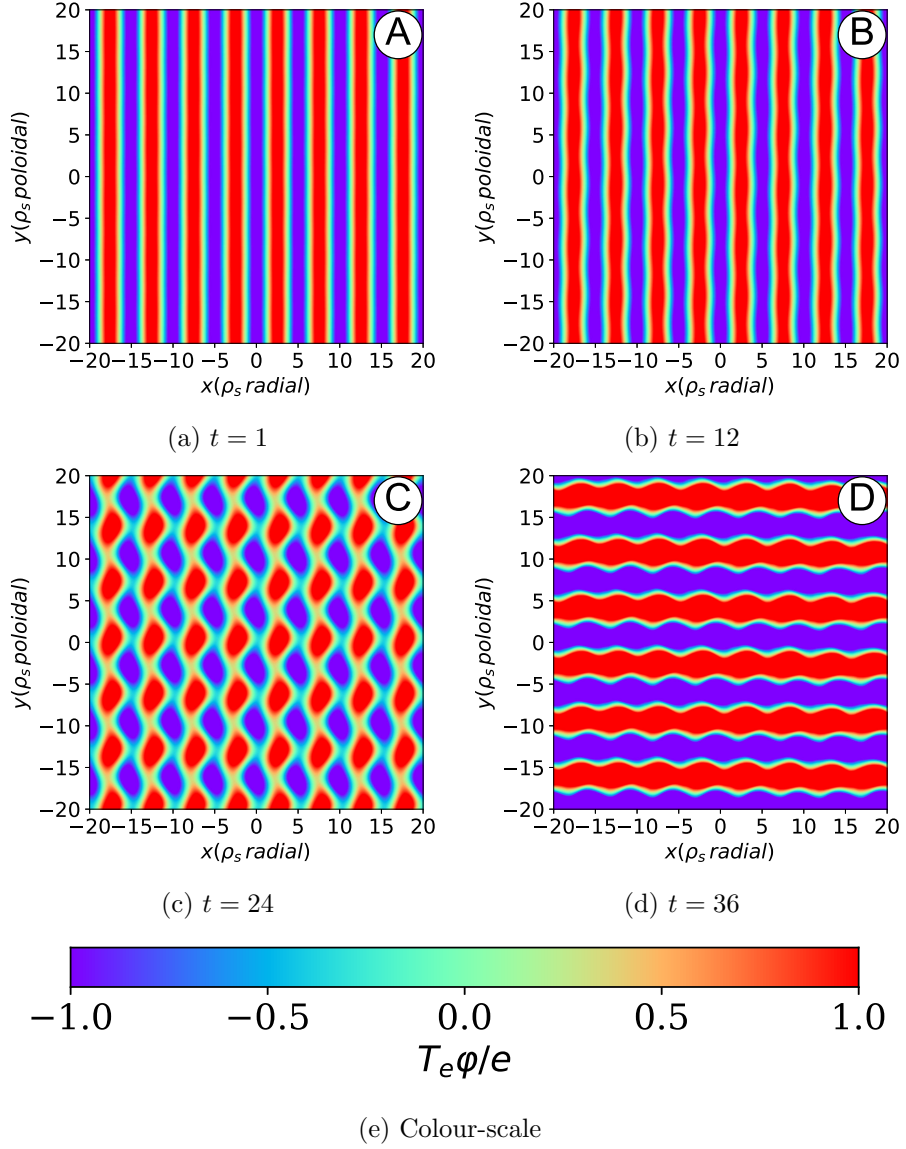


Figure 2.3: Plots showing the time-evolution of scalar potential. The time-steps are in units of  $\omega_{ci}^{-1}$ . The initial perturbation's  $k_y$  is set to  $0.3\pi$ , or a mode number  $m_s = 6$ .

The energies are split into zonal flow energy,  $E_{ZF}$ , the energy of the turbulence,  $E_T$  and the kinetic energy,  $E_{Kin}$ . Figure 2.3 illustrates the result of a simulation run. The parameters are set as  $\alpha = 0.5$ ,  $\kappa = 1.0$ ,  $k_{ZF} = 0.4\pi$  and  $V_0 = 1$ . The initial drift-wave perturbation is not clearly visible in Fig. 2.3a but it is of the form visible in Fig. 2.3d ( $m_s = 6$  corresponding to 6 peaks). The perturbation grows rapidly and is clearly dominant by the end of the time-span. Figure 2.4 shows this transition in the context of



system energetics.

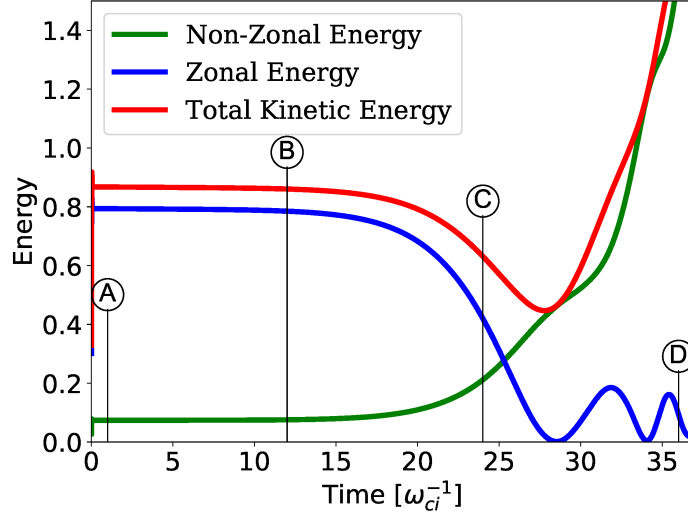


Figure 2.4: An energy plot of the simulation run shown in Fig. 2.3. The A-D labelled points show the energies at various stages and the transition from zonal flow to drift-wave dominance is clear. The energies are normalised to the same constant, which is chosen for convenience.

## 2.3 Discussion

To start with, the results of the simulation are compared to the prediction from the solution to Eq. (2.27). Figures 2.3 and 2.4 show the initial phases of a simulation run with parameters set to values typical of those seen in tokamak plasmas. Fig. 2.4 in particular shows evidence of zonal flow - drift-wave interaction in the fact that it shows a decay of zonal flow energy on the same time-scale as the growth of the drift-wave energy. This excludes the possibility that the drift-wave growth is due to pure linear instability as in that case the zonal flow energy would have remained stable during drift-wave energy growth.

Figure 2.5 shows the frequencies and growth rates of the drift-waves, these are plotted for the cases of linear drift-wave instability, zonal flow-drift wave interaction and the measured results from the simulation. Figures 2.5a and 2.5b shows the case where conditions are far from resonance. As  $V_0$  (the zonal flow velocity profile amplitude) increases, there is a gradual departure for large mode numbers,  $m_s$ , this can be seen in Figs. 2.5c and 2.5d.

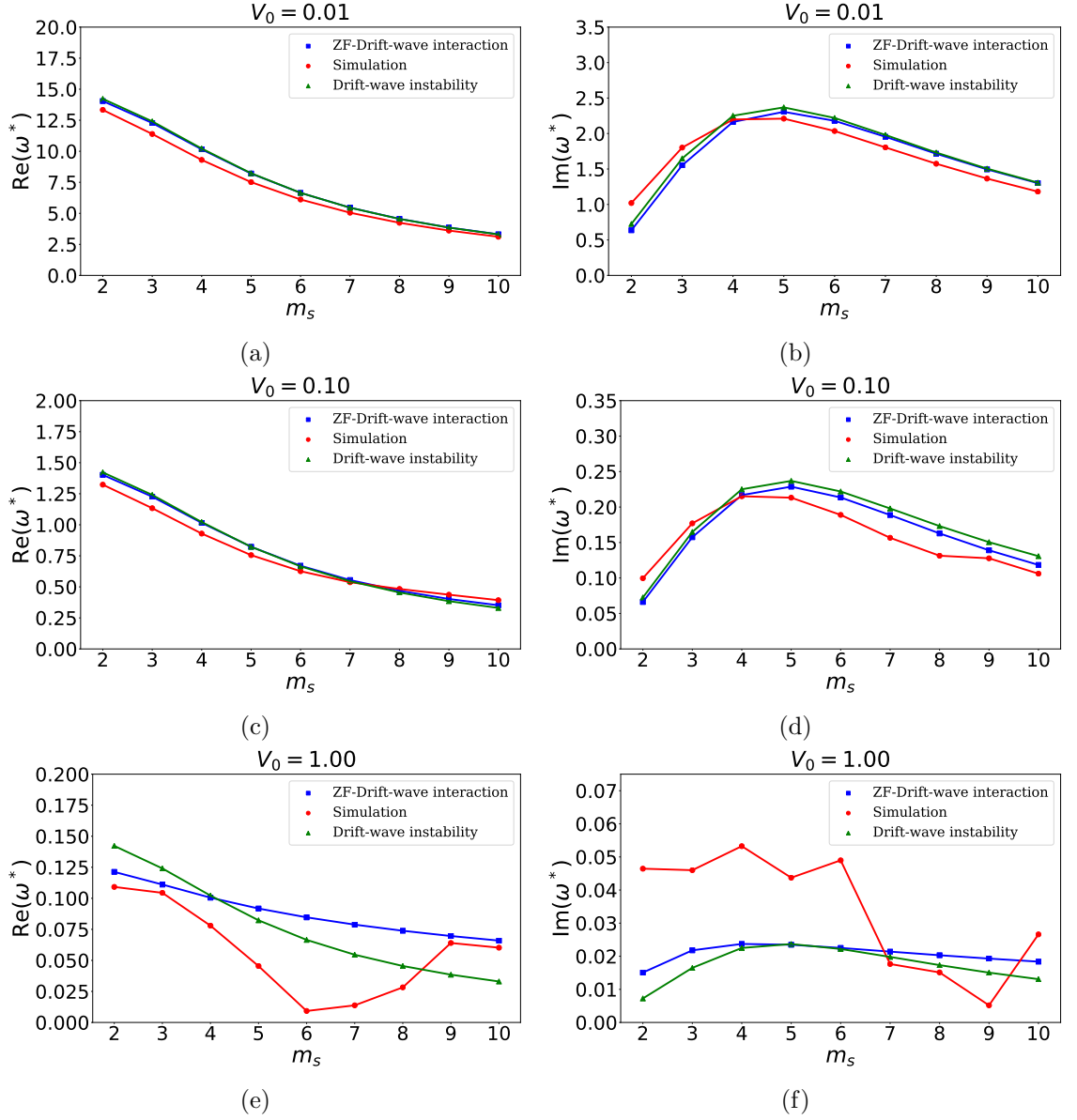


Figure 2.5: Figures showing the frequencies and growth rates of the drift-waves against their mode number,  $m_s$  at different values of  $V_0$  with identical conditions to Fig. 2.4. The curves correspond to predictions from the linear stability theory, the solution to Eq. (2.27) and the measure values from the simulation. The y-axis units are  $\omega^* = \omega/k_y V_0$ , these apply to the linear result as well to allow comparison between results.

When  $V_0$  is large enough such that  $-V_0/V_0$  range includes the drift-wave phase velocity, then contributions from resonant terms in Eq. (2.27) start to impact the dispersion relation, as can be seen in Figs. 2.5e and 2.5f. The zonal flow-drift wave interaction

deviates considerably from the linear instability case. At points the frequency and growth rates can differ by a factor 2-4. The departure of the simulation case from the predicted cases may be due to the resonant energy transfer from ZF to drift-wave happening very quickly and nonlinear interactions taking over almost immediately. The fact that the results show deviations from linear instability in resonant conditions demonstrates the sensitivity of the drift-wave growth to non-adiabatic electron response. This  $\alpha$  contribution is included in the Landau-like terms in Eq. (2.27). These are not the only Landau-like terms in the equation however, therefore there is no sole resonance that affects the drift-wave growth.

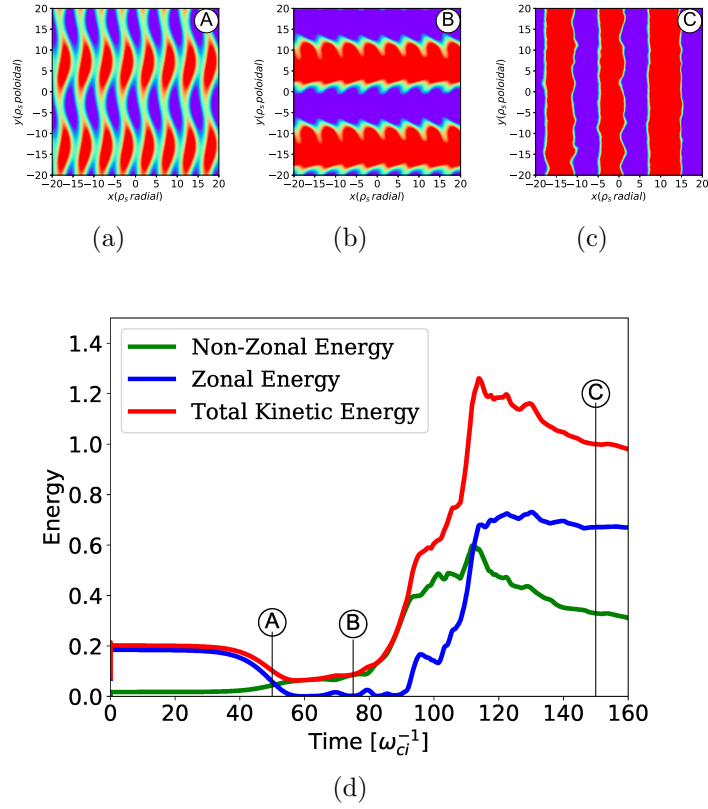


Figure 2.6: The main plot shows the energy of the system with constants set to  $\alpha = 0.5$ ,  $\kappa = 1.0$ ,  $V_0 = 1.0$ ,  $k_{ZF} = 0.4\pi$  and with a drift-wave perturbation mode number  $m_s = 2$ . Panel A shows the initial transition and inversion of dominant states, Panel B shows full dominance of the drift-wave mode and suppression of the zonal flow, with Panel C showing the return to zonal flow dominance.

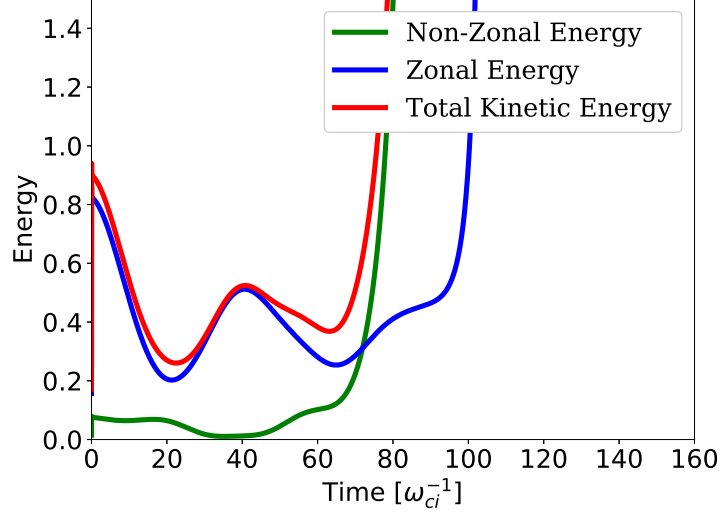


Figure 2.7: An energy plot showing the results from a simulation run similar to Fig. 2.6, but with  $V_0 = 0.01$  to illustrate a lack of zonal flow suppression as a result of energy exchange.

The energy dynamics of drift-waves and zonal flows are now examined closely over the course of the simulation, two cases which satisfy resonant conditions are investigated. Firstly, a case where  $\alpha = 0.5$  and  $m_s = 2$  are chosen with other parameters identical to the previous simulation run showcased in Figs. 2.3 and 2.4. The drift-wave perturbation mode number,  $m_s = 2$ , is chosen to showcase a simple example of drift-wave zonal flow interaction. The presentation is identical in format to Fig. 2.4 with the letter labels corresponding to accompanying snapshots in time. Prior to point A in Fig. 2.6 the zonal flow energy decays on approximately the same time scale as the drift-wave growth. By comparison, when this scenario is repeated away from resonance,  $V_0 = 0.01$ , the zonal flow does not decay at all and the drift-wave grows in a linear fashion. Therefore, further evidence that non-adiabatic electron response is contributing to zonal flow and drift-wave energy exchange at resonance. Also of note is that by point C the zonal flow dominates again, this is expected as that is the natural tendency of the MHW system. Figure 2.8 illustrates a similar scenario but with  $\alpha = 0.2$ , here the drift-wave grows faster than Fig. 2.6. This broadly agrees with Fig. 2.2b which shows that for the same  $m_s$ , the growth rate increases as  $\alpha$  is decreased (in this case from 0.5 to 0.2).

The topic of zonal flow decay is now investigated, even though the main concern of this chapter is to explore drift-wave instability, it is still useful to check the behaviour of

zonal flow decay. This is to verify that the behaviour is consistent with the behaviour seen for drift-wave growth and if so this provides further evidence to suggest an energy exchange between the two phenomena. The measure of the decay rates of zonal flows is  $1.0/\tau$ , here  $\tau$  is the time taken for the zonal flow energy to decay (to the first minimum). The data for the drift-wave growth from the simulation in Fig. 2.5f and the decay of the zonal flow energy in Fig. 2.9 are in good agreement both in terms of peak locations and overall structure. If the initial perturbation mode number is set  $m_s > 6$  then the energy exchange and so the zonal flow decay is muted and the decay does not occur until nonlinear interactions of the drift-waves generate modes with mode numbers of  $m_s = 4 - 6$ . Depending on the initial conditions, particularly the value  $\kappa$  which introduces energy into the system via a radial density gradient, this generation of optimal drift-waves can take a significant amount of time.

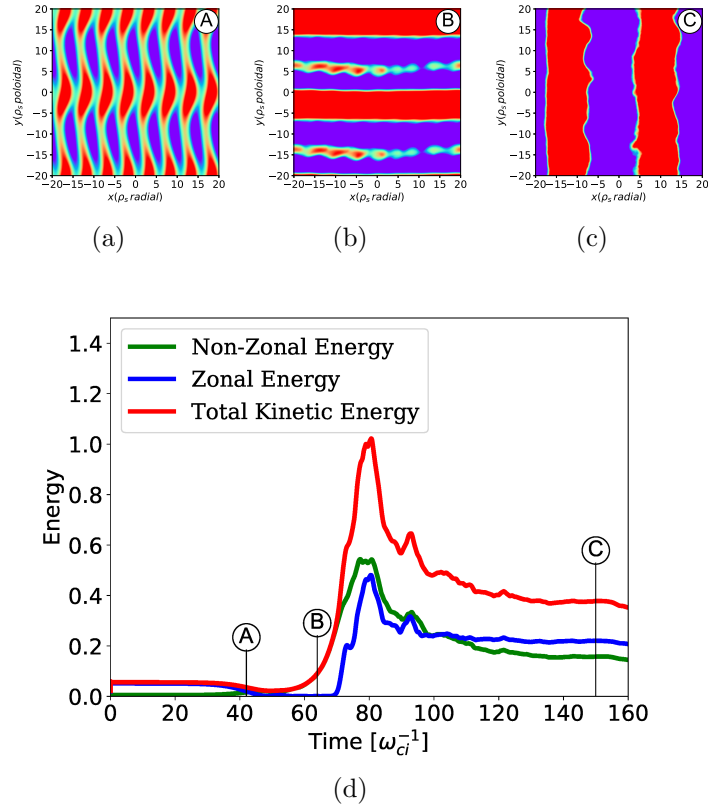


Figure 2.8: A similar figure to Fig. 2.6 but with  $\alpha = 0.2$ . This shows faster dynamics in all respects including drift-wave growth and subsequent zonal flow dominance later in the simulation.

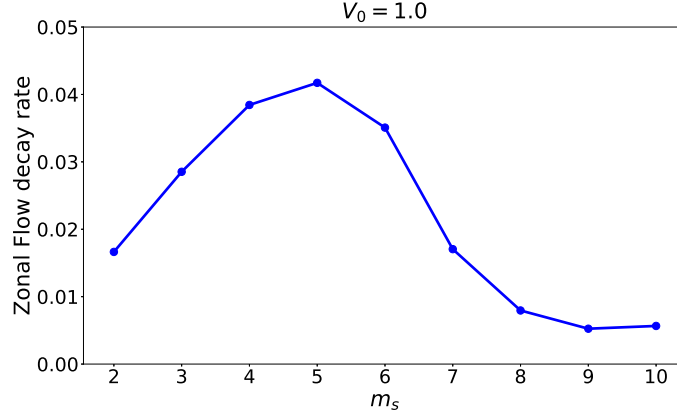


Figure 2.9: Figure showing the zonal flow decay rates with  $\alpha = 0.5$  consistent with all simulation data from Figures 2.6 and earlier.

### 2.3.1 Further analysis at $V_0 = 1.0$

Due to the fast evolution of mode structures in the case of running the simulation with  $V_0 = 1.0$ , obtaining accurate data for the frequency and growth rate of the prescribed  $k_y$  modes is not straightforward. Instead more data is obtained by running the simulation for longer and starting with a perturbation with a significantly reduced amplitude. The perturbation amplitude is now set to  $10^{-12}$  instead of 0.01. This slows the dynamics of the system and allows the perturbations to stay in the linear regime for much longer. In turn, this allows for more confidence in any derived frequencies and growth rates of the perturbations. Furthermore the extraction of these frequencies and growth rates is now approached differently. Considering the phase  $q(t)$  of the perturbation, expressed as:

$$\varphi(t, y) = \exp(iq(t) + ik_y y) \quad (2.32)$$

Then looking at the ratio of  $\varphi(t + dt)$  and  $\varphi(t)$  and using a Maclaurin series, returns:

$$\frac{\varphi(t + dt)}{\varphi(t)} = \exp(iq(t + dt) - iq(t)) \sim 1 + idt \frac{dq}{dt} \quad (2.33)$$

Where through re-arrangement  $\omega$  can be obtained since  $\omega = dq/dt$  with frequency being the real part and growth rate being the imaginary part. The plots in Figure 2.10 are in the same format as Figs. 2.5e and 2.5f but with more accurate values for the frequencies and growth rates of the various modes from the simulation.

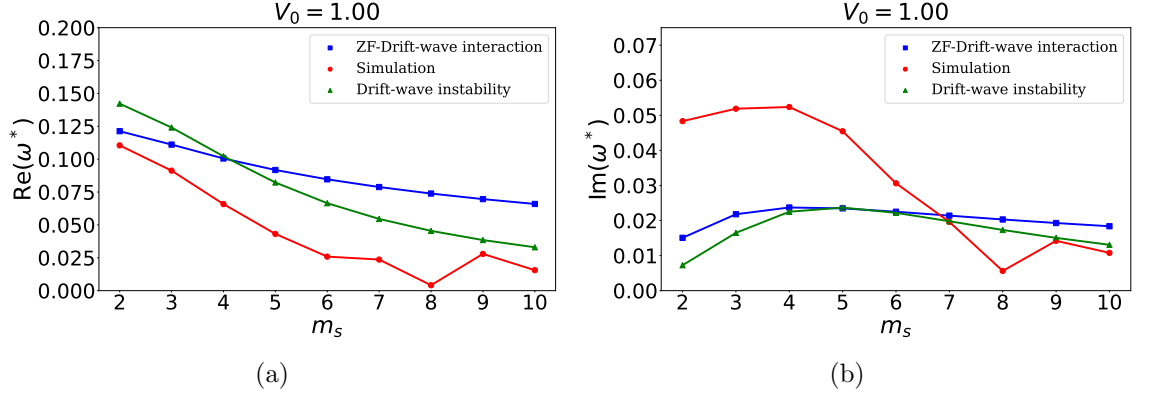


Figure 2.10: Figures showing the frequencies and growth rates of the drift-waves against their mode number,  $m_s$ .

To obtain more accurate values for the frequencies and growth rates, the simulation was run with a much smaller amplitude for the initial drift-wave-like perturbation, from  $10^{-2}$  to  $10^{-12}$ . In essence, this slows the dynamics of the drift-wave growth sufficiently that several oscillations of the mode can exist before the growth to the maximum amplitude (after which, as before, there is a decay and zonal flow becomes dominant again). For most mode numbers this works well and allows upwards of  $\sim 10$  coherent oscillations that exhibit linear growth. However, at mode numbers  $m_s > 6$ , there is a complication in the sense that those modes do not grow linearly or become the dominant mode. As mentioned before when discussing Fig. 2.9, there is still a zonal flow decay and re-emergence (albeit more slowly than with lower modes), but the dominant drift-wave mode is not the mode that is initiated at the start of the simulation but  $m_s = 4 - 6$ . The technique to obtain  $\omega$  from the change in phase,  $q$  described earlier is still applied to the data and still yields values that are less erratic than in Figs. 2.5e and 2.5f.

## 2.4 Conclusion

This chapter explored a possible mechanism of drift-wave and zonal flow interaction. A spatial averaging technique was used in calculating the drift-wave dispersion relation in order to account for a background velocity profile. This exposed a number of resonant terms which, when the relevant conditions were satisfied, modified the classic linear dispersion relation obtained from the MHW (Modified Hasegawa-Wakatani) model. The resulting equation was solved numerically and the results were compared to and verified with data from a simulation of MHW. Various distinct initial conditions were used to probe the nature of the drift-wave/zonal flow interaction and clear evidence was found

indicating energy exchange between the two phenomena in the initial phase of drift-wave growth. The prediction that the energy exchange would be dependent on the drift-wave mode number,  $m_s$ , was also verified. After analysis of more accurate data for the most resonant case ( $V_0 = 1.0$ ) it is clear that though, there is clear deviation of the frequencies and growth rates from the standard linear relation, there is also a deviation from the predicted rates obtained from utilizing spatial averaging. It seems there are more effects at play that are not accounted for by the spatial averaging approach. Nevertheless, the results from this chapter do provide information about one aspect of the potential drift-wave/GAM (Geodesic Acoustic Modes)/zonal flow interaction in a simplified model setting. The next chapter will investigate in more detail the properties of GAMs, primarily focusing on the linear properties in a different more holistic simulation which simulates an entire spherical tokamak (CENTORI).



## Chapter 3

# Linear GAM Properties

### 3.1 Introduction

One of the emerging areas of interest in plasma physics this century has been the Geodesic Acoustic Mode(GAM). This mode was hypothesised by Winsor in 1968[39], to explain certain observations in both tokamaks[40] and computer simulations. In particular an advantageous property of this mode is that it oscillates with an observable frequency, this can be used to infer the sound speed in the plasma and acts as a proxy for the electron and ion temperatures. A better understanding of the behaviour of GAMs both linearly and non-linearly could lead to a non-invasive method of detecting the electron and ion temperature in the plasma. Another benefit to understanding GAMs would be a possible use of its shear flow in controlling the level of edge turbulence. To start with an analytical description of the most basic version of GAM is presented following the derivation in Winsor's paper[39]. Following this a brief introduction to CENTORI is given along with an overview of the basic physics of the simulation. Finally results and subsequent analysis of a CENTORI run are presented and the linear properties of the signals produced are investigated. This chapter should serve as a stepping stone to Chapter 4 where the non-linear properties of GAMs are investigated more deeply.

### 3.2 Geodesic Acoustic Mode

The basic concept for GAMs is that if an initial density fluctuation were to excite an electric field perturbation in a tokamak, then this would cause a perpendicular plasma flow which would lead to a density accumulation. This accumulation would generate a current that would act to reverse the electric field perturbation, which would lead to

an overshoot and an identical density fluctuation occurring  $180^\circ$  away from the original fluctuation. This typically appears as an up-down asymmetry in density in tokamaks, for example over-dense plasma at  $\theta = 90^\circ$  and under-dense at  $\theta = 270^\circ$ . This is classified by the fundamental poloidal mode number  $m=1$ . Crucially this mode can only occur in any magnetic confinement device with geodesic curvature, ie. tokamaks or stellarators, and hence the “Geodesic” part of the name. The term “Acoustic” comes from the fact that the wave-speed of GAMs scales with the sound speed in the plasma (the sound speed in question would be  $c_s \sim \sqrt{T_e/m_i}$ ). Winsor starts with a perturbed standard MHD system whilst neglecting the time variation of the magnetic field,  $\vec{B}$ . All of the equilibrium and perturbed quantities are defined as,  $p$  is equilibrium pressure and  $p_1$  is the perturbed pressure.

$$\rho \frac{\partial \vec{v}_1}{\partial t} = \frac{1}{c}(\vec{J}_1 \times \vec{B}) - \vec{\nabla} \rho_1 \quad (3.1)$$

$$\frac{\partial \rho_1}{\partial t} + \vec{\nabla} \cdot (\rho \vec{v}_1) = 0 \quad (3.2)$$

$$\vec{\nabla} \phi_1 = \frac{1}{c}(\vec{v}_1 \times \vec{B}) \quad (3.3)$$

$$\vec{\nabla} \cdot \vec{J}_1 = 0 \quad (3.4)$$

$$\rho^{-\gamma} \frac{\partial p_1}{\partial t} - \gamma p \rho^{-\gamma-1} \frac{\partial \rho_1}{\partial t} + \vec{v}_1 \cdot \vec{\nabla} (p \rho^{-\gamma}) = 0 \quad (3.5)$$

$\psi$  labels the magnetic surfaces and is defined as:  $\vec{B} \cdot \vec{\nabla} \psi = 0$ . Additionally  $p = (n_e + n_i)k_B T = 2\rho k_B T/m_i$ , ( $m_i \gg m_e$ ) and  $\rho = \rho(\psi)$  and  $p = p(\psi)$ . The perturbation velocity is defined as:

$$\vec{v}_1 = \left( v_{1\psi} \frac{\vec{\nabla} \psi}{|\vec{\nabla} \psi|^2} + v_{1s} \frac{\vec{B} \times \vec{\nabla} \psi}{B^2} + v_{1b} \frac{\vec{B}}{B^2} \right) \exp(-i\omega t) \quad (3.6)$$

The definitions for the individual velocity components are recovered by taking different components of the model equations:

$$\vec{\nabla} \psi \text{ component of Eq. (A.3) gives: } v_{1s} = \frac{\vec{v}_1 \cdot (\vec{B} \times \vec{\nabla} \psi)}{|\vec{\nabla} \psi|^2} \quad (3.7)$$

$$(\vec{B} \times \vec{\nabla} \psi) \text{ component of Eq. (A.3) gives: } v_{1\psi} = 0 \quad (3.8)$$

Since  $p = p(\psi)$  and  $\rho = \rho(\psi)$  then Eq. (A.5) reduces down to  $p_1 = (\gamma p / \rho) \rho_1$ . The  $J_{1\psi}$  term can be obtained by taking the  $(\vec{B} \times \vec{\nabla} \psi)$  of Eq. (A.1). Using the divergence theorem on the volume integral of Eq. (A.4) to turn it into a surface integral; substituting in  $J_{1\psi}$

and rearranging gives:

$$v_{1s} = \frac{-i\gamma p}{\omega\rho^2} \int \frac{(\vec{B} \times \vec{\nabla}\psi) \cdot \vec{\nabla}\rho_1}{B^2} \mathcal{J}dS \Big/ \int \frac{|\vec{\nabla}\psi|^2}{B^2} \mathcal{J}dS \quad (3.9)$$

Here  $\int \mathcal{J}dS$  is the surface integral with  $\mathcal{J}$  being the Jacobian for a given coordinate system. Taking the  $\vec{B}$  component of Eq. (A.1) recovers:

$$v_{1b} = -\frac{i\gamma p}{\omega\rho^2} \vec{B} \cdot \vec{\nabla}\rho_1 \quad (3.10)$$

The new definition of  $\vec{v}_1$  is:

$$\begin{aligned} \vec{v}_1 = & \left[ \frac{-i\gamma p}{\omega\rho^2} \left[ \int \frac{(\vec{B} \times \vec{\nabla}\psi) \cdot \vec{\nabla}\rho_1}{B^2} \mathcal{J}dS \Big/ \int \frac{|\vec{\nabla}\psi|^2}{B^2} \mathcal{J}dS \right] \frac{\vec{B} \times \vec{\nabla}\psi}{B^2} \right. \\ & \left. + -\frac{i\gamma p}{\omega\rho^2} \vec{B} \cdot \vec{\nabla}\rho_1 \frac{\vec{B}}{B^2} \right] \exp(-i\omega t) \end{aligned} \quad (3.11)$$

Multiplying both sides by  $\rho$ ; substituting the new  $\rho\vec{v}_1$  into Eq. (A.2) and rearranging and integrating both sides with respect to time (between 0 and  $\infty$ ) yields:

$$\rho_1 = \frac{-\gamma p}{\omega^2 \rho} \vec{\nabla} \cdot \left[ \left[ \int \frac{(\vec{B} \times \vec{\nabla}\psi) \cdot \vec{\nabla}\rho_1}{B^2} \mathcal{J}dS \Big/ \int \frac{|\vec{\nabla}\psi|^2}{B^2} \mathcal{J}dS \right] \frac{\vec{B} \times \vec{\nabla}\psi}{B^2} + \vec{B} \cdot \vec{\nabla}\rho_1 \frac{\vec{B}}{B^2} \right] \quad (3.12)$$

Now multiplying both sides by  $\rho_1^* \mathcal{J}dS$  and integrating; using integration by parts on the L.H.S. and re-arranging yields:

$$\begin{aligned} \omega^2 \int |\rho_1|^2 \mathcal{J}dS = & \frac{\gamma p}{\rho} \left\{ \left[ \left| \int \rho_1 \frac{(\vec{B} \times \vec{\nabla}\psi) \cdot \vec{\nabla}(B^2)}{B^4} \mathcal{J}dS \right|^2 \Big/ \int \frac{|\vec{\nabla}\psi|^2}{B^2} \mathcal{J}dS \right] \right. \\ & \left. + \int \frac{|\vec{B} \cdot \vec{\nabla}\rho_1|^2}{B^2} \mathcal{J}dS \right\} \end{aligned} \quad (3.13)$$

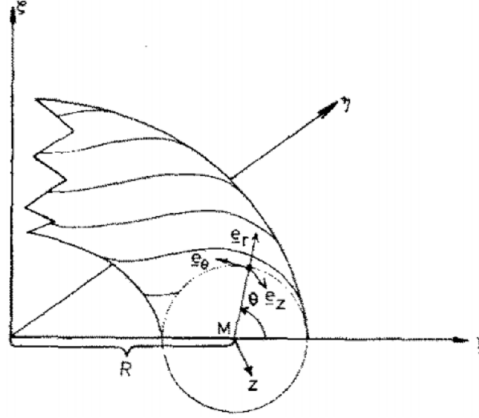


Figure 3.1: Knorr's model [6]

Up to this point the mathematical description of GAM has been in general magnetic coordinates. From this point forward the Knorr coordinate system is used. Now choosing Knorr's coordinate system as an example, it is possible to proceed in calculating the dispersion relation. Knorr's coordinate system is illustrated in Fig. 3.1, it consists of a radial, poloidal and toroidal directions to form an orthogonal system that describes a circular cross-section torus. For the surface integral the following definition for this coordinate system is used:

$$\mathcal{J}dS = r \left( 1 + \frac{r}{R} \cos \theta \right) d\theta dz \quad (3.14)$$

, where  $r$  is the radial direction along the minor radius,  $\theta$  is the poloidal angle,  $z$  is in the toroidal direction and  $R$  is the major radius. For modes independent of  $z$ , applying this coordinate system gives:

$$\omega^2 \int_0^{2\pi} |\rho_1|^2 d\theta = \frac{\gamma p}{\rho r^2 (1 + f^2)} \left[ 2r^2 \left| \int_0^{2\pi} \rho_1 \left( \sin(\theta) + \frac{r}{2R} \sin(2\theta) \right) d\theta \right|^2 / \pi R^2 \left( 1 + \frac{3r^2}{2R^2} \right) + f^2 \int_0^{2\pi} \left| \frac{\partial \rho_1}{\partial \theta} \right|^2 d\theta \right] \quad (3.15)$$

Now if  $\rho_1 \propto \sin \theta$  then:

$$\omega^2 = \frac{2\gamma p}{\rho R^2} \left( 1 + \frac{i^2}{8\pi^2} \right) = \omega_s^2 \left( 2 + \frac{1}{q^2} \right) \quad (3.16)$$

This describes the frequency of the GAM but the modal structure is fairly simple to describe. As described previously, the up-down asymmetry in the fluctuating electron density leads to an  $m = 1$  mode structure. This equation only holds for symmetric concentric circular plasmas with long radial wavelengths of the GAMs and no background flows in a single-fluid MHD description. Additionally, this is the accepted definition for GAM frequency in the absence of additional terms that can be introduced to include the effects of plasma rotation in the tokamak for example. A more detailed derivation of this result can be found in Appendix A.

### 3.3 CENTORI

In order to investigate the behaviour of GAMs(Geodesic Acoustic Mode) in MAST a simulation named CENTORI was primarily used. CENTORI(Culham Emulator of Numerical TORI[7]) is a two-fluid electromagnetic turbulence code that was developed in an effort to model, among other things, turbulent transport, resistive diffusion timescales and MHD instabilities. It does this by solving the two-fluid Braginskii[17] description of the plasma whilst co-evolving an equilibrium which is calculated using the modified Grad-Shafranov equation[41][42]. It is written in FORTRAN-95 and utilises MPI(Message Passing Interface) for parallelism. The coordinate system is slightly different to most used for fusion plasma analysis since the code is trying to capture full device geometry related effects. Therefore the coordinate system consists of  $R$  which is the major radius of the tokamak,  $Z$  which is the vertical displacement from a chosen central point and  $\zeta$  is the toroidal angle. The direction for the toroidal angle is chosen such that the  $(R, Z, \zeta)$  system generates a right-handed coordinate system. In addition, another more natural coordinate system is utilised. This would be the  $(\rho, \theta, \zeta)$  coordinate system, this is in general a non-orthogonal system. The plasma quantities are then evolved and tracked in both coordinate systems and the user can choose which one is more appropriate for their particular use-case. Here,  $\rho(R, Z)$  is a normalised version of the poloidal flux function ( $\psi$ ),  $\theta$  is the poloidal angle and  $\zeta$  is identical to before. The direction of travel along the poloidal and toroidal axes is again such that the coordinate system is right-handed. This coordinate system is illustrated in Fig. 3.2. The plasma quantities that are evolved are:  $n_i$ , ion number density;  $\vec{A}$ , vector potential;  $\vec{v}_i$ , the ion velocity;  $T_i$ , the ion temperature and  $T_e$ , the electron temperature. The electron number density  $n_e$  is also tracked via quasi-neutrality, which ties it to  $n_i$ . In addition there are more physical quantities which are evolved, however they are generally considered secondary. These secondary

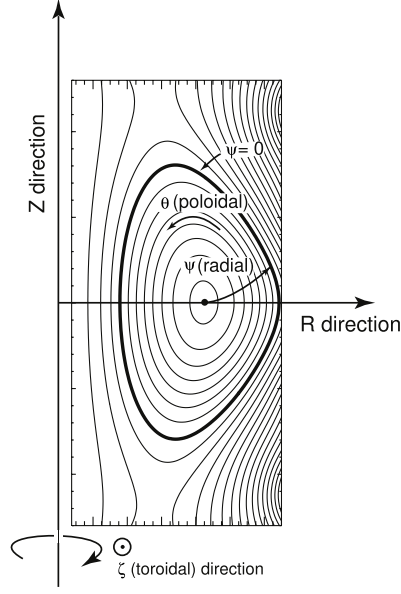


Figure 3.2: A breakdown of the coordinate systems used by CENTORI[7]

quantities are:  $p_i = n_e T_i$  and  $p_e = n_e T_e$ , ion and electron pressure respectively;  $\vec{J}$ , the current density;  $\vec{B}$ , the magnetic field;  $v_e$ , the electron velocity;  $\phi$ , the scalar potential;  $\vec{E}$ , the electric field. All of the tracked quantities are normalised before being used in any equations. The code favours using initial values as the basis for normalisation over equilibrium values. For example  $\vec{v}_i$  and  $\vec{v}_e$  are normalised using an initial Alfvén speed,  $v_a = \sqrt{B_0/4\pi m_i \bar{n}_e}$ , where  $B_0$  is the vacuum toroidal field on axis,  $\bar{n}_e$  is a volume averaged electron number density. The quantities are evolved using two-fluid equations. The ion momentum balance used is:

$$\rho_m \left( \frac{\partial \vec{v}_i}{\partial t} + \vec{W} \times \vec{v}_i \right) = -\nabla p_i - \frac{\rho_m}{2} \nabla \vec{v}_i^2 + en_e \vec{E} + \frac{en_e}{c} (\vec{v}_i \times \vec{B}) - en_e \eta \vec{J} - \rho_m \chi_v (\nabla \times \vec{W}) + \vec{S}_v \quad (3.17)$$

Here  $\rho_m = m_i n_e = \rho_i$  due to quasi-neutrality,  $\eta$  is resistivity,  $\vec{W} = \nabla \times \vec{v}_i$  is the vorticity,  $\chi_v$  is velocity diffusion,  $\vec{S}_v$  is external force. The electron momentum equation is modified in comparison to the ion momentum equation by ignoring inertial terms (effectively assuming zero electron mass):

$$\vec{0} = -\nabla p_e - en_e \vec{E} - \frac{en_e}{c} (\vec{v}_e \times \vec{B}) + en_e \eta \vec{J} \quad (3.18)$$

The energy evolution is defined as:

$$\frac{3}{2}n_i \left( \frac{\partial}{\partial t} + \vec{v}_i \cdot \nabla \right) T_i + p_i \nabla \cdot \vec{v}_i = -\nabla \cdot \vec{q}_i + S_i \quad (3.19)$$

$$\frac{3}{2}n_e \left( \frac{\partial}{\partial t} + \vec{v}_e \cdot \nabla \right) T_e + p_e \nabla \cdot \vec{v}_e = -\nabla \cdot \vec{q}_e + S_e \quad (3.20)$$

Again,  $q_i$  and  $q_e$  are the heat fluxes for the ions and electrons respectively and  $S_i$  and  $S_e$  are external heating sources for ions and electrons. The heat fluxes are derived from neoclassical thermal diffusivity terms ( $\chi_e$  and  $\chi_i$ ), which are themselves dependent on empirically derived neoclassical diffusivity coefficients ( $K_{NC,e}$  and  $K_{NC,i}$ ). These coefficients add the effects of toroidal curvature to the classical thermal diffusivity. There is also a contribution to the heat fluxes from terms associated with Rechester-Rosenbluth contribution [43], which damps radial fluctuations in electron temperature, the contribution is not included in the derivation of the ion heat fluxes. There is also a mass continuity equation which is only accounted for the ions owing to quasi-neutrality and the current being divergence free:

$$\frac{\partial \rho_i}{\partial t} + \nabla \cdot (\rho_i \vec{v}_i) = S_n - m_i \bar{n}_e v_A \nabla \cdot \Gamma_W^* + \delta_n - v_{i\parallel} (\rho_i - \langle \rho_i \rangle) \quad (3.21)$$

Here,  $S_n$  is external particle source;  $\delta_n$  is a diffusive term and  $\nabla \cdot \Gamma_W^*$  represents the effect of Ware Pinch. The Ware pinch is a phenomena which occurs in tokamak plasmas that are operated with a low safety factor,  $q < 3$ . It is a result of trapped particles in banana orbits that are affected by the toroidal electric field. This causes the orbit to be displaced from the mid-plane and combined with the  $\vec{\nabla} B$  and curvature drifts experienced by the trapped particles, causes the particles to drift radially inwards at a velocity of  $v_\rho = -E_\zeta / B_\theta$ . The flux therefore varies as,  $\Gamma \sim \epsilon^{0.5} n E_\zeta / B_\theta$  [44], where  $\epsilon = r/R$  is the inverse aspect ratio and  $\epsilon^{0.5}$  is the trapped particle fraction.

Finally there are Maxwell's equations, Faraday's Law, Gauss's Law of Magnetism and Ampere's Law:

$$\frac{1}{c} \frac{\partial \vec{A}}{\partial t} = -\vec{E} - \nabla \phi \quad (3.22)$$

$$\nabla \cdot \vec{B} = 0 \quad (3.23)$$

$$\vec{J} = \frac{c}{4\pi} \nabla \times \vec{B} \quad (3.24)$$

Gauss's Law is guaranteed to be true if the magnetic field is defined as the curl of the vector potential ( $\vec{B} = \nabla \times \vec{A}$ ) as is the case in CENTORI. These are the analytical forms of the equations that are solved in CENTORI but the actual code solves normalized versions of these equations. These are further re-formulated so as to suit the requirements of simulating the system in a discretized manner. There is also Ohm's Law:

$$\vec{E} = -\frac{\vec{v}_i \times \vec{B}}{c} + \frac{\vec{J} \times \vec{B}}{en_e c} + \eta \vec{J} - \frac{\nabla p_e}{en_e} \quad (3.25)$$

$$\eta = \text{resistivity} \quad (3.26)$$

The terms on the RHS are due to contributions from motion, Hall effect, resistance and pressure gradient in that order.

### 3.4 CENTORI results

Before exploring any potential non-linear dynamics of GAMs in Chapter 4, data on the linear dynamics was acquired. CENTORI runs were executed with a MAST-like configuration. The simulation constructs, using GRASS (GRAd-Shafranov Solver), an equilibrium from the magnetic coil positions and the coil currents specified in an input file. This equilibrium is then used to construct a coordinate system  $(\psi, \theta, \zeta)$ . The grid resolution of the simulation is as follows:  $N\psi = 129$ ,  $N\theta = 65$ ,  $N\zeta = 33$ . The smaller value for  $\zeta$  is due to the fact that the parallel length scales are significantly longer than the two perpendicular scales. The time-step is set to  $5 \times 10^{-10}$ s, the equilibrium is re-evaluated every 500 time-steps and the code outputs physical quantities at an interval of  $2.5 \times 10^{-6}$ s (every 5000 time-steps). A full run is  $5 \times 10^{-3}$ s. Even allowing for  $1 \times 10^{-3}$ s to  $2 \times 10^{-3}$ s to let the simulation stabilize from the input configuration, the full timespan should be enough to allow approximately 30 oscillations of GAM. This is with  $f_{GAM} \approx 10$ kHz for a typical MAST discharge with edge temperature  $\sim 0.1$ keV [45]. Given the GAMs low poloidal mode number and relatively small radial wave number [10],



the grid resolution should be enough to capture not only GAMs but also significantly smaller structures that may influence the GAM behaviour. The reference magnetic field strength is 0.5T, the plasma current is set to  $1 \times 10^6$ A. The starting electron number density is  $5 \times 10^{19}$ per m<sup>3</sup>, the initial electron temperature is set to 1.5keV and the initial ion temperature is set to 2.0keV. The initial profile for the electron number density is defined as:  $n_e(\rho, \theta, \zeta) = n_{e0} \exp(-\alpha_{ne}\rho)$ , the coefficient  $\alpha_{ne}$  is user-defined, 1.6 in the case of this simulation. The initial profiles for the initial ion and electron temperatures follow the same form with different coefficients,  $\alpha_{ti}$  and  $\alpha_{te}$ , that are user-defined, 3.0 for both for this simulation. The Alfven speed is  $\sim 1.35 \times 10^8$ cms<sup>-1</sup> and the Alfven time-scale is  $\sim 4 \times 10^{-7}$ s. Typical sound speed at the outer edge of the plasma is  $\sim 10^7$ cms<sup>-1</sup> and sound time-scale is  $\sim 5 \times 10^{-6}$ s.

### 3.4.1 Continuous wavelet transform (CWT)

To understand the temporal, spatial and frequency domain structure of GAMs, some form of transform is required. Usually this involves taking the Fourier transform of a 2D time-space data, this reveals frequency and spatial wavenumber domain structure. However to show the time-evolution of the frequency domain structure a time-series must be windowed such that the windows overlap. Fourier transforms are then performed over these overlapping windows and thus some structure is recovered. The issue is that the quality of Fourier transform depends heavily on the length of the data and the stationarity of the signal being decomposed. Given the average length of pulse( $\sim O(0.1$ s)) in MAST and the period of a GAM oscillation( $\sim O(0.1$ ms)), analysing MAST data using Fourier transforms is viable but the time-span for the simulation presented here is 5ms of which 1.25ms is usable. Continuous wavelet transforms by contrast fit a series of time and frequency localized wavelets and are thus more tolerant to non-stationary signals in data with a limited time-span. The general definition of the continuous wavelet transform (CWT) is:

$$X(s, b) = \frac{1}{\sqrt{s}} \int_{-\infty}^{\infty} x(t) \phi^* \left( \frac{t-b}{s} \right) dt \quad [46] \quad (3.27)$$

Here,  $x(t)$  is the time series signal,  $\phi^*(t)$  is the complex conjugate of the so-called mother wavelet. This mother wavelet is the comparable to the sine function in a Fourier transform and the variables  $s$  and  $b$  are analogous to the frequencies used to localise a Fourier component. However, in this case the two variables correspond to the width and offset of

the wavelet (with the width being closer to the frequency scaling in a Fourier transform). The pure  $\phi^*(t)$  is the mother wavelet and the variables ( $s$  and  $b$ ) are used to generate so-called daughter wavelets which decrease in amplitude as the scale,  $s$ , increases. The particular choice of the mother wavelet is fundamental to the quality and relevancy of the transformed data. For the case of GAMs it is useful to prioritise frequency resolution as opposed to time-resolution (but without completely disregarding the time-resolution). To this end, a wavelet in MATLAB known as the ‘bump’ wavelet is used for the CWT[8], an example of this is shown in Fig. 3.3a. This wavelet provides an increased frequency resolution but diminished time resolution when compared with the widely-used Morlet wavelet[47] as shown in Fig. 3.3.

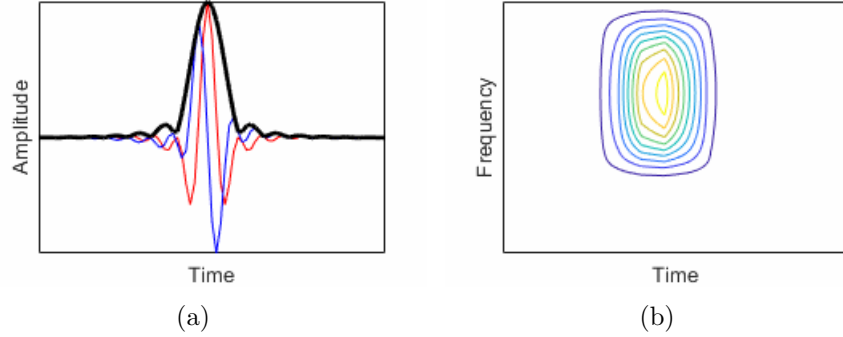


Figure 3.3: (a) Plot of the structure of the ‘bump’ wavelet from the MATLAB documentation.[8] (b) The frequency-time domain structure of the ‘bump’ wavelet. [8]

The frequency-domain definition of is:

$$\phi(s\omega) = \exp\left(1 - \frac{1}{1 - \frac{(s\omega - \mu)^2}{\sigma^2}}\right) I_{[(\mu - \sigma)/s, (\mu + \sigma)/s]} \quad (3.28)$$

A large number of the parameters present in this definition are not exposed when using the ‘bump’ wavelet in MATLAB. In any case,  $s$  is the scale number which spans between a minimum scale  $s_0 = 2\Delta t$  ( $\Delta t$  is the time-step of the original time-series) and a maximum scale dependent on the signal properties. The values of  $\mu$  and  $\sigma$  determine the structure of the mother wavelet and are 5 and 0.6 respectively by default. The term  $I_{[(\mu - \sigma)/s, (\mu + \sigma)/s]}$  represents an indicator function between  $(\mu - \sigma)/s \leq \omega \leq (\mu + \sigma)/s$ . To ensure not too much frequency resolution is sacrificed, a calculation is performed to determine the smallest frequency range between  $(\mu - \sigma)/s$  and  $(\mu + \sigma)/s$ . For this the definition of the

scales,  $s$ , used for the ‘bump’ wavelet is needed:

$$s = s_0(2^{((Sc)ds)}), \quad (3.29)$$

$$NbSc = \text{integer} \left( \frac{\log_2(\frac{N_t dt}{s_0})}{ds} \right) \quad (3.30)$$

$NbSc$  is the total number of scales,  $Sc$  is any integer from 0 to  $NbSc - 1$ ,  $ds = 0.1$  and  $N_t$  is the number of temporal data points in the original time-series. The smallest frequency range is calculated by choosing the largest  $s$  which occurs at  $Sc = NbSc - 1$ . The frequency resolution is thus calculated to be  $\sim 1.1\text{kHz}$  for a  $1.25\text{ms}$  duration signal. Therefore any results presented in this chapter with frequencies separated by  $> 1.1\text{kHz}$  should be resolvable and valid.

### 3.4.2 Fluctuating Electron Density ( $n_{e1}$ )

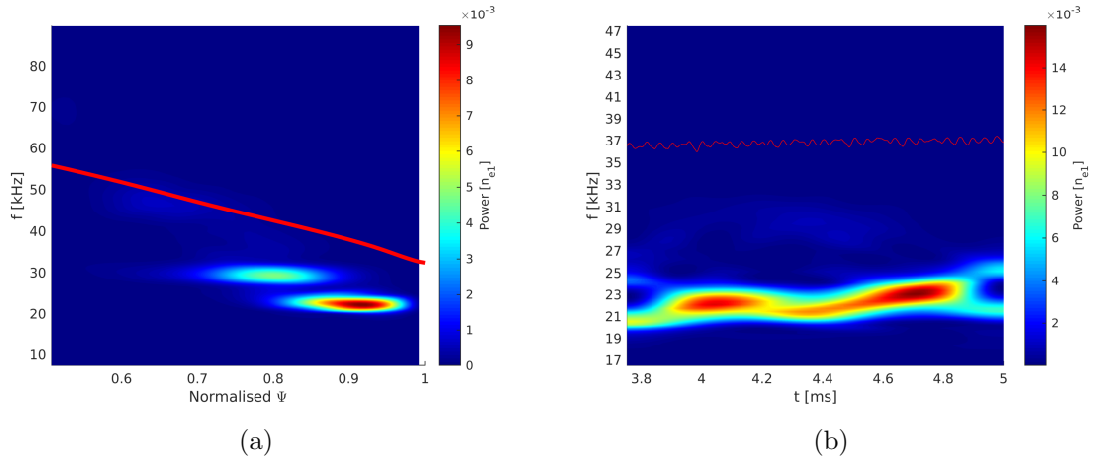


Figure 3.4: (a): CWT of the fluctuating electron density,  $n_{e1}$ , showing frequency as a function of normalised  $\psi$  averaged over 3.75-5ms of the run at a fixed poloidal position of  $\theta = 90^\circ$ . The red line signifies the expected profile of the GAM frequency if it were present across the entire radial extent. (b): CWT showing frequency as a function of time in a fixed radial location,  $\psi = 0.92$ , and a fixed poloidal location,  $\theta = 90^\circ$ , between 17kHz and 47kHz. The red line represents the expected profile of the GAM frequency at this particular location across the time-span calculated based on Eq. (3.31).

Firstly the result for the fluctuating electron density( $n_{e1}$ ) are presented. Figure 3.4a shows a spectrogram showing frequency against radius with two peaks at normalized  $\psi$  of  $\sim 0.8$  and  $\sim 0.92$  at frequencies of  $\sim 30\text{kHz}$  and  $\sim 23\text{kHz}$  respectively. These peaks

extend radially towards each others peak as is evidenced by the faint power signature in Fig. 3.4b at  $\sim 30\text{kHz}$ . The red line represents the expected GAM profile across the radial extent as calculated using the formula:

$$f_{GAM} = \frac{1}{2\pi R} \sqrt{2 + \frac{1}{q^2}} \sqrt{\frac{T_e}{m_i}} = \frac{c_s}{2\pi R_0} \sqrt{2 + \frac{1}{q^2}} \quad (3.31)$$

Here,  $R$  is the local major radius,  $q$  is the local safety factor,  $T_e$  is the local electron temperature,  $m_i$  is the ion mass and  $c_s$  is the sound speed. As major radius increases and electron temperature decreases, local safety factor increases towards the edge of the tokamak, the expected GAM frequency decreases as can be seen in the red line in Figure 3.4a. This expected GAM profile has an overall higher frequency than the one quoted for a typical MAST discharge ( $f \approx 10\text{kHz}$ ). This is consistent with temperatures at the edge being 3-4 times hotter in the simulation compared to typical MAST discharges. Two peaks appear close to the expected GAM profile with the outermost one being the more prominent of the two.

The deviations from the expected GAM dispersion relation ( $\sim 11\text{kHz}$  expected vs.  $\sim 36\text{kHz}$ ) may be due a variety of effects, including a different safety factor profile. For example the local GAM dispersion relation is calculated using Eq. (A.6) which is the formula for a circular cross-section large aspect-ratio tokamak. The effect of elongation,  $\kappa$ , and triangulation,  $\delta$ , may be significant enough to explain the deviation. These are defined as:  $\kappa = (Z_{max} - Z_{min})/2a$  and  $\delta = (R_{geo} - R_{Z_{max}})/a$ . For MAST in this simulation the elongation is  $\kappa = 1.80$  and the triangularity is  $\delta = 0.40$ . A revised definition of GAM frequency is given in Sorokina et al.[48] as:

$$f_{GAM} = \frac{c_s}{2\pi R} \sqrt{\frac{2}{(\kappa^2 + 1)} \left( 2 + \frac{(\kappa^2 + 1)}{2q^2} - \frac{3}{2} \frac{3\kappa^2 + 1}{\kappa^2 + 1} \epsilon^2 + \frac{5\kappa^2 - 1}{2(\kappa^2 + 1)} \epsilon \delta + \frac{17\kappa^2}{16(\kappa^2 + 1)} \delta^2 \right)} \quad (3.32)$$

Here  $\omega_s = c_s/R_0$  is the sound frequency,  $\epsilon = r/R = 0.752$  is the inverse aspect ratio. Substituting in the relevant values for these parameters (with  $q = 3.4$ ) leads to a frequency  $f = 15.1\text{kHz}$  for the location presented in Fig. 3.4b. This is still not accurate per Fig. 3.4b but shows that the effects of plasma shaping can have a significant effect on the GAM frequency and brings the predicted GAM frequency much closer to the 23kHz signal.

More modifications can be made to account for properties such as toroidal Mach number (plasma velocity as a multiple of the speed of sound in the plasma). One such treatment

yields:

$$f_{GAM} = \frac{c_s}{2\pi R} \frac{1}{2} \sqrt{2 + \frac{1}{q^2} + 4M^2 + \left\{ \left( 2 + \frac{1}{q^2} + 4M^2 \right)^2 + \frac{2M^4}{q^2} \right\}^{1/2}} \quad [49] \quad (3.33)$$

This modification increases the GAM frequency with higher toroidal Mach number,  $M$ . However, the toroidal Mach number at the measured radial locations is too low,  $M < 0.1$ , to have a significant impact on the predicted GAM frequency.

Looking at the time-trace for a portion of this run as shown in Figure 3.4b, it's clear that the GAM signal is not constant and shows a low frequency modulation. Having said that however it is present for a sufficient amount of time for multiple oscillations to be observed. This is illustrated in Figure 3.5a, where observing the oscillations between 4-4.8ms it's clear that there are multiple oscillations present. The number of oscillations observed in Figure 3.5a is consistent with the peak in Fig. 3.4b being at  $\sim 23$ kHz.

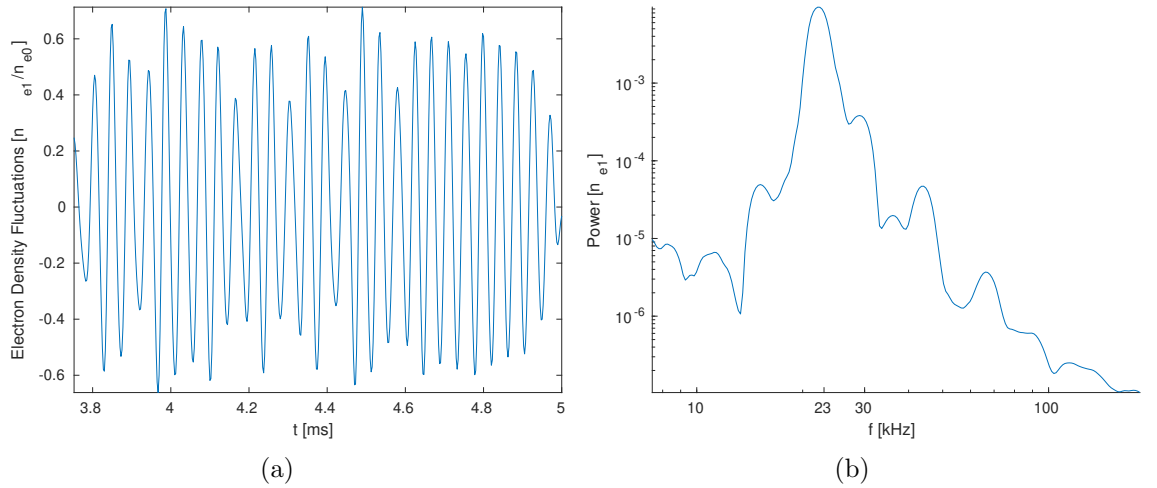


Figure 3.5: (a): Filtered time trace showing the fluctuating electron density,  $n_{e1}$ , for frequencies between 17kHz - 47kHz at radial location of 0.92 and a poloidal angle of  $90^\circ$ . (b): Power spectrum of the fluctuating electron density,  $n_{e1}$ , across the 3.75-5ms time-span in a fixed radial position, 0.92, and poloidal angle,  $90^\circ$ .

As demonstrated in Figure 3.5b, there are indeed peaks in the power spectrum at both higher and lower frequencies to the main peak. However, the peaks are orders of magnitude lower than they appear since this is a log-log plot. An area of interest is the peak directly adjacent to the main peak at 23kHz, the peak in power here may be due to the 30kHz signal that appears at a normalized radial position of 0.8. This is not to say that the 30kHz isn't GAM but that it is not consistent with GAM frequency at this

radial location.

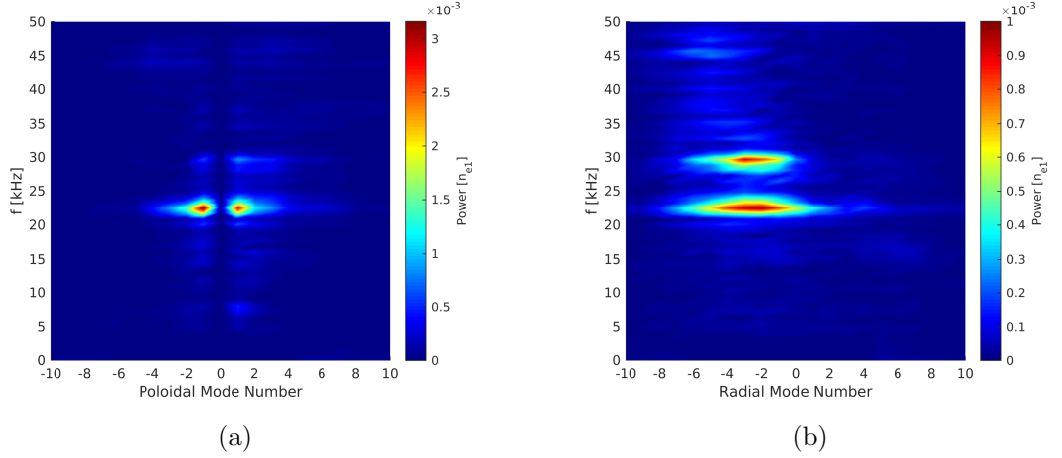


Figure 3.6: (a): Fourier transform of fluctuating electron density,  $n_{e1}$ , showing frequency vs. poloidal mode number at a fixed radial location, 0.92. (b): Fourier transform of fluctuating electron density,  $n_{e1}$ , showing frequency vs. radial mode number at a fixed poloidal angle,  $90^\circ$ .

To confirm the presence of GAM it is essential to establish the spatial mode structure of the observed signal. This is illustrated in Figures 3.6a and 3.6b, for poloidal and radial mode structure respectively. Both figures are generated using a discrete 2D FFT(Fast Fourier Transform)[50]. Figure 3.6a, shows peaks at mode numbers -1 and 1 with a frequency of 23kHz, this is localised in poloidal mode number, which indicates GAM. There is also a faint peak at a frequency of 30kHz with  $m = \pm 1$ . Figure 3.6b, by contrast shows two peaks, however the peak at 30kHz is weaker and since this plot considers the whole radial extent it may be a marker for the peak present in Figure 3.4a at the radial location 0.8. The symmetric nature of the 23kHz mode in Figure 3.6a indicates a standing wave in the poloidal direction. This is verified by Figure 3.7a where, using the horizontal guide lines(constant time values), it's clear that there is no definitive direction of travel for the signal in either direction. There is a slight gradient indicating a movement of the density towards the in-board side of the tokamak but this could be attributed to the expected over-density of particles towards the in-board side as a result of the shape of the magnetic field. This is especially prevalent in spherical tokamaks where the aspect ratio is minimised in order to improve confinement by keeping the particles in the high-field region of the tokamak(the in-board side) for the maximum amount of time. The equivalent time-trace for the radial direction shows a motion in the outward radial direction. There is no clear radial wave-number as evidenced by Figure

3.6b. The two frequencies present in Figure 3.6b can be clearly seen in different radial locations, backing up the radial profile spectrogram in Figure 3.4a. It is to be noted that the amplitudes of the Fourier transforms does not match the continuous wavelet transforms. This is expected and the scaling between the fluctuating electron density and fluctuating scalar potential is still preserved in both transforms.

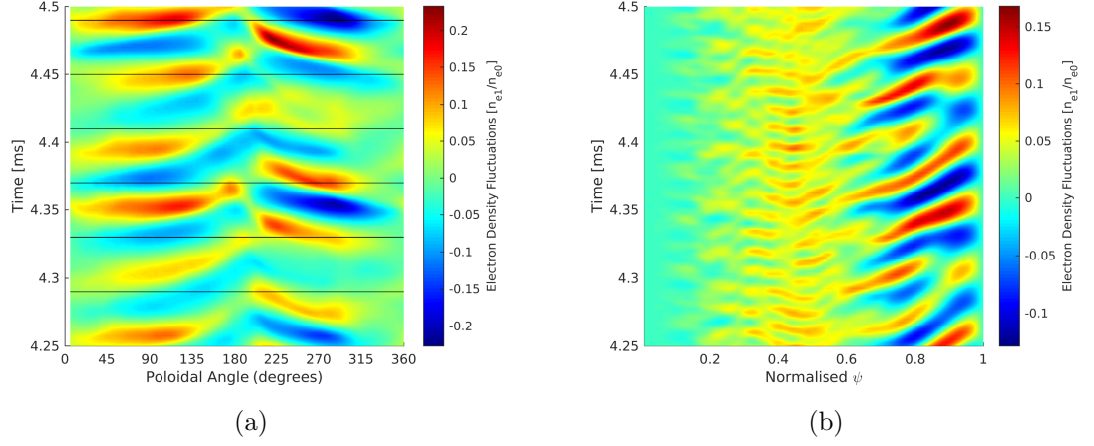


Figure 3.7: (a): Time-space plot of fluctuating electron density,  $n_{e1}$ , vs. poloidal angle. The poloidal angles are such that  $0^\circ$  is the out-board mid-plane and  $90^\circ$  is the point in the tokamak with the highest Z-axis value per Figure 3.2. The radial location is 0.92 (b): Time-space plot of fluctuating electron density,  $n_{e1}$ , vs. normalised  $\psi$  at a poloidal angle  $90^\circ$ .

### 3.4.3 Total Scalar Potential ( $\phi$ )

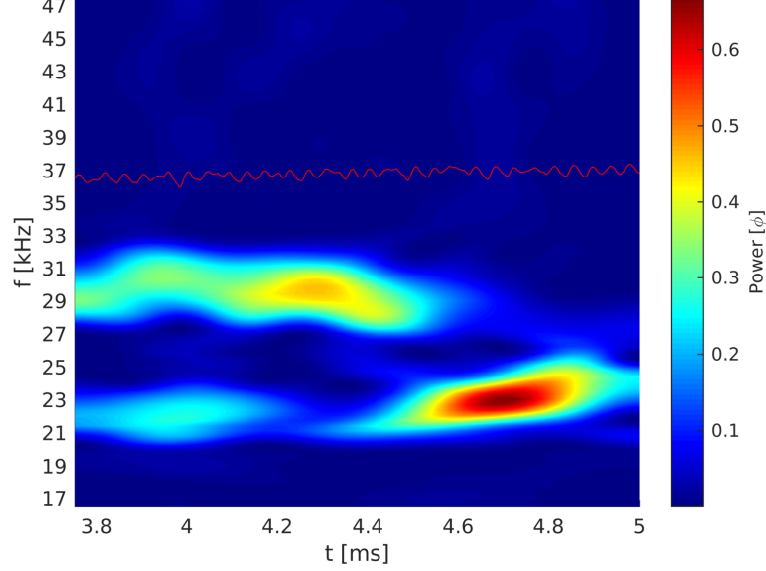


Figure 3.8: CWT of total scalar potential,  $\phi$ , data showing frequency versus time in a fixed radial location, 0.92, and a fixed poloidal location,  $90^\circ$ , between 17kHz and 47kHz. The red line represents the expected profile of the GAM frequency at this particular location across the time-span.

Before looking at the fluctuating scalar potential, data for the total scalar potential,  $\phi$ , is analysed. This is to ensure that any modes (particularly  $m=0$ ) that might be suppressed by the subtraction of averages from the total scalar potential are recorded. The radial profile is not presented here as the radial point at 0.92 is used for all analysis of this data so as to be consistent with the choices made for the fluctuating electron density. The two signals with frequencies of 23kHz and 30kHz are clearly present in Fig. 3.8 but they are not dominant simultaneously. Of the two signals the 23kHz has the highest peak power but not by an order of magnitude. The power spectrum shown in Fig. 3.9b is distinct from Fig. 3.5b and shows that for the total scalar potential the two signals at 23kHz and 30kHz are much closer in power. Whilst this may not be obvious from Fig. 3.8, where the 23kHz has a higher peak power, the 30kHz persists for a longer time and the power spectrum is integrated across the entire time-span, 3.75-5ms. Figures 3.10a and 3.10b show the spatial mode structure of the data. There is clear evidence that the both major frequencies have an  $m=0$  structure and a radial mode number that is  $\sim 0$ . This indicates that both frequencies are GAMs (which has a varying local predicted frequency).



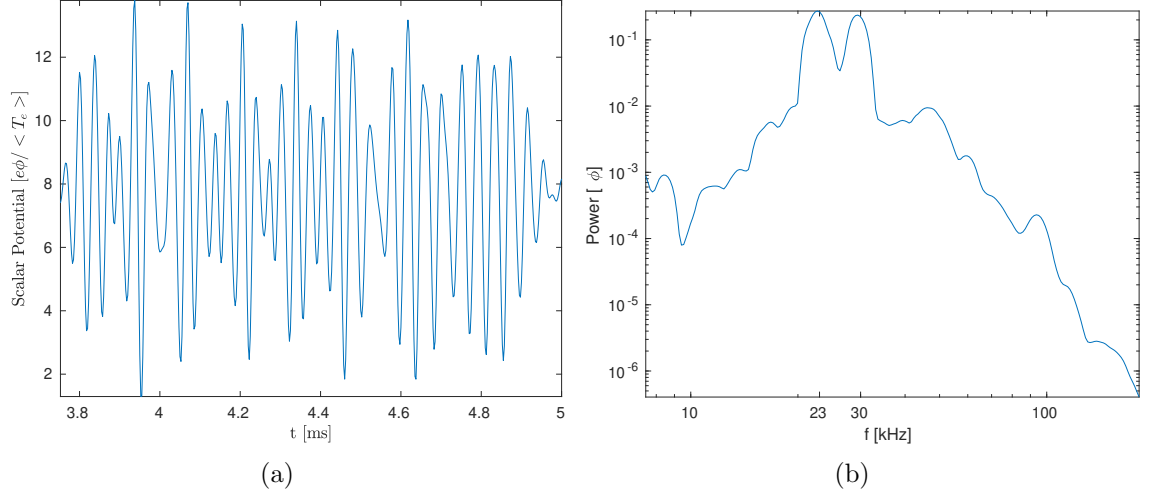


Figure 3.9: (a): Filtered time trace showing the total scalar potential,  $\phi$ , for frequencies between 17kHz - 47kHz at radial location of 0.92 and a poloidal angle of  $90^\circ$ . (b): Power spectrum of the total scalar potential,  $\phi$ , across the 3.75-5ms time-span in a fixed radial position, 0.92, and poloidal angle,  $90^\circ$ .

Figures 3.11a and 3.11b show further evidence of an  $m=0$  mode structure. The normalisation applied here and for Fig. 3.9a is  $e\phi / \langle T_e \rangle$ , where the electron charge,  $e = 1$  for a deuterium plasma and  $\langle T_e \rangle$  is the flux-surface average of the electron temperature. There is minimal radial structure in Fig. 3.11b, at the edge there is a slight sign of movement radially outwards. This may be a relic of the underlying  $\phi_1$  imprinting structure on the otherwise fairly homogeneous total scalar potential.

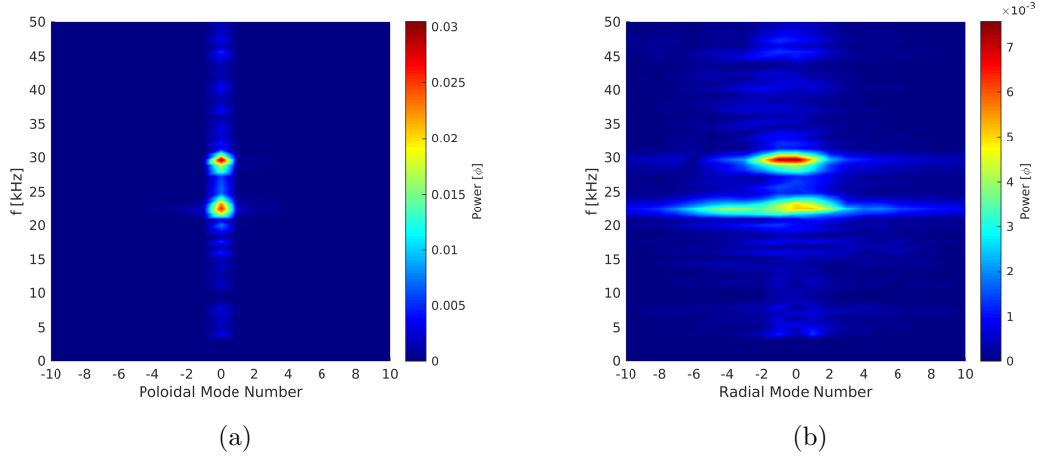


Figure 3.10: (a): Fourier transform of total scalar potential,  $\phi$ , showing frequency vs. poloidal mode number at a fixed radial location, 0.92. (b): Fourier transform of total scalar potential,  $\phi$ , showing frequency vs. radial mode number at a fixed poloidal angle,  $90^\circ$ .

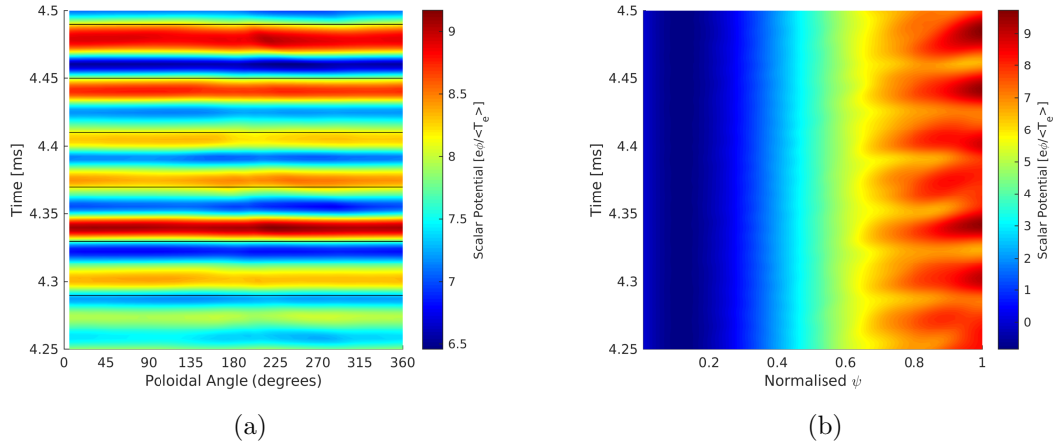


Figure 3.11: (a): Time-space plot of total scalar potential,  $e\phi / \langle T_e \rangle$ , vs. poloidal angle. The poloidal angles are such that  $0^\circ$  is the out-board mid-plane and  $90^\circ$  is the point in the tokamak with the highest Z-axis value per Figure 3.2. The radial location is 0.92. (b): Time-space plot of total scalar potential,  $e\phi / \langle T_e \rangle$ , vs. normalised  $\psi$  at a poloidal angle  $90^\circ$ .

### 3.4.4 Fluctuating Scalar Potential ( $\phi_1$ )

The fluctuating scalar potential,  $\phi_1$ , is defined in the CENTORI output as  $\phi_1 = \phi - \langle \phi \rangle$ , where the  $\langle \phi \rangle$  is the flux-surface average of  $\phi$ . This results in a subtraction of any data pertaining to the  $m = 0$  mode observed previously for the total scalar potential,  $\phi$ . Analysis of  $\phi_1$  is undertaken to investigate the possibility of the fluctuating electron density structure presenting itself in this data. A clear match for an  $m = 1, n = 0$  mode is present here. The frequency is consistent with the predicted GAM frequency and the time trace shown in Figure 3.12 is clearly matched with the equivalent electron density( $n_{e1}$ ) in Figure 3.4b.

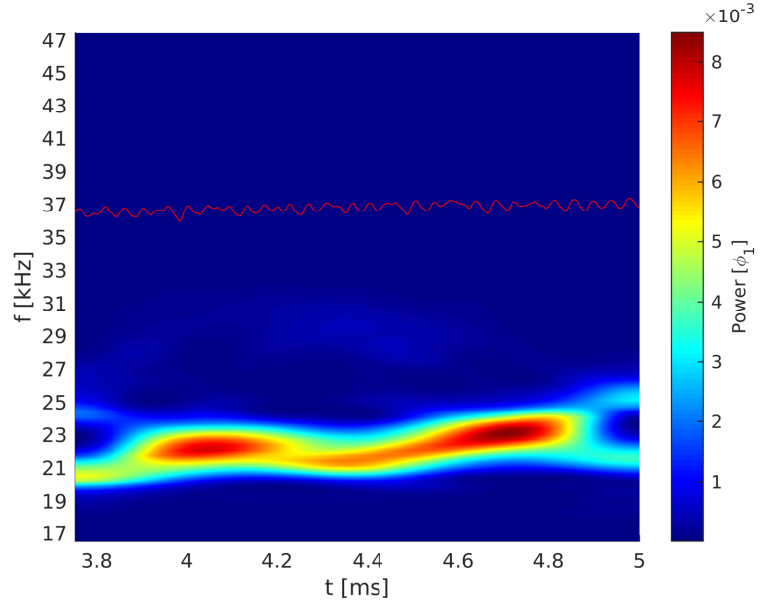


Figure 3.12: CWT showing frequency versus time in a fixed radial location, 0.92. and a fixed poloidal location,  $90^\circ$ , between 17kHz and 47kHz. The red line represents the expected profile of the GAM frequency at this particular location across the time-span.

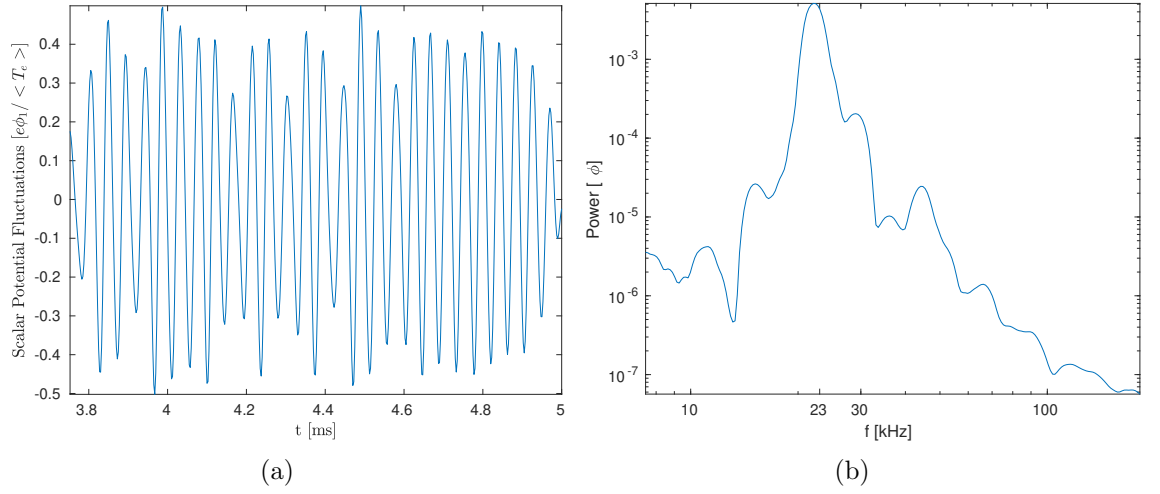


Figure 3.13: (a): Filtered time trace showing the fluctuating scalar potential,  $\phi_1$ , for frequencies between 17kHz - 47kHz at a radial location, 0.92 and a poloidal angle of  $90^\circ$ . (b): Power spectrum of fluctuating scalar potential,  $\phi_1$ , across the 3.75-5ms time-span in a fixed radial position, 0.92, and poloidal angle,  $90^\circ$ .

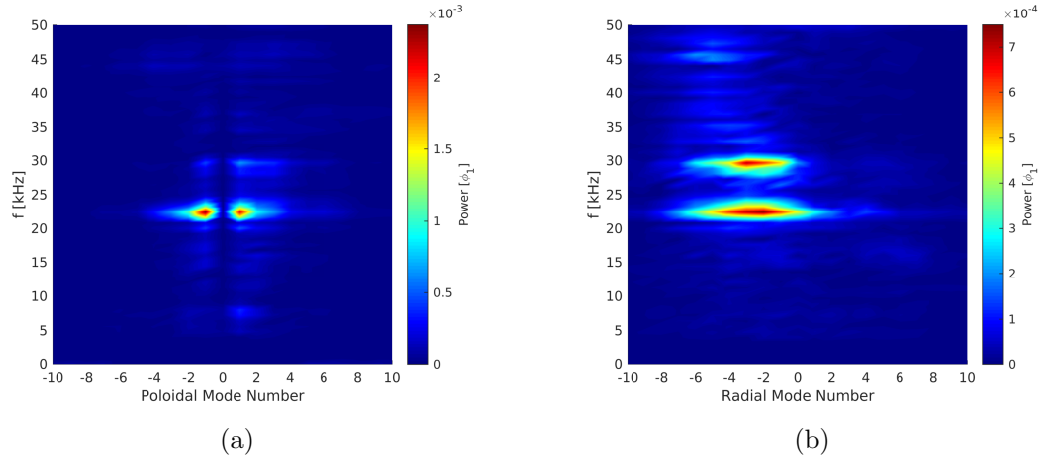


Figure 3.14: (a): Fourier transform of fluctuating scalar potential,  $\phi_1$ , showing frequency vs. poloidal mode number at a fixed radial location, 0.92. (b): Fourier transform of fluctuating scalar potential,  $\phi_1$ , showing frequency vs. radial mode number at a fixed poloidal angle,  $90^\circ$ .

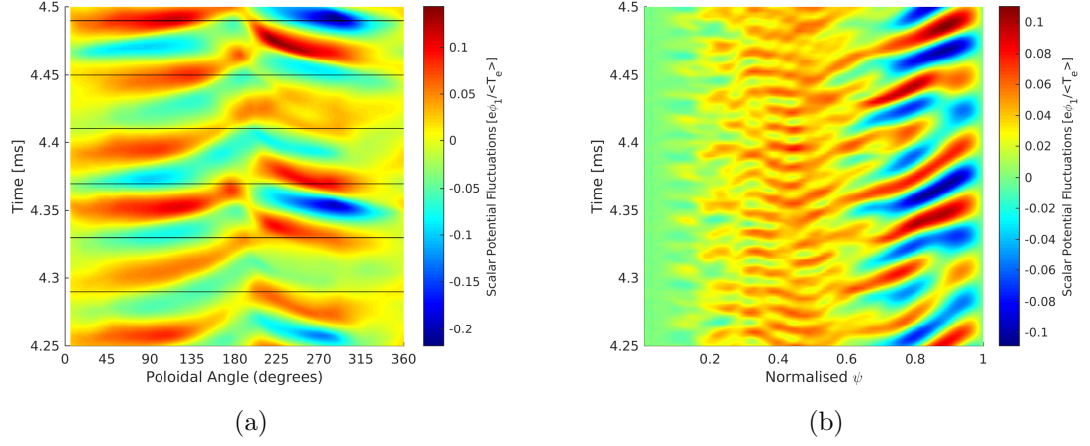


Figure 3.15: (a): Time-space plot of fluctuating scalar potential,  $\phi_1$ , vs. poloidal angle. The poloidal angles are such that  $0^\circ$  is the out-board mid-plane and  $90^\circ$  is the point in the tokamak with the highest Z-axis value per Figure 3.2. The radial location is 0.92. (b): Time-space plot of fluctuating scalar potential,  $\phi_1$ , vs. normalised  $\psi$  at a poloidal angle  $90^\circ$ .

The scales for  $\phi_1$  in these plots are comparable to those used for the  $n_{e1}$ , however they are consistently slightly lower than that of the electron density. The overall structure of the mode observed for the fluctuating scalar potential is also near-identical to the mode observed for the electron density. This presents a challenge in comparing the potential and the electron density since the definition for the fluctuating electron density is also based on subtracting the flux-surface average from the total electron density. The remaining analysis of the data for the fluctuating scalar potential matches the fluctuating electron density within a factor 1-3 depending on whether power or amplitudes are compared.

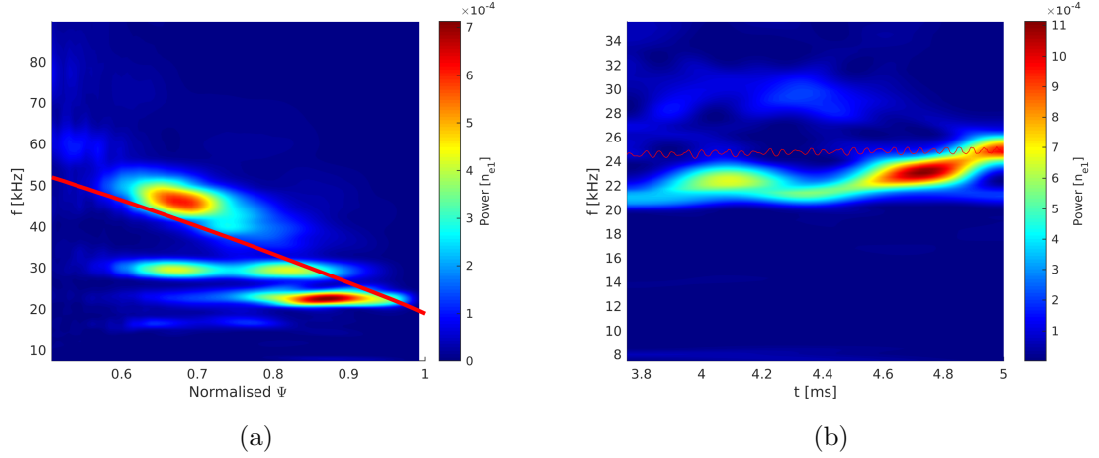


Figure 3.16: (a): CWT of the fluctuating electron density,  $n_{e1}$ , showing normalised  $\psi$  versus frequency averaged over 3.75-5ms of the run at a fixed poloidal position of  $\theta = 0^\circ$ . The red line signifies the expected profile of the GAM frequency if it were present across the entire radial extent. (b): CWT showing frequency versus time in a fixed radial location, 0.92, and a fixed poloidal location,  $0^\circ$ , between 17kHz and 47kHz. The red line represents the expected profile of the GAM frequency at this particular location across the time-span.

### 3.4.5 Outboard Mid-Plane Fluctuating Electron Density ( $n_{e1}$ )

Driven by many reports of GAM-like oscillations observed at the  $\theta = 0^\circ$ , the analysis is extended to the outboard mid-plane data, it is clear that there are several differences when compared to the  $90^\circ$  poloidal angle data. This is to be expected, as the  $m = 1$  modes of frequencies 23kHz and 30kHz reduce in power as the poloidal angle approaches  $0$ , weaker modes at different frequencies will appear more comparable to the 23kHz and 30kHz signals in power and amplitude. There is now an additional mode at  $\sim 0.7$  at  $\sim 50$ kHz as well as  $\sim 30$ kHz. All of the major modes, with the exception of the mode at 0.7 and 30kHz, fit well with the predicted GAM radial profile— this can be seen more clearly in Fig. 3.16b. It should be noted however that the amplitude and the power are severely reduced in this location, with the power being reduced by an order magnitude and the amplitude (seen in Fig. 3.18b) being reduced by a factor of  $\sim 4$ -5. Furthermore the power spectrum is also distinct from Fig. 3.5b in this location. The peak at 30kHz is now closer in value to the main peak at 23kHz as are other peaks on the higher frequency side of the main peak. There also seems to be more power in the low-frequency region but this does not exceed the power of the main peak. Figures 3.18a and 3.18b (which take into account the full radial extent) show that the reduced energy is now localised further inwards towards the core and if the power spectrum, Fig. 3.17b, were observed at  $\sim 0.5$  then the 30kHz peak would dominate.

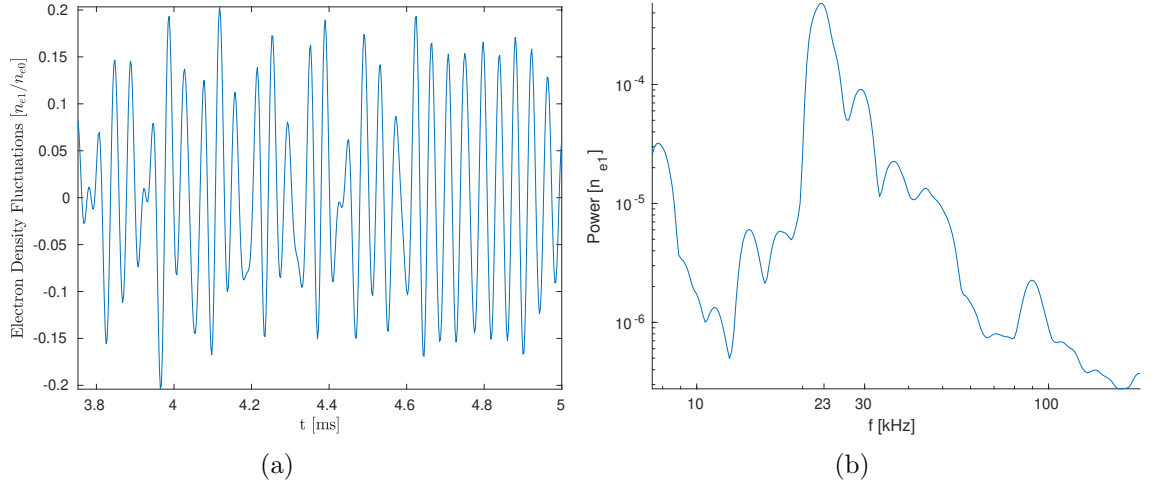


Figure 3.17: (a): Filtered time trace showing the fluctuating electron density,  $n_{e1}$ , for frequencies between 17kHz - 47kHz at radial location of 0.92 and a poloidal angle of  $0^\circ$ . (b): Power spectrum of the fluctuating electron density,  $n_{e1}$ , across the 3.75-5ms time-span in a fixed radial position, 0.92, and poloidal angle,  $0^\circ$ .

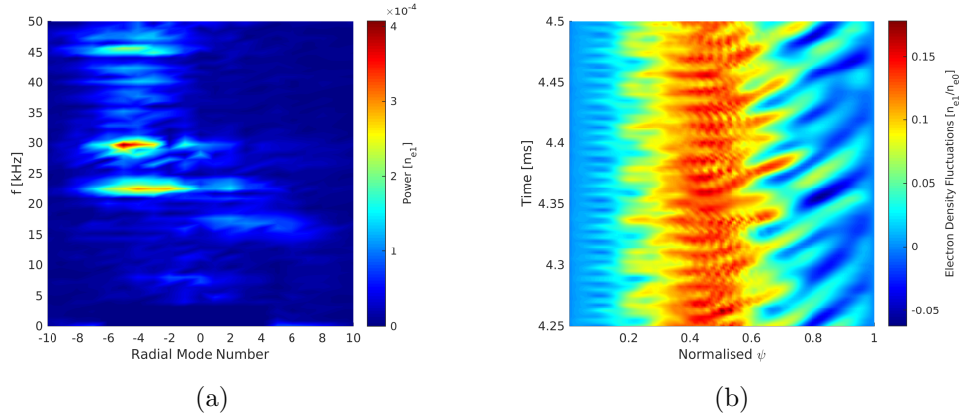


Figure 3.18: (a): Fourier transform of fluctuating electron density,  $n_{e1}$ , showing frequency vs. radial mode number at a fixed poloidal angle,  $0^\circ$ . (b): Time-space plot of fluctuating electron density,  $n_{e1}$ , vs. normalised  $\psi$  at a poloidal angle  $0^\circ$ .

### 3.4.6 Outboard Mid-Plane Scalar Potential ( $\phi$ )

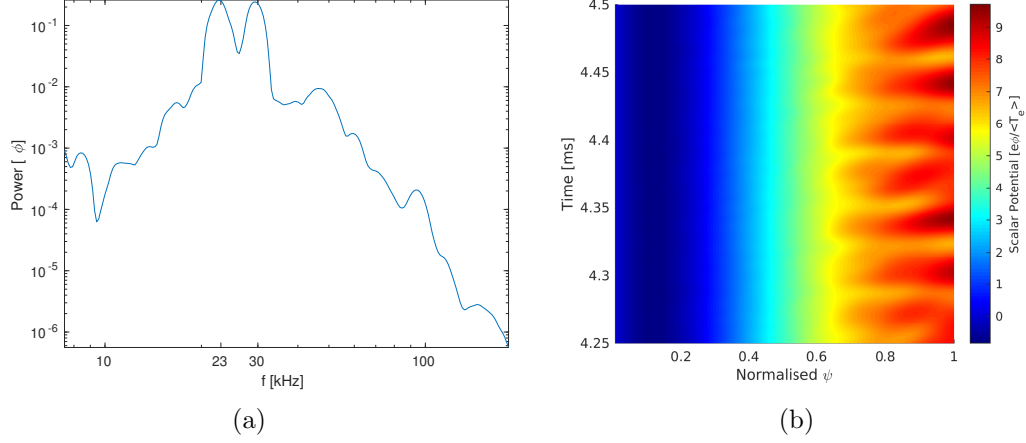


Figure 3.19: (a): Filtered time trace showing the fluctuating scalar potential,  $\phi_1$ , for frequencies between 17kHz - 47kHz at radial location of 0.92 and a poloidal angle of  $0^\circ$ . (b): Time-space plot of fluctuating scalar potential,  $\phi_1$ , vs. normalised  $\psi$  at a poloidal angle  $0^\circ$ .

To confirm the  $m=0$  structure of the modes observed for the total scalar potential, the outboard mid-plane data for this quantity is also analysed. The power and amplitudes in both Figs. 3.19a and 3.19b are unchanged from those recorded at a poloidal angle of  $90^\circ$ . The structure of the power spectrum and the time-space plot for the radial extent at the mid-plane also show no significant changes to the previously recorded data. This confirms the  $m=0$  mode structure for the signals observed in the total scalar potential.

## 3.5 Summary

The work in this chapter offers an introduction into the analysis of GAM. A derivation of the GAM frequency is shown following the seminal Winsor paper[39]. This serves as a starting point to introduce data from a simulation, CENTORI[7], and the subsequent analysis. The analysis shows the presence of a clear  $m = 1$  mode with a frequency of 23kHz in the vicinity of the predicted GAM frequency for the fluctuating electron density,  $n_{e1}$ . A mode with the same frequency of 23kHz is found to have an  $m=0$  structure in the analysis of the total scalar potential,  $\phi$ , indicating geometric coupling. The expected GAM frequency is calculated using a simplistic local dispersion relation that neglects shaping and plasma velocity effects. True comparison between the amplitudes and the powers of



$n_{e1}$  is  $\phi$  is difficult since one is a fluctuating quantity and the other is a total quantity. However both quantities can be compared with respect to spatial and frequency structure. Due to the subtraction of the flux-surface average when determining the fluctuating scalar potential,  $\phi_1$ , it is impossible to recover any  $m=0$  modes, therefore comparison between  $\phi$  and  $n_{e1}$  is preferred. The outboard mid-plane data is also investigated and found to be consistent with predictions of an  $m = 1$  mode for the electron density, and an  $m = 0$  mode for the total scalar potential.

The next step is to investigate the non-linear and/or self-interacting nature of GAMs, which will use the results derived from the data analysis presented in this chapter as a starting point.

## Chapter 4

# Non-Linear GAM Properties

### 4.1 Introduction

With the linear physics associated with GAMs verified for CENTORI in the previous chapter, the non-linear physics of GAMs will be investigated in this chapter. In particular, the self-interaction of the GAM mode which has been observed experimentally[51] to generate a mode with double the frequency. Any self-interaction may point to another avenue of energy transfer from GAM to higher frequencies (and/or higher harmonics). The identification of GAM self-interaction in data from CENTORI would also act as a validation to theoretical results as well, such as those shown in Sasaki et al.[52]. Additionally any interaction of the GAM mode with lower frequency modes could indicate LFZF-GAM (Low Frequency Zonal Flow - Geodesic Acoustic Mode) coupling which would generate a triplet of (LFZF, GAM, Turbulence). In addition, any three-wave non-linear coupling which could mediate the energy from GAMs and LFZFs(Low Frequency Zonal Flows) back to turbulent scale are of interest as well[53].

To investigate this type of coupling, bicoherence analysis is applied to the same data from CENTORI as used in Chapter 3. This type of analysis is well established and details on its applicability in analysing non-linear wave coupling can be found in Kim et al.[54]. Work relating to the analysis of plasma turbulence (space plasma) in particular can be found in Dudok de Wit 2003[55]. A series of papers by Ritz et al. show the use of bicoherence analysis to investigate tokamak turbulence, its association with energy cascade and its onset in transitioning flow[56][57][58].

## 4.2 Methodology

Bicoherence analysis involves observing the phase-matching of two modes per specific resonant conditions. These resonant conditions are defined as:

$$f_3 = f_1 + f_2 \quad (4.1)$$

The frequencies,  $f_1$  and  $f_2$ , correspond to the two waves in question and  $f_3$  is the frequency of the wave that is generated as a result of the coupling between  $f_1$  and  $f_2$ . This technique has been used previously in a plasma physics context, for example: Balikhin et al.[59] on magnetospheric data to investigate the role of non-linear coupling in generating turbulent fluctuations; Dudok de Wit et al. [60] which also looks at magnetospheric data but approaches the bicoherence analysis as a wavelet transform description instead of Fourier; Dos Santos Lima et al.[61] which looks at broadband turbulence generation in tokamak plasmas due to low-frequency magnetohydrodynamic modes. Before fully defining the bicoherence equation, a definition for the bispectrum equation is necessary. Let  $x(t)$  be a stationary time-dependent signal then the continuous wavelet transform can be labelled as  $X(f)$  with the definition given in Eq. (3.27) with  $a \equiv f$  and  $b$  being the time coordinate needed for the averaging in the bispectrum (given the averaging, the time argument is neglected when referring to  $X(f)$ ). The bispectrum is defined as:

$$B_S^2(f_1, f_2) = |\langle X^*(f_1)X^*(f_2)X(f_3) \rangle|^2 \quad (4.2)$$

The  $X^*(...)$  is the complex conjugate of the transform, the  $\langle ... \rangle$  indicates the averaging over time. Ordinarily this would be an average over an ensemble of windowed Fourier transforms. However, with CWTs there is an in-built time-resolution since it uses wavelets that are localised in both the frequency and time domain. The bicoherence is then a normalized version of the bispectrum. There are a few methods of normalization, the method presented here can be found in Hajj et al.[62]:

$$B_C^2(f_1, f_2) = \frac{B_S^2}{\langle |X(f_1)X(f_2)|^2 \rangle \langle |X^*(f_1 + f_2)|^2 \rangle} = \frac{|\langle X^*(f_1)X^*(f_2)X(f_3) \rangle|^2}{\langle |X(f_1)X(f_2)|^2 \rangle \langle |X(f_3)|^2 \rangle} \quad (4.3)$$

The result of Eq. (4.3) varies 0 and 1 and the value now provides measure of the amount of non-linear coupling between modes with frequencies  $f_1$  and  $f_2$ . It is worth noting however that this value does not recover any information regarding the direction of energy transfer. Nevertheless there is some insight to be gained by confirming whether there is

any self-interaction of any stationary modes or whether there are any other frequencies that are coupled with higher frequencies.

A different technique needed for analysing non-stationary interactions is cross-bicoherence. The non-stationary nature of the interactions can be spatial and/or temporal, with each type requiring special treatment. If the interaction is spatially non-stationary then two time series are needed with each coming from a suitably separated spatial location, these can be written as:  $x_1(t)$  and  $x_2(t)$ . The temporally non-stationary case (ie. intermittent/pulsed interactions) must also have two time series but from the same spatial location. The difference between the two time series is a time shift of one of the signals,  $\delta t$ , such that the two signals can be written as:  $x_1(t)$  and  $x_1(t - \delta t)$ . In either the spatial or temporal case the two time series generate two distinct CWTs and for illustrative purposes they are labelled as:  $X(f)$  and  $Y(f)$ . With these two CWTs the cross-bicoherence can be defined as[62]:

$$B_C^2(f_1, f_2) = \frac{|\langle X^*(f_1)X^*(f_2)X(f_3)Y(f_1)Y(f_2)Y^*(f_3) \rangle|^2}{\langle |X^*(f_1)X^*(f_2)X(f_3)|^2 \rangle \langle |Y(f_1)Y(f_2)Y^*(f_3)|^2 \rangle} \quad (4.4)$$

The spatial and temporal shifts must be chosen carefully to ensure a sufficient window in which the waves of interest are coherent enough to interact non-linearly.

### 4.3 Results

The results presented here are based on data from the same simulations as reported in Chapter 3. Firstly, power spectra are presented to highlight key features and frequencies of interest. Next the results of the bicoherence analysis are presented, either unfiltered or filtered.

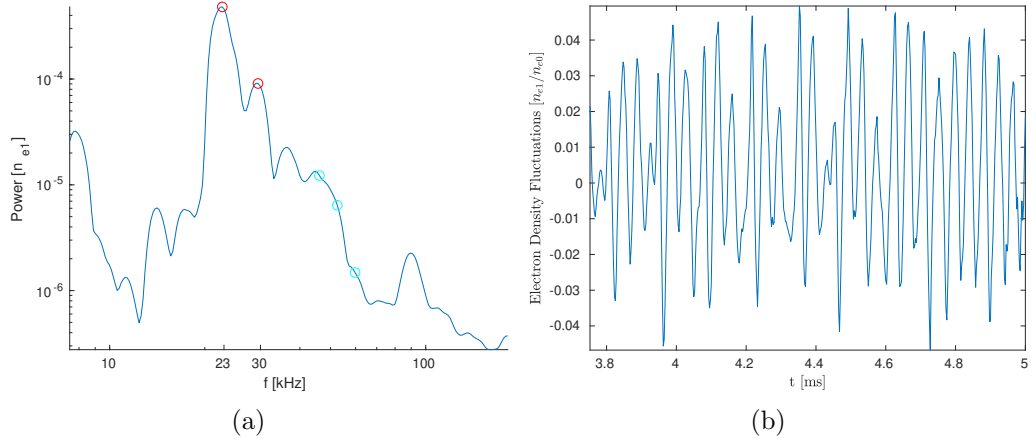


Figure 4.1: (a) Power spectrum of the fluctuating electron density,  $n_{e1}$ . The power spectrum is averaged over the time-span of 3.75-5ms at a radial location of 0.92 and poloidal angle of  $0^\circ$ . The red circles are aligned with the two main frequencies of interest, 23kHz and 30kHz. The cyan circles are aligned with the interaction frequencies of 46kHz, 53kHz and 60kHz. (b) Shows an unfiltered time trace of the fluctuating electron density,  $n_{e1}$ , at a radial location of 0.92 and a poloidal angle of  $0^\circ$ .

#### 4.3.1 Outboard Mid-Plane Fluctuating Electron Density ( $n_{e1}$ )

Firstly, Fig. 4.1 shows the power spectrum for  $n_{e1}$  data taken at the outboard mid-plane and shows the dominant peak at a frequency of 23kHz and a secondary peak at 30kHz. The outboard mid-plane was chosen so as to minimise the power in GAM and allow other interactions to become more visible. Weak turbulent fluctuations in particular should be more prevalent at the outboard mid-plane as the magnetic field is at its weakest and thus the plasma is most vulnerable to unstable interchange modes which lead to turbulence. In accordance with the two dominant peaks in Fig. 4.1, there are three red guidelines overlain on the bicoherence plot shown in Fig. 4.2. These guidelines act as markers for three possible interactions: ( $23\text{kHz} + 23\text{kHz} = 46\text{kHz}$ ), ( $23\text{kHz} + 30\text{kHz} = 53\text{kHz}$ ) and ( $30\text{kHz} + 30\text{kHz} = 60\text{kHz}$ ). Two of these represent self-interaction whilst the remaining presents an interaction between two GAM-like modes. Note that since bicoherence analysis does not provide the direction of energy transfer in a non-linear interaction, the three interactions can be more appropriately considered as triplets where any frequency can transfer the power from the other/s.

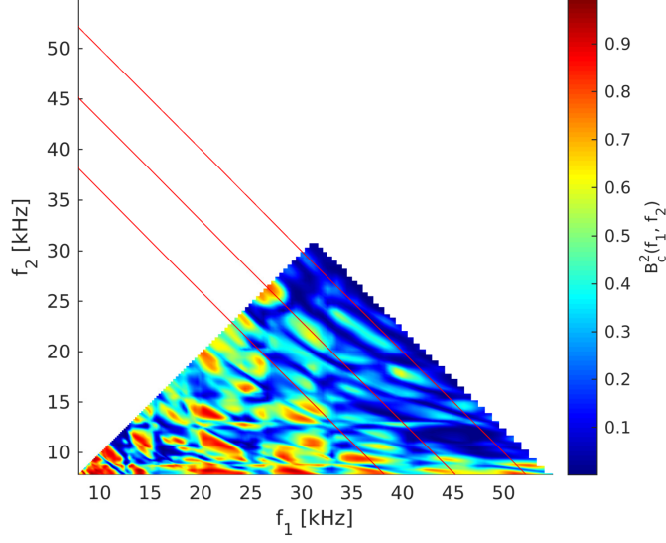


Figure 4.2: Bicoherence of the fluctuating electron density,  $n_{e1}$ , at a radial location of 0.92 and poloidal angle of  $0^\circ$ . There is a time shift of  $0.047ms \sim T_{GAM}$ , where  $T_{GAM}$  is the approximate time period of the 23kHz mode. This plot is unfiltered therefore the bicoherence values range from 0-1.

An example of this bicoherence is shown in Fig. 4.2, where the plot is unfiltered. The time shift of  $T_{GAM} \sim 0.047ms$  is chosen so as to allow the GAM to remain coherent between the two shifted time coordinates for long enough to interact with other modes. The figure shows a high level of coupling between the GAM mode at 23kHz and lower frequency modes which may be LFZFs (low-frequency zonal-flows). This region of interaction occurs around  $f_1 = 23kHz$  and  $f_2 = 10 - 15kHz$ . The resulting  $f_3$  would then be  $\sim 33 - 38kHz$ . There is a small peak in the power spectrum around the values for  $f_3$  but much weaker structures for the  $f_1 = 10 - 15kHz$  region. Furthermore there are clear indications of interactions near/on the three guidelines, which would result in non-linear interactions affecting the power at the frequencies,  $f_3$ , represented by the guidelines with  $f_3 = 46, 53, 60kHz$ .

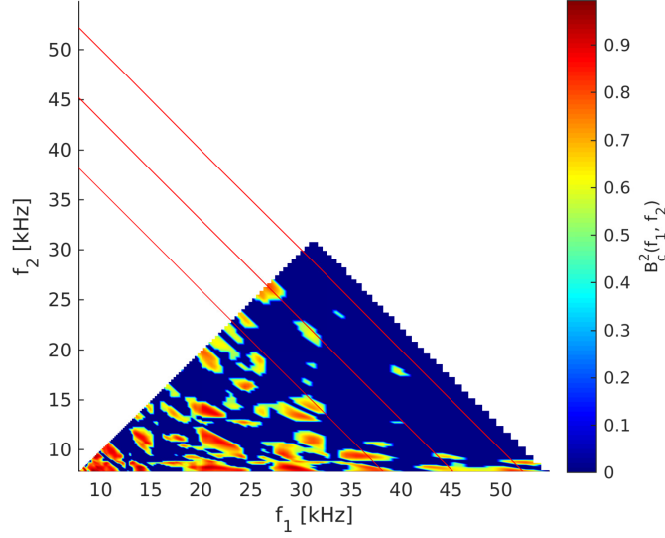


Figure 4.3: Bicoherence of the fluctuating electron density,  $n_{e1}$ , at a radial location of 0.92 and poloidal angle of  $0^\circ$ . There is a time shift of  $0.047ms \sim T_{GAM}$ , where  $T_{GAM}$  is the approximate time period of the 23kHz mode. This plot is filtered to exclude values below 0.5.

Figure 4.3 shows the results of filtering the data from Fig. 4.2 to exclude values  $\leq 0.5$ . The filtering eliminates weak coherence found at higher frequencies on both axes and exposes the fact that the majority of the strong coherence exists at lower frequencies in the region of 10 – 30kHz. Figure 4.4 shows bicoherence with a filter applied to exclude values below 0.75 resulting in further localisation to low frequency interactions. For the case of self-interaction of the 23kHz and 30kHz modes one would expect peaks on the diagonal (eg.  $f_1 = f_2 = 23\text{kHz}$  and  $f_1 = f_2 = 30\text{kHz}$ ) but there are only weak peaks with large spreads in frequency-space in the 0.75 filtered plot. The higher coherence peaks exist instead between the 23kHz mode and lower frequency modes 10-15kHz and to a lesser extent between 30kHz and the same lower frequency modes. Another highly localised peak appears at  $f_1 \approx 30\text{kHz}$  and  $f_2 \approx 23\text{kHz}$  on the  $f_3 = 53\text{kHz}$  guideline, this can be seen more clearly in Fig. 4.2. There is one peak on a diagonal, at  $f_1 = f_2 \approx 26\text{-}27\text{kHz}$  with  $f_3 = 53\text{kHz}$ , however there is little indication in the power spectrum of any significant power at these frequencies. This may be due to the fact that CWTs have poorer frequency resolution compared to Fourier transforms. What may be contributing to this apparent self-interaction is interaction between different peaks within the main GAM peak at 23kHz which cannot be resolved in the power spectrum as it is based on data from CWTs.

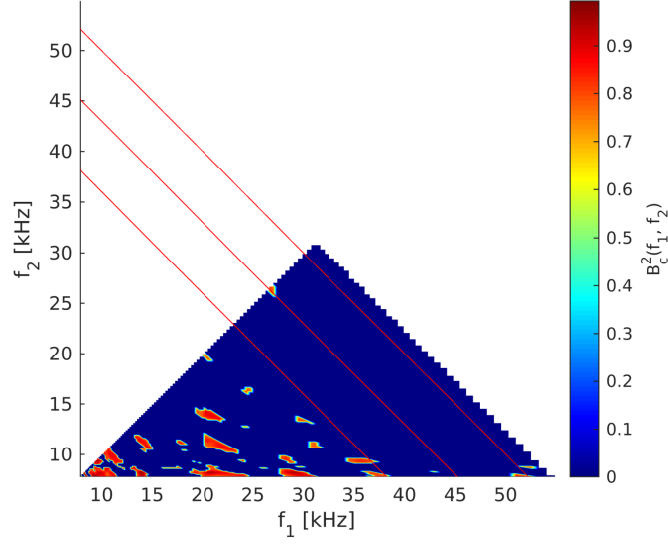


Figure 4.4: Bicoherence of the fluctuating electron density,  $n_{e1}$ , at a radial location of 0.92 and poloidal angle of  $0^\circ$ . There is a time shift of  $0.047ms \sim T_{GAM}$ , where  $T_{GAM}$  is the approximate time period of the 23kHz mode. This plot is filtered to exclude values below 0.75.

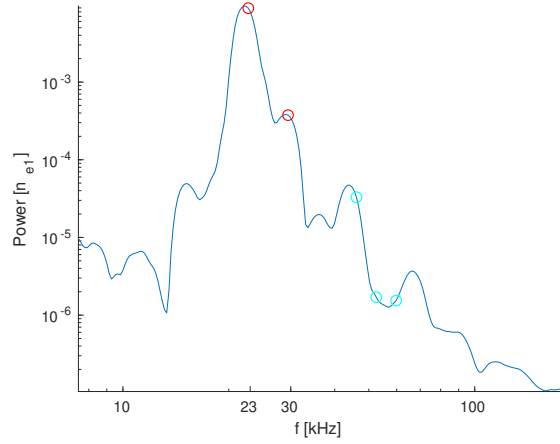


Figure 4.5: Power spectrum of the fluctuating electron density,  $n_{e1}$ . The power spectrum is averaged over the time-span of 3.75-5ms at a radial location of 0.92 and poloidal angle of  $90^\circ$ . The red circles are aligned with the two main frequencies of interest, 23kHz and 30kHz. The cyan circles are aligned with the interaction frequencies of 46kHz, 53kHz and 60kHz.



### 4.3.2 Fluctuating Electron Density ( $n_{e1}$ ), $\theta = 90^\circ$

This section examines the same fluctuating electron density at  $\theta = 90^\circ$ . Note that though the relative increase in magnetic field strength at this poloidal angle for a spherical tokamak with high triangularity may exceed the expected increase in magnetic field strength of a circular cross-section, large aspect-ratio tokamak. This is because the radial location of the  $\theta = 90^\circ$  location may be closer to the central solenoid than the magnetic axis of the tokamak. Hence the reduction in turbulence may be larger than expected. The power spectrum in Fig. 4.5 shows significant deviation from Fig. 4.1. Mainly the absolute and relative power of the 23kHz mode is increased at this poloidal location (in line with an  $m = 1$  structure). The relative suppression in power of modes of lower or higher frequencies than 23kHz should also suppress coupling of other modes to 23kHz. This can indeed be observed in Figs. 4.6 and 4.7, where there few if any interactions between higher frequencies ( $f_1 > 30\text{kHz}$  and  $f_2 > 30\text{kHz}$ ). There are still interactions involving lower frequency modes however these too are less numerous than at  $\theta = 0^\circ$ . Crucially there is now a clear peak at  $f_1 = f_2 \approx 23\text{kHz}$  at least for Fig. 4.6 which is unfiltered, though the peak is still present in Fig. 4.7, but somewhat more localised in frequency-space. There is again a peak at  $f_1 \approx 23\text{kHz}$  and  $f_2 \approx 15\text{kHz}$  which results in  $f_3 \approx 38\text{kHz}$ . A small peak in power can be observed at this  $f_3$  in Fig. 4.5, where again it is important to emphasise that bicoherence does not recover any data concerning the direction of energy transfer.

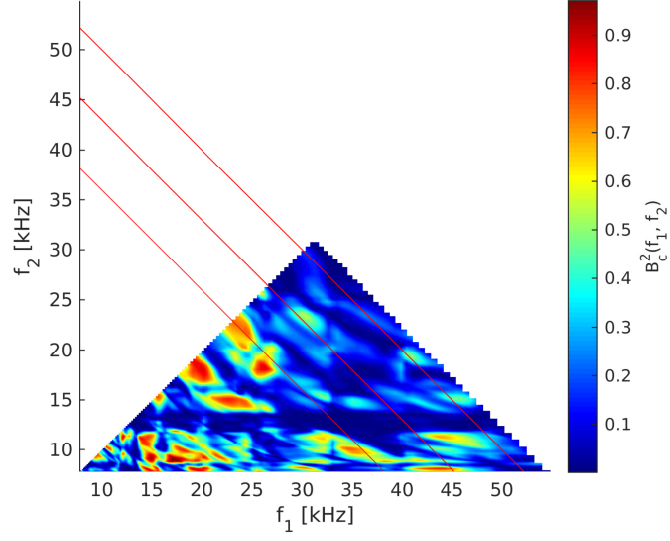


Figure 4.6: Bicoherence of the fluctuating electron density,  $n_{e1}$ , at a radial location of 0.92 and poloidal angle of  $90^\circ$ . There is a time shift of  $0.047ms \sim T_{GAM}$ , where  $T_{GAM}$  is the approximate time period of the 23kHz mode. This plot is unfiltered therefore the bicoherence values range from 0-1.

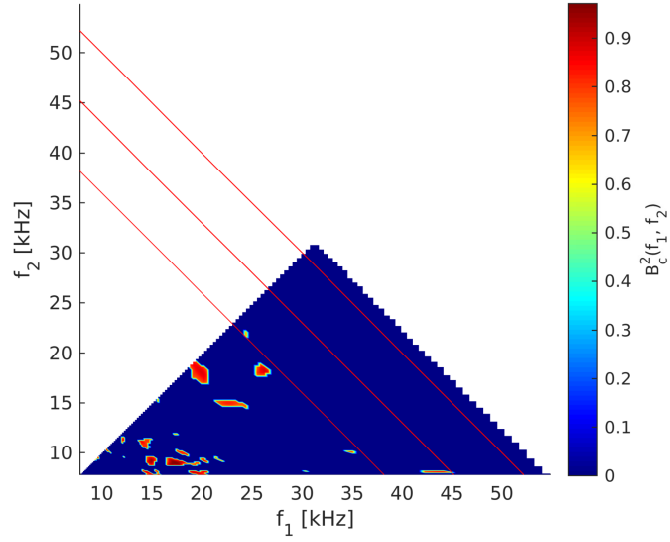


Figure 4.7: Bicoherence of the fluctuating electron density,  $n_{e1}$ , at a radial location of 0.92 and poloidal angle of  $90^\circ$ . There is a time shift of  $0.047ms \sim T_{GAM}$ , where  $T_{GAM}$  is the approximate time period of the 23kHz mode. This plot is filtered to exclude values below 0.75.

### 4.3.3 Outboard Mid-Plane Total Scalar Potential ( $\phi$ )

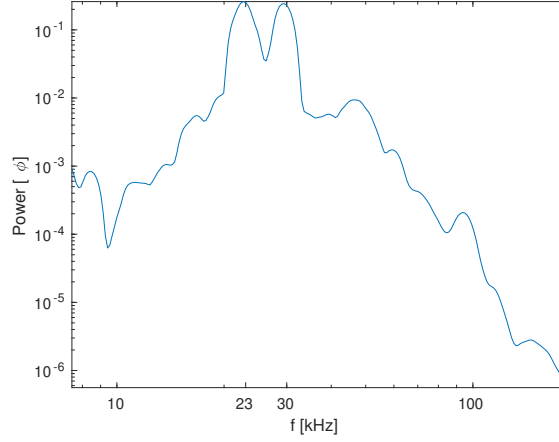


Figure 4.8: Power spectrum of the total scalar potential,  $\phi$ . The power spectrum is averaged over the time-span of 3.75-5ms at a radial location of 0.92 and poloidal angle of  $0^\circ$ .

Bicoherence analysis is also applied to data from the scalar potential. Figure 4.8 shows the power spectrum at the mid-plane and has obvious differences to the power spectra for the fluctuating electron density. Chiefly, the 23kHz and 30kHz peaks are almost identical in power and power range is  $\sim 3$  orders of magnitude larger than for the equivalent spectrum for  $n_{e1}$  (shown in Fig. 4.1). Interestingly however the bicoherence in Fig. 4.9 shows no significant self-interaction of the 30kHz mode. There is a highly localised peak near the  $f_3 = 46\text{kHz}$  guideline which matches  $f_1 \approx 30\text{kHz}$  and  $f_2 \approx 16\text{kHz}$ . The two triplets, (23, 23, 46kHz) and (30, 16, 46kHz) both contain the 46kHz mode and therefore this mode may act as an intermediary between the interaction of 23 and 30kHz but this would be via a quadruplet-like interaction which cannot be recovered from this particular bicoherence analysis. There is a peak at  $f_1 \approx 23\text{kHz}$  and  $f_2 \approx 16\text{kHz}$  but this may not couple to 30kHz as the total is  $f_1 + f_2 = 39\text{kHz}$  and this frequency only appears weakly in Fig. 4.8. Also there is no peak at  $f_1 \approx 30\text{kHz}$  and  $f_2 \approx 9\text{kHz}$ , which would then be more indicative of some coupling between 23kHz and 30kHz. There is also another highly localised peak near  $f_1 = f_2 \approx 23\text{kHz}$  which is near a similar peak in Fig. 4.7.

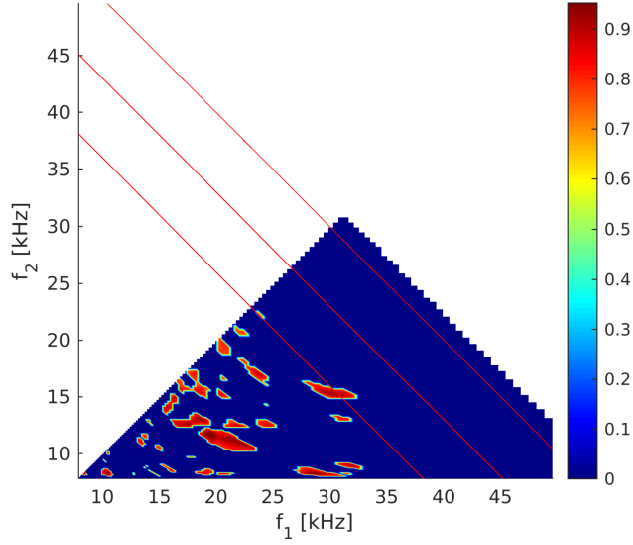


Figure 4.9: Bicoherence of the total scalar potential,  $\phi$ , at a radial location of 0.92 and poloidal angle of  $0^\circ$ . There is a time shift of  $0.047ms \sim T_{GAM}$ , where  $T_{GAM}$  is the approximate time period of the 23kHz mode. This plot is filtered to exclude values below 0.75.

#### 4.4 Summary

The results presented in this chapter showcase evidence of non-linear coupling in data from CENTORI. For the case of fluctuating electron density,  $n_{e1}$ , the analysis shows a sensitivity to poloidal location of the time series being investigated. At the mid-plane there is evidence of interaction between LFZF (Low Frequency Zonal Flows) and GAM (Geodesic Acoustic Mode). The lack of strong self-interaction at this poloidal angle is to be expected as the relative power in GAM is reduced, allowing it to couple to other frequencies. At  $\theta = 90^\circ$  there is clearer evidence of strong self-interaction of the GAM mode with a frequency of 23kHz. With regards to the total scalar potential,  $\phi$ , there are many differences compared to  $n_{e1}$ . Mainly of interest are two separate interactions of the 23kHz and 30kHz modes with a 46kHz mode which may indicate a quadruplet interaction, but this cannot be recovered through bicoherence analysis and is beyond the scope of this chapter. Nevertheless there is evidence of non-linear self-interaction of the 23kHz mode in scalar potential as well. These results show non-linear interactions involving GAMs in CENTORI and verify that the requisite background physics is present in CENTORI's physics model.

## Chapter 5

# Conclusion

The work presented in this thesis focuses on Zonal Flow-Drift Wave interaction and GAM(Geodesic Acoustic Mode) behaviour in CENTORI simulation data for a MAST plasma. These areas of interest were chosen so as to contribute to the understanding of ZF-GAM-Drift-Wave interactions which is key to understanding the L-H transition.

Firstly, the Zonal Flow-Drift-Wave interaction was investigated in the context of zonal flow modifying the growth of drift-waves in the modified Hasegawa-Wakatani (MHW) model. The standard linearization process for the MHW was changed to include a contribution from a background velocity profile. A spatial averaging technique was needed to account for the radial variability of the background velocity profile. This revealed the existence of resonances which manifested as poles in velocity space and yielded modifications to the growth rate of the drift-waves. A simulation solving MHW in a slab-model was used to investigate these modifications. Though, the data did not match the specific predictions from the modified dispersion relation well it did confirm not only a modification of the drift-wave growth due to a background velocity profile but also showed that there was energy exchange between the drift-wave and zonal flow depending on the drift-wave mode number,  $m_s$ .

Next, an introduction to GAMs is provided and a derivation closely following Winsor's treatment is presented[39]. The linear properties of GAMs are examined using data obtained from MAST simulations using CENTORI. The spatio-temporal modal structures of GAMs were recovered using CWTs (continuous wavelet transform for temporal structure) and FFTs (fast fourier transform for spatial structures). An  $m = 1$  mode in fluctuating electron density with a frequency of 23kHz was found as well as a  $m = 0$  scalar potential mode with the same frequency, indicating geometric coupling. The  $m = 1$  mode structure is validated by observing the outboard mid-plane for the fluctuating

electron density. The outboard mid-plane

Finally, the non-linear properties of GAMs are investigated using bicoherence analysis. A non-linear coupling between GAM and low-frequency zonal flows is recovered particularly at the outboard mid-plane for the fluctuating electron density  $n_{e1}$ . At  $\theta = 90^\circ$  however, there is clear evidence of non-linear self-interaction of the 23kHz GAM mode and far fewer interactions with lower frequency modes. The same analysis performed on total scalar potential  $\phi$ , data also shows evidence of non-linear self-interaction of the 23kHz mode.

## Appendix A

### GAM derivation

The derivation presented in this appendix closely follows the derivation given in Winsor et al.[39] and provides more detail than offered in Chapter 3. Starting with an electrostatic hydrodynamic model neglecting the time variation of  $\vec{B}$ :

$$\rho \frac{\partial \vec{v}_1}{\partial t} = \frac{1}{c}(\vec{J}_1 \times \vec{B}) - \vec{\nabla} \rho_1 \quad (\text{A.1})$$

$$\frac{\partial \rho_1}{\partial t} + \vec{\nabla} \cdot (\rho \vec{v}_1) = 0 \quad (\text{A.2})$$

$$\vec{\nabla} \phi_1 = \frac{1}{c}(\vec{v}_1 \times \vec{B}) \quad (\text{A.3})$$

$$\vec{\nabla} \cdot \vec{J}_1 = 0 \quad (\text{A.4})$$

$$\rho^{-\gamma} \frac{\partial \rho_1}{\partial t} - \gamma p \rho^{-\gamma-1} \frac{\partial \rho_1}{\partial t} + \vec{v}_1 \cdot \vec{\nabla} (p \rho^{-\gamma}) = 0 \quad (\text{A.5})$$

$\psi$  labels the magnetic surfaces and is defined as:  $\vec{B} \cdot \vec{\nabla} \psi = 0$ . Additionally  $p = (n_e + n_i)k_B T = 2\rho k_B T / m_i$ , ( $m_i \gg m_e$ ) and  $\rho = \rho(\psi)$  and  $p = p(\psi)$ . Starting the linearization process with a definition for the perturbation velocity:

$$\vec{v}_1 = \left( v_{1\psi} \frac{\vec{\nabla} \psi}{|\vec{\nabla} \psi|^2} + v_{1s} \frac{\vec{B} \times \vec{\nabla} \psi}{B^2} + v_{1b} \frac{\vec{B}}{B^2} \right) \exp(-i\omega t) \quad (\text{A.6})$$

Taking the component of (A.3) along  $\vec{B}$  results in 0, therefore  $\phi_1 = \phi_1(\psi)$ . Taking the component of (A.3) along  $\vec{\nabla}\psi$ :

$$\begin{aligned}\vec{\nabla}\psi.\vec{\nabla}\phi_1 &= \frac{1}{c}\vec{\nabla}\psi.(v_1 \times \vec{B}) \\ \vec{\nabla}\psi.\vec{\nabla}\psi\frac{d\phi_1}{d\psi} &= \frac{1}{c}v_1.(\vec{B} \times \vec{\nabla}\psi) \\ \frac{d\phi_1}{d\psi}|\vec{\nabla}\psi|^2 &= \frac{1}{c}v_1.(\vec{B} \times \vec{\nabla}\psi) \\ c\frac{d\phi_1}{d\psi} &= \frac{v_1.(\vec{B} \times \vec{\nabla}\psi)}{|\vec{\nabla}\psi|^2} = v_{1s}\end{aligned}$$

Taking the component of (A.3) along  $(\vec{B} \times \vec{\nabla}\psi)$  also results in 0, which means  $v_{1\psi} = 0$ . Then since  $p = p(\psi)$ ,  $\rho = \rho(\psi) \rightarrow \vec{\nabla}(p\rho^{-\gamma}) = C\vec{\nabla}\psi$ , where  $C$  is a constant, this turns the third term on the L.H.S. of (A.5) into:

$$v_1.\vec{\nabla}(p\rho^{-\gamma}) = v_{1s}\frac{(\vec{B} \times \vec{\nabla}\psi).C\vec{\nabla}\psi}{B^2} + v_{1b}\frac{\vec{B}.C\vec{\nabla}\psi}{B^2} = 0$$

This reduces (A.5) to:

$$\begin{aligned}\rho^{-\gamma}\frac{\partial p_1}{\partial t} - \gamma p\rho^{-\gamma-1}\frac{\partial \rho_1}{\partial t} &= 0 \\ \frac{\partial p_1}{\partial t} &= \frac{\gamma p}{\rho}\frac{\partial \rho_1}{\partial t} \\ p_1 &= \frac{\gamma p}{\rho}\rho_1\end{aligned}$$

Using the divergence theorem turns (A.4) into:

$$\int J_{1\psi}\mathcal{J}dS = 0.$$

Taking the component of (A.1) along  $\vec{B} \times \vec{\nabla}\psi$ :

$$\rho(\vec{B} \times \vec{\nabla}\psi).(-i\omega\vec{v}_1) = \frac{1}{c}(\vec{B} \times \vec{\nabla}\psi).(\vec{J}_1 \times \vec{B}) - (\vec{B} \times \vec{\nabla}\psi).\vec{\nabla}p_1$$

R.H.S 1st term:

$$\frac{1}{c}(\vec{B} \times \vec{\nabla}\psi).(\vec{J}_1 \times \vec{B}) = \frac{1}{c}((\vec{B}.\vec{J})(\vec{B}.\vec{\nabla}\psi) - B^2J_{1\psi}) = -\frac{1}{c}B^2J_{1\psi}$$



R.H.S 2nd term:

$$\frac{-\gamma p}{\rho}(\vec{B} \times \vec{\nabla} \psi) \cdot \vec{\nabla} \rho_1$$

L.H.S :

$$-\rho i \omega v_{1s} \frac{(\vec{B} \times \vec{\nabla} \psi) \cdot (\vec{B} \times \vec{\nabla} \psi)}{B^2} = -\rho i \omega v_{1s} \frac{B^2 |\vec{\nabla} \psi|^2 - 0}{B^2} = -\rho i \omega v_{1s} |\vec{\nabla} \psi|^2$$

Divide through by  $B^2$  then multiply by  $\mathcal{J} dS$  and integrate:

$$\begin{aligned} - \int \rho i \omega v_{1s} \frac{|\vec{\nabla} \psi|^2}{B^2} \mathcal{J} dS &= - \int J_{1\psi} \mathcal{J} dS - \frac{\gamma p}{\rho} \int \frac{(\vec{B} \times \vec{\nabla} \psi) \cdot \vec{\nabla} \rho_1}{B^2} \mathcal{J} dS \\ v_{1s} &= v_{1s}(\psi) \\ v_{1s} &= \frac{-i \gamma p}{\omega \rho^2} \int \frac{(\vec{B} \times \vec{\nabla} \psi) \cdot \vec{\nabla} \rho_1}{B^2} \mathcal{J} dS \Big/ \int \frac{|\vec{\nabla} \psi|^2}{B^2} \mathcal{J} dS \end{aligned}$$

Taking the component of (A.1) along  $\vec{B}$ :

$$\begin{aligned} \rho \vec{B} \frac{\partial \vec{v}_1}{\partial t} &= \frac{1}{c} \vec{B} \cdot (\vec{J}_1 \times \vec{B}) - \vec{B} \cdot \vec{\nabla} p_1 \\ -\rho i \omega \vec{B} \cdot \vec{v}_1 &= -\frac{\gamma p}{\rho} \vec{B} \cdot \vec{\nabla} \rho_1 \\ \vec{B} \cdot \vec{v}_1 &= v_{1b} \\ v_{1b} &= \frac{-i \gamma p}{\omega \rho^2} \vec{B} \cdot \vec{\nabla} \rho_1 \end{aligned}$$

Next observe (A.2):

$$\frac{\partial \rho_1}{\partial t} + \vec{\nabla} \cdot \rho \vec{v}_1 = 0$$

One can absorb the  $\rho$  into  $\vec{v}_1$  to eliminate the  $\psi$  dependence in the pre-factors:

$$\begin{aligned} \rho \vec{v}_1 &= \left[ \frac{-i \gamma p}{\omega \rho} \left[ \int \frac{(\vec{B} \times \vec{\nabla} \psi) \cdot \vec{\nabla} \rho_1}{B^2} \mathcal{J} dS / \int \frac{|\vec{\nabla} \psi|^2}{B^2} \mathcal{J} dS \right] \frac{(\vec{B} \times \vec{\nabla} \psi)}{B^2} \right. \\ &\quad \left. + \frac{-i \gamma p}{\omega \rho} \vec{B} \cdot \vec{\nabla} \rho_1 \frac{\vec{B}}{B^2} \right] \exp(-i \omega t) \end{aligned}$$

The term in the outer-most square-brackets is referred to as (\*), substituting it into (A.2) and rearranging  $\vec{\nabla} \cdot \rho \vec{v}_1$  to R.H.S and integrating with respect to  $t$ :

$$\begin{aligned}\rho_1 &= \int_0^\infty -\vec{\nabla} \cdot \rho \vec{v}_1 dt = -\frac{1}{i\omega} \vec{\nabla} \cdot (*) \\ &= \frac{-\gamma p}{\omega^2 \rho} \vec{\nabla} \cdot \left[ \left[ \int \frac{(\vec{B} \times \vec{\nabla} \psi) \cdot \vec{\nabla} \rho_1}{B^2} \mathcal{J} dS \right] / \int \frac{|\vec{\nabla} \psi|^2}{B^2} \mathcal{J} dS \right] \frac{(\vec{B} \times \vec{\nabla} \psi)}{B^2} + \vec{B} \cdot \vec{\nabla} \rho_1 \frac{\vec{B}}{B^2} \end{aligned}$$

Multiplying by  $\rho_1^* \mathcal{J} dS$  and integrating gives a L.H.S of:

$$\int |\rho_1|^2 \mathcal{J} dS$$

The 1st term on the R.H.S turns into:

$$\frac{-\gamma p}{\omega^2 \rho} \rho_1^* \vec{\nabla} \cdot \left( \left[ \int \frac{(\vec{B} \times \vec{\nabla} \psi) \cdot \vec{\nabla} \rho_1}{B^2} \mathcal{J} dS \right] / \int \frac{|\vec{\nabla} \psi|^2}{B^2} \mathcal{J} dS \right) \int \frac{(\vec{B} \times \vec{\nabla} \psi)}{B^2} \mathcal{J} dS$$

Using integration by parts:

$$= \frac{-\gamma p}{\omega^2 \rho} \int_0^{2\pi} \left[ \rho_1^* \left[ \dots \right] \frac{[\vec{B} \times \vec{\nabla} \psi]_\xi}{B^2} \mathcal{J} \right]_0^{2\pi} d\zeta - \frac{-\gamma p}{\omega^2 \rho} \int \left[ \dots \right] \frac{\vec{B} \times \vec{\nabla} \psi}{B^2} \cdot \vec{\nabla} \rho_1^* \mathcal{J} dS$$

The 1st term goes to zero and the 2nd term becomes:

$$\frac{\gamma p}{\omega^2 \rho} \left[ \left| \int \frac{(\vec{B} \times \vec{\nabla} \psi) \cdot \vec{\nabla} \rho_1}{B^2} \mathcal{J} dS \right|^2 / \int \frac{|\vec{\nabla} \psi|^2}{B^2} \mathcal{J} dS \right]$$

The remaining term of the modification becomes:

$$\begin{aligned} \frac{-\gamma p}{\omega^2 \rho} \int \rho_1^* \vec{\nabla} \cdot \left( \vec{B} \cdot \vec{\nabla} \rho_1 \frac{\vec{B}}{B^2} \right) \mathcal{J} dS &= \frac{-\gamma p}{\omega^2 \rho} \int_0^{2\pi} \left[ \rho_1^* (\vec{B} \cdot \vec{\nabla} \rho_1) \frac{[\vec{B}]_\xi}{B^2} \mathcal{J} \right]_0^{2\pi} d\zeta \\ &\quad - \frac{-\gamma p}{\omega^2 \rho} \int \vec{B} \cdot \vec{\nabla} \rho_1 \frac{\vec{B}}{B^2} \cdot \vec{\nabla} \rho_1^* \mathcal{J} dS \\ &= \frac{\gamma p}{\omega^2 \rho} \int \frac{|\vec{B} \cdot \vec{\nabla} \rho_1|^2}{B^2} \mathcal{J} dS \end{aligned}$$

Putting it all together and multiplying by  $\omega^2$ :

$$\omega^2 \int |\rho_1|^2 \mathcal{J} dS = \frac{\gamma p}{\rho} \left[ \left| \int \frac{B^2 (\vec{B} \times \vec{\nabla} \psi) \cdot \vec{\nabla} \rho_1}{B^4} \mathcal{J} dS \right|^2 / \int \frac{|\vec{\nabla} \psi|^2}{B^2} \mathcal{J} dS + \int \frac{|\vec{B} \cdot \vec{\nabla} \rho_1|^2}{B^2} \mathcal{J} dS \right] \quad (\text{A.7})$$

Looking at the numerator of the first term in the square brackets:

$$\begin{aligned}
& \int \frac{B^2(\vec{B} \times \vec{\nabla}\psi) \cdot \vec{\nabla}\rho_1}{B^4} \mathcal{J} dS \\
&= \int \rho_1 \vec{\nabla} \cdot \left( \frac{B^2(\vec{B} \times \vec{\nabla}\psi)}{B^4} \right) \mathcal{J} dS \\
&= \int \rho_1 \left[ B^2 \vec{\nabla} \cdot \left( \frac{\vec{B} \times \vec{\nabla}\psi}{B^4} \right) + \frac{\vec{B} \times \vec{\nabla}\psi}{B^4} \cdot \vec{\nabla}(B^2) \right] \mathcal{J} dS \\
&= \int \rho_1 \left[ \frac{(\vec{B} \times \vec{\nabla}\psi) \cdot \vec{\nabla}(B^2)}{B^4} \right] \mathcal{J} dS
\end{aligned}$$

(The last step is because the first term in the square brackets in the penultimate equation can be rearranged via a vector calculus identity  $(\vec{\nabla} \cdot (\vec{A} \times \vec{B})) = \vec{A} \cdot (\vec{\nabla} \times \vec{B}) + \vec{B} \cdot (\vec{\nabla} \times \vec{A})$  to have  $\vec{\nabla}\psi \cdot (\vec{\nabla} \times \vec{B}) = \frac{4\pi}{c} \vec{J}_{1\psi}$  which when integrated goes to 0). This turns (A.7) into:

$$\omega^2 \int |\rho_1|^2 \mathcal{J} dS = \frac{\gamma p}{\rho} \left[ \left| \int \rho_1 \frac{(\vec{B} \times \vec{\nabla}\psi) \cdot \vec{\nabla} B^2}{B^4} \mathcal{J} dS \right|^2 / \int \frac{|\vec{\nabla}\psi|^2}{B^2} \mathcal{J} dS + \int \frac{|\vec{B} \cdot \vec{\nabla}\rho_1|^2}{B^2} \mathcal{J} dS \right] \quad (\text{A.8})$$

This matches the result in the paper. This is a general result that is agnostic when it comes to coordinate systems. The main elements to address when defining a specific coordinate system are the definition of  $\vec{\nabla}$  and the  $\mathcal{J}$ , which is the Jacobian. An example of extracting a result for a given coordinate system is to start with (A.8) and change to a coordinate system with metric:

$$\begin{aligned}
dl^2 &= dr^2 + r^2 d\theta^2 + \left[ 1 + \frac{r}{R} \cos \theta \right]^2 dz^2 \\
g &= \begin{bmatrix} 1 & 0 & 0 \\ 0 & r^2 & 0 \\ 0 & 0 & \left( 1 + \frac{r}{R} \cos \theta \right)^2 \end{bmatrix} \\
\det(g) &= r^2 \left( 1 + \frac{r}{R} \cos \theta \right)^2 \\
\mathcal{J} &= \sqrt{\det(g)} = r \left( 1 + \frac{r}{R} \cos \theta \right) \\
\mathcal{J} dS &= r \left( 1 + \frac{r}{R} \cos \theta \right) d\theta dz
\end{aligned}$$

This is Knorr's model(cite Knorr), where  $r$  is the radial direction along the minor radius,  $\theta$  is the poloidal angle and  $z$  is in the toroidal direction. This is demonstrated in Fig.

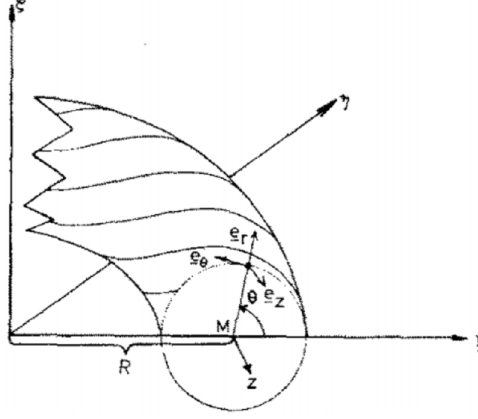


Figure A.1: Knorr's model[6]

A.1. For modes independent of  $z$  then L.H.S becomes:

$$\omega^2 \int_0^{2\pi} |\rho_1|^2 r \left(1 + \frac{r}{R} \cos \theta\right) d\theta \quad \rho_1 = \rho_1(r, \theta), \psi = r$$

The numerator of the first term on the R.H.S of (A.8) becomes:

$$\vec{B} \times \vec{\nabla} \psi = \vec{B} \times \vec{\nabla} r \quad \vec{B} = \frac{B_0}{1 + \frac{r}{R} \cos \theta} [\vec{e}_z + f(r) \vec{e}_\theta]$$

$$\vec{B} \times \vec{\nabla} r = \det \begin{bmatrix} \vec{e}_r & \vec{e}_\theta & \vec{e}_z \\ 0 & \frac{B_0 f}{1 + \frac{r}{R} \cos \theta} & \frac{B_0}{1 + \frac{r}{R} \cos \theta} \\ 1 & 0 & 0 \end{bmatrix} = \frac{B_0}{1 + \frac{r}{R} \cos \theta} \begin{bmatrix} 0 \\ 1 \\ -f \end{bmatrix}$$

$$\text{where } f = \frac{ri(r)}{2\pi(R^2 - r^2)^{\frac{1}{2}}} \quad \text{where } \frac{i(r)}{2\pi} = \text{rotational transform}$$

$$\begin{aligned} (\vec{B} \times \vec{\nabla} r) \cdot \vec{\nabla} B^2 &= (\vec{B} \times \vec{\nabla} r) \cdot \begin{bmatrix} \frac{\partial B^2}{\partial r} \\ \frac{\partial B^2}{\partial \theta} \\ 0 \end{bmatrix} \quad \text{note that: } B^2 = \frac{B_0^2}{(1 + \frac{r}{R} \cos \theta)^2} (1 + f^2) \\ &= \frac{B_0}{1 + \frac{r}{R} \cos \theta} \frac{\partial B^2}{\partial \theta} = \frac{B_0}{1 + \frac{r}{R} \cos \theta} B_0^2 (1 + f^2) \left( \frac{2r}{R} \sin \theta \right) \left( 1 + \frac{r}{R} \cos \theta \right)^{-3} \end{aligned}$$

$$\rightarrow \left| \int_0^{2\pi} \frac{\rho_1}{B^4} (\vec{B} \times \vec{\nabla} r) \cdot \vec{\nabla} B^2 \mathcal{J} dS \right|^2 = \frac{4r^4}{B_0^2 R^2 (1 + f^2)^2} \left| \int_0^{2\pi} \rho_1 \left( \sin(\theta) + \frac{r}{2R} \sin(2\theta) \right) d\theta \right|^2$$

The denominator if the 1st term on R.H.S of (A.8) becomes:

$$\begin{aligned} \int_0^{2\pi} \frac{1}{B^2} r \left[ 1 + \frac{r}{R} \cos \theta \right] d\theta &= r \int_0^{2\pi} \frac{\left( 1 + \frac{r}{R} \cos(\theta) \right)^2}{B_0^2(1+f^2)} \left( 1 + \frac{r}{R} \cos(\theta) \right) d\theta \\ &= \frac{r}{B_0^2(1+f^2)} \int_0^{2\pi} \left( 1 + \frac{r}{R} \cos(\theta) \right)^3 d\theta = \frac{1}{B_0^2(1+f^2)} \left( 2\pi r \left( 1 + \frac{3}{2} \frac{r^2}{R^2} \right) \right) \end{aligned}$$

The second term on the R.H.S of (A.8) becomes:

$$\begin{aligned} \int_0^{2\pi} \frac{|\vec{B} \cdot \vec{\nabla} \rho_1|^2}{B^2} r \left( 1 + \frac{r}{R} \cos \theta \right) d\theta &= \int_0^{2\pi} \frac{1}{B^2} \left| \frac{B_0}{1 + \frac{r}{R} \cos \theta} f \frac{\partial \rho_1}{\partial \theta} \right|^2 r \left( 1 + \frac{r}{R} \cos \theta \right) d\theta \\ &= \frac{f^2}{1+f^2} \int_0^{2\pi} \left| \frac{\partial \rho_1}{\partial \theta} \right|^2 r \left( 1 + \frac{r}{R} \cos \theta \right) d\theta \end{aligned}$$

Combining it all to complete the transform(without full simplification):

$$\begin{aligned} &\omega^2 \int_0^{2\pi} |\rho_1|^2 r \left( 1 + \frac{r}{R} \cos(\theta) \right) d\theta \\ &= \frac{\gamma p}{\rho} \left[ \frac{2r^3}{R^2(1+f^2)} \left| \int_0^{2\pi} \rho_1 \left( \sin(\theta) + \frac{r}{2R} \sin(2\theta) \right) d\theta \right|^2 / \pi \left( 1 + \frac{3r^2}{2R^2} \right) \right. \\ &\quad \left. + \frac{f^2}{1+f^2} \int_0^{2\pi} \left| \frac{\partial \rho_1}{\partial \theta} \right|^2 r \left( 1 + \frac{r}{R} \cos(\theta) \right) d\theta \right] \end{aligned} \quad (\text{A.9})$$

Now there is a slight complication in the derivation as presented in Winsor's original paper. At some point Winsor takes the of  $r \ll R$  and assumes  $\rho_1 = \sin(\theta)$ . It is unclear however when this limit and assumption are applied. If the  $r \ll R$  limit is applied after Eq. A.9, then the following result is obtained:

$$\begin{aligned} &\omega^2 \int_0^{2\pi} |\rho_1|^2 d\theta \\ &= \frac{\gamma p}{\rho r^2(1+f^2)} \left[ 2r^2 \left| \int_0^{2\pi} \rho_1 \left( \sin(\theta) + \frac{r}{2R} \sin(2\theta) \right) d\theta \right|^2 / \pi R^2 \left( 1 + \frac{3r^2}{2R^2} \right) \right. \\ &\quad \left. + f^2 \int_0^{2\pi} \left| \frac{\partial \rho_1}{\partial \theta} \right|^2 d\theta \right] \end{aligned} \quad (\text{A.10})$$

and if  $\rho_1 = \sin(\theta)$  then:

$$\begin{aligned}
\omega^2 \pi &= \frac{\gamma p}{\rho r^2 (1 + f^2)} \left[ 2r^2 \pi^2 / \pi R^2 + f^2 \pi \right] \\
\rightarrow \quad \omega^2 &= \frac{2\gamma p}{\rho R^2} \left[ 1 + \frac{R^2 f^2}{2r^2 (1 + f^2)} \right] \\
f^2 &= \frac{r^2 i^2}{4\pi^2 (R^2 - r^2)} \approx \frac{r^2 i^2}{4\pi^2 R^2} \quad \text{then } (1 + f^2) \approx 1 \\
\frac{R^2 f^2}{2r^2} &= \frac{i^2}{8\pi^2} \\
\omega^2 &= \frac{2\gamma p}{\rho R^2} \left( 1 + \frac{i^2}{8\pi^2} \right) = \omega_s^2 \left( 2 + \frac{1}{q^2} \right)
\end{aligned}$$

# Bibliography

- [1] P.H. Rebut, R.J. Bickerton, and B.E. Keen. The joint european torus: installation, first results and prospects. *Nuclear Fusion*, 25(9):1011–1022, 1985. doi: 10.1088/0029-5515/25/9/003.
- [2] R J Akers, J W Ahn, G Y Antar, L C Appel, D Applegate, C Brickley, C Bunting, P G Carolan, C D Challis, and N J et al. Conway. Transport and confinement in the mega ampère spherical tokamak (mast) plasma. *Plasma Physics and Controlled Fusion*, 45(12A):A175–A204, 2003. doi: 10.1088/0741-3335/45/12a/013.
- [3] G.H. Miley, H. Towner, and N. Ivich. Fusion cross sections and reactivities. 1974. doi: 10.2172/4014032.
- [4] 2011. URL <https://www.euro-fusion.org/news/detail/tokamak-principle>.
- [5] A. Cardinali, C. Castaldo, R. Cesario, L. Amicucci, A. Galli, F. Napoli, L. Panaccione, C. Riccardi, F. Santini, and G. et al. Schettini. Radio-frequency current drive for thermonuclear fusion reactors. *Scientific Reports*, 8(1), 2018. doi: 10.1038/s41598-018-27996-9.
- [6] Georg Knorr. Equilibrium of a toroidal plasma with finite resistivity and inertia. *Physics of Fluids*, 8(7):1334, 1965. doi: 10.1063/1.1761404.
- [7] P.J. Knight, A. Thyagaraja, T.D. Edwards, J. Hein, M. Romanelli, and K.G. McClements. Centori: A global toroidal electromagnetic two-fluid plasma turbulence code. *Computer Physics Communications*, 183(11):2346–2363, 2012. doi: 10.1016/j.cpc.2012.06.002.
- [8] 2020. URL <https://uk.mathworks.com/help/wavelet/ref/cwtft.html#buu64ch>.

- [9] S. Gadgil, B. Hnat, and G. Rowlands. Investigation of drift-wave instability in the presence of zonal flows using spatial averaging. *Physics of Plasmas*, 26(1):012105, 2019. doi: 10.1063/1.5049087.
- [10] B Hnat, S Gadgil, A Kirk, F Militello, and N Walkden. Experimental constraint on the radial mode number of the geodesic acoustic mode from multi-point langmuir probe measurements in mast ohmic plasma. *Plasma Physics and Controlled Fusion*, 60(8):085016, 2018. doi: 10.1088/1361-6587/aacd58.
- [11] Energy & Industrial Strategy Department for Business. *Industrial Strategy Offshore Wind Sector Deal*. 2019.
- [12] Hyun-Gil Kim, Jae-Ho Yang, Weon-Ju Kim, and Yang-Hyun Koo. Development status of accident-tolerant fuel for light water reactors in korea. *Nuclear Engineering and Technology*, 48(1):1–15, 2016. doi: 10.1016/j.net.2015.11.011.
- [13] Michael F. L’Annunziata. Neutron radiation. *Radioactivity*, pages 253–288, 2007. doi: 10.1016/b978-044452715-8.50007-4.
- [14] Yoshio Horibe and Mituko Kobayakawa. Deuterium abundance of natural waters. *Geochimica et Cosmochimica Acta*, 20(3-4):273–283, 1960. doi: 10.1016/0016-7037(60)90078-8.
- [15] Keii Gi, Fuminori Sano, Keigo Akimoto, Ryoji Hiwatari, and Kenji Tobita. Potential contribution of fusion power generation to low-carbon development under the paris agreement and associated uncertainties. *Energy Strategy Reviews*, 27:100432, 2020. doi: 10.1016/j.esr.2019.100432.
- [16] Keywan Riahi, Detlef P. van Vuuren, Elmar Kriegler, Jae Edmonds, Brian C. O’Neill, Shinichiro Fujimori, Nico Bauer, Katherine Calvin, Rob Dellink, and Oliver et al. Fricko. The shared socioeconomic pathways and their energy, land use, and greenhouse gas emissions implications: An overview. *Global Environmental Change*, 42:153–168, 2017. doi: 10.1016/j.gloenvcha.2016.05.009.
- [17] S. I. Braginskii. *Transport Processes in a plasma, Reviews of plasma physics, Vol. 1*. Consultants Bureau, 1965.
- [18] John A Wesson. *Tokamaks*. Clarendon Press, 2004.
- [19] C.S. Chang, S. Ku, A. Loarte, V. Parail, F. Köchl, M. Romanelli, R. Maingi, J.-W. Ahn, T. Gray, and J. et al. Hughes. Gyrokinetic projection of the divertor heat-flux



- width from present tokamaks to iter. *Nuclear Fusion*, 57(11):116023, 2017. doi: 10.1088/1741-4326/aa7efb.
- [20] Martin Greenwald. Density limits in toroidal plasmas. *Plasma Physics and Controlled Fusion*, 44(8):R27–R53, 2002. doi: 10.1088/0741-3335/44/8/201.
- [21] A.E. Costley. On the fusion triple product and fusion power gain of tokamak pilot plants and reactors. *Nuclear Fusion*, 56(6):066003, 2016. doi: 10.1088/0029-5515/56/6/066003.
- [22] M. Valovic, R. Akers, G. Cunningham, L. Garzotti, B. Lloyd, D. Muir, A. Patel, D. Taylor, M. Turnyanskiy, and M. Walsh. Scaling of h-mode energy confinement withipandbtin the mast spherical tokamak. *Nuclear Fusion*, 49(7):075016, 2009. doi: 10.1088/0029-5515/49/7/075016.
- [23] Elizabeth Gibney. Uk hatches plan to build world’s first fusion power plant. *Nature*, 2019. doi: 10.1038/d41586-019-03039-9.
- [24] Masahiro Wakatani and Akira Hasegawa. A collisional drift wave description of plasma edge turbulence. *Physics of Fluids*, 27(3):611, 1984. doi: 10.1063/1.864660.
- [25] Akira Hasegawa and Yuji Kodama. Spectrum cascade by mode coupling in drift-wave turbulence. *Phys. Rev. Lett.*, 41:1470–1473, Nov 1978. doi: 10.1103/PhysRevLett.41.1470.
- [26] Alexander V. Melnikov. Applied and fundamental aspects of fusion science. *Nature Physics*, 12(5):386–390, 2016. doi: 10.1038/nphys3759.
- [27] P H Diamond, S-I Itoh, K Itoh, and T S Hahm. Zonal flows in plasma—a review. *Plasma Physics and Controlled Fusion*, 47(5):R35–R161, 2005. doi: 10.1088/0741-3335/47/5/r01.
- [28] Ryusuke. Numata, Rowena. Ball, and Robert. L. Dewar. Bifurcation in electrostatic resistive drift wave turbulence. *Physics of Plasmas*, 14(10):102312, 2007. doi: 10.1063/1.2796106.
- [29] A. M. Dimits, G. Bateman, M. A. Beer, B. I. Cohen, W. Dorland, G. W. Hammett, C. Kim, J. E. Kinsey, M. Kotschenreuther, and A. H. et al. Kritz. Comparisons and physics basis of tokamak transport models and turbulence simulations. *Physics of Plasmas*, 7(3):969–983, 2000. doi: 10.1063/1.873896.

- [30] P. W. Terry. Suppression of turbulence and transport by sheared flow. *Rev. Mod. Phys.*, 72:109–165, Jan 2000. doi: 10.1103/RevModPhys.72.109.
- [31] F. Wagner, G. Fussmann, T. Grave, M. Keilhacker, M. Kornherr, K. Lackner, K. McCormick, E. R. Müller, A. Stäbler, G. Becker, K. Bernhardt, U. Ditte, A. Eberhagen, O. Gehre, J. Gernhardt, G. v. Gierke, E. Glock, O. Gruber, G. Haas, M. Hesse, G. Janeschitz, F. Karger, S. Kissel, O. Klüber, G. Lisitano, H. M. Mayer, D. Meisel, V. Mertens, H. Murmann, W. Poschenrieder, H. Rapp, H. Röhr, F. Ryter, F. Schneider, G. Siller, P. Smeulders, F. Söldner, E. Speth, K. H. Steuer, Z. Szymanski, and O. Vollmer. Development of an edge transport barrier at the h-mode transition of asdex. *Phys. Rev. Lett.*, 53:1453–1456, Oct 1984. doi: 10.1103/PhysRevLett.53.1453.
- [32] R. Dewar and R. Abdullatif. Zonal flow generation by modulational instability. *Frontiers in turbulence and coherent structures*, pages 415–430, 2007. doi: 10.1142/9789812771025\_0017.
- [33] S. Gallagher, B. Hnat, C. Connaughton, S. Nazarenko, and G. Rowlands. The modulational instability in the extended hasegawa-mima equation with a finite larmor radius. *Physics of Plasmas*, 19(12):122115, 2012. doi: 10.1063/1.4773050.
- [34] G. Manfredi, C. M. Roach, and R. O. Dendy. Zonal flow and streamer generation in drift turbulence. *Plasma Physics and Controlled Fusion*, 43(6):825–837, 2001. doi: 10.1088/0741-3335/43/6/307.
- [35] B. N. Rogers, W. Dorland, and M. Kotschenreuther. Generation and stability of zonal flows in ion-temperature-gradient mode turbulence. *Physical Review Letters*, 85(25):5336–5339, 2000. doi: 10.1103/physrevlett.85.5336.
- [36] Yu. I. Troitskaya and L. A. Ostrovskiy. Influence of velocity fine structure in the ocean on internal wave generation. *Izvestiya, Atmospheric and Oceanic Physics*, 24(7), 1988.
- [37] Akio Arakawa. Computational design for long-term numerical integration of the equations of fluid motion: Two-dimensional incompressible flow. part i. *Journal of Computational Physics*, 1(1):119–143, 1966. doi: 10.1016/0021-9991(66)90015-5.
- [38] George Em. Karniadakis, Moshe. Israeli, and Steven. A. Orszag. High-order splitting methods for the incompressible navier-stokes equations. *Journal of Computational Physics*, 97(2):414–443, 1991. doi: 10.1016/0021-9991(91)90007-8.

- [39] Niels Winsor. Geodesic acoustic waves in hydromagnetic systems. *Physics of Fluids*, 11(11):2448, 1968. doi: 10.1063/1.1691835.
- [40] L.Th.M. Ornstein and K.M. Young. *Bulletin of the American Physical Society*, 13 (286), 1968.
- [41] V D Shafranov. On magnetohydrodynamical equilibrium configurations. *Soviet Phys. JETP*, Vol: 6, 3 1958.
- [42] H Grad and H Rubin. Hydromagnetic equilibria and force-free fields. 10 1958.
- [43] A. B. Rechester and M. N. Rosenbluth. Electron heat transport in a tokamak with destroyed magnetic surfaces. *Phys. Rev. Lett.*, 40:38–41, Jan 1978. doi: 10.1103/PhysRevLett.40.38. URL <https://link.aps.org/doi/10.1103/PhysRevLett.40.38>.
- [44] A. A. Ware. Pinch effect for trapped particles in a tokamak. *Physical Review Letters*, 25(1):15–17, 1970. doi: 10.1103/physrevlett.25.15.
- [45] J. R. Robinson, B. Hnat, A. Thyagaraja, K. G. McClements, P. J. Knight, and A. Kirk. Global two-fluid simulations of geodesic acoustic modes in strongly shaped tight aspect ratio tokamak plasmas. *Physics of Plasmas*, 20(5):052302, 2013. doi: 10.1063/1.4804271.
- [46] Paul S Addison. *The illustrated wavelet transform handbook*. Institute of Physics Pub., 2002.
- [47] Signal Analyzer and Wavelet Denoiser. Choose a wavelet- matlab & simulink- mathworks united kingdom, 2020. URL <https://uk.mathworks.com/help/wavelet/gs/choose-a-wavelet.html>.
- [48] E. A. Sorokina, V. P. Lakhin, L. V. Konovaltseva, and V. I. Ilgisonis. Geodesic acoustic modes in noncircular cross section tokamaks. *Plasma Physics Reports*, 43 (3):271–279, 2017. doi: 10.1134/s1063780x17030126.
- [49] V.P. Lakhin, V.I. Ilgisonis, and A.I. Smolyakov. Geodesic acoustic modes and zonal flows in toroidally rotating tokamak plasmas. *Physics Letters A*, 374(48):4872–4875, 2010. doi: 10.1016/j.physleta.2010.10.012.
- [50] 2020. URL <https://uk.mathworks.com/help/matlab/ref/fft2.html>.

- [51] Y Nagashima, K Itoh, S-I Itoh, A Fujisawa, M Yagi, K Hoshino, K Shinohara, A Ejiri, Y Takase, and T et al. Ido. In search of zonal flows by using direct density fluctuation measurements. *Plasma Physics and Controlled Fusion*, 49(10):1611–1625, 2007. doi: 10.1088/0741-3335/49/10/002.
- [52] M. Sasaki, K. Itoh, Y. Nagashima, A. Ejiri, and Y. Takase. Nonlinear self-interaction of geodesic acoustic modes in toroidal plasmas. *Physics of Plasmas*, 16(2):022306, 2009. doi: 10.1063/1.3076933.
- [53] B Scott. The geodesic transfer effect on zonal flows in tokamak edge turbulence. *Physics Letters A*, 320(1):53–62, 2003. doi: 10.1016/j.physleta.2003.10.080.
- [54] Young C. Kim and Edward J. Powers. Digital bispectral analysis and its applications to nonlinear wave interactions. *IEEE Transactions on Plasma Science*, 7(2):120–131, 1979. doi: 10.1109/tps.1979.4317207.
- [55] Joërg Büchner, Manfred Scholer, and Christian T Dum. *Space Plasma Simulation*. 2003.
- [56] Ch. P. Ritz, E. J. Powers, and R. D. Bengtson. Experimental measurement of three-wave coupling and energy cascading. *Physics of Fluids B: Plasma Physics*, 1(1):153–163, 1989. doi: 10.1063/1.859082.
- [57] Ch.P. Ritz and E.J. Powers. Estimation of nonlinear transfer functions for fully developed turbulence. *Physica D: Nonlinear Phenomena*, 20(2-3):320–334, 1986. doi: 10.1016/0167-2789(86)90036-9.
- [58] Ch. P. Ritz, E. J. Powers, R. W. Micksad, and R. S. Solis. Nonlinear spectral dynamics of a transitioning flow. *Physics of Fluids*, 31(12):3577, 1988. doi: 10.1063/1.866875.
- [59] M. A. Balikhin, H. St.-C. K. Alleyne, R. A. Treumann, M. N. Nozdrachev, S. N. Walker, and W. Baumjohann. The role of nonlinear interaction in the formation of lf whistler turbulence upstream of a quasi-perpendicular shock. *Journal of Geophysical Research: Space Physics*, 104(A6):12525–12535, 1999. doi: 10.1029/1998ja900102.
- [60] T. Dudok de Wit, V. V. Krasnosel’skikh, M. Dunlop, and H. Lüher. Identifying nonlinear wave interactions in plasmas using two-point measurements: A case study of short large amplitude magnetic structures (slams). *Journal of Geophysical Research: Space Physics*, 104(A8):17079–17090, 1999. doi: 10.1029/1999ja900134.

- [61] G. Z. dos Santos Lima, Z. O. Guimarães-Filho, A. M. Batista, I. L. Caldas, S. R. Lopes, R. L. Viana, I. C. Nascimento, and Yu. K. Kuznetsov. Bicoherence in electrostatic turbulence driven by high magnetohydrodynamic activity in tokamak chauffage alfvén brésilien. *Physics of Plasmas*, 16(4):042508, 2009. doi: 10.1063/1.3099701.
- [62] M. R. Hajj, J. B. Davila, R. W. Miksad, and E. J. Powers. A technique to measure wavenumber mismatch between quadratically interacting modes. *Experiments in Fluids*, 18(4):217–224, 1995. doi: 10.1007/bf00195090.